Title
Be Our Guest: 129Xe Detection in Macrocycles and Oriented Environments

Author
Slack, Clancy

Publication Date
2016

Peer reviewed|Thesis/dissertation

Be Our Guest:
^{129}Xe Detection in Macrocycles and Oriented Environments

by

Clancy Carlton Slack

A dissertation submitted in partial satisfaction of the
requirements for the degree of
Doctor of Philosophy

in

Chemistry

in the

GRADUATE DIVISION
of the
UNIVERSITY OF CALIFORNIA, BERKELEY

Committee in charge:
Professor Alexander Pines, Chair
Professor David Wemmer
Professor Jeffery Reimer

Summer 2016

Be Our Guest:
^{129}Xe Detection in Macrocycles and Oriented Environments

Abstract

Be Our Guest:
^{129}Xe Detection in Macrocycles and Oriented Environments

by

Clancy Carlton Slack

Doctor of Philosophy in Chemistry

University of California, Berkeley

Professor Alexander Pines, Chair

Nuclear Magnetic Resonance (NMR) is an extrememly powerful technique for determining chemical structure, which can look in opaque samples. Using ^{129}Xe as our detected nucleus we can synthesize molecualar cages that interact with their chemical environment or molecular target, which is observed through the chemical shift of the xenon in the molecular cage. The use of spin exchange optical pumping (SEOP) the pool of xenon can be hyperpolarized to give signal enhancement that makes it on par with proton NMR techniques. Further using chemical exchnge saturation transfer (CEST) we can use the exchange of xenon in and out of the molecualr cage to detect concentrations in the nanomolar range. In chapter 3 we will look at a cryptophane-A based sensor and how the chemical shift changes when the cage is chelated to different metal ions. In chapter 4 we looked at using a relaxation based detection method for cryptophane sensors showing a decrease in relaxation time when bound to the protein Avidin. In chapter 5 we look at cucurbituril based xenon detection with a base activated sensor using a rotaxane backbone. In chapter 6 we further develop the rotaxane to include a peptide sequence recognizable by the enzyme MMP2. In chapter 7 we explore a new device that allows for xenon to dissolve directly into ordered media without disturbing the local structure, and in chapter 8 we show preliminary results and discuss the future of xenon based sensors.

To my teachers

Contents

List of Figures

List of Tables

Acknowledgments

I'd like to start my thanking my friends, family, and collegues for their support during my time in gradaute school. I certainly couldn't have accomplished as much as I have without all of you.

Of course I need to start by acknowledging and thanking my advisor Alex Pines, who has consistently believed in me far more then I have believed in myself. Thank you for embracing my interestes outside of the research lab and working equally hard to help me become an excellent educator as well a researcher. I appreciate that you always encouraged me to chase down and test my ideas no matter how crazy they sounded and you never missed an oppertunity to celebrate my successes. David Wemmer for your avidce and constructive criticisms over the years. You've helped me be a better scientific writer and develop more thoughtful experiments. Matt Francis, whose collaboration has helped me have a more complete understanding of the systems I've been studying. Your support in working through some difficult challeneges in understanding our findings has been invaluable.

I would also like to thank Monica Smith, Matt Ramirez, Lindsay Sperling, Hattie Ring and Dan Kennedy who first welcomed me onto the xenon team and showed me how to run experiments and helped me prepare for my qualifying exam. You were excllent mentors and I really sppreciate all the help you gave me. Also Phuong Dao and Anna Parker the members of my cohort year, it was certainly an interesting journey from start to finish and I'm glad I had both of you to share it with. Also Paul Gannsel, Claudia Avalos, Pete Mustonen, Haijing Wang, and Scott Seltzer who were here when I joined and not on the xenon projects. You were all very welcoming and I always enjoyed spending time with you.

Of course I need to thank the current xenon subgroup, Ashley Truxal, Muller Gomes, Chris Vassiliou, Keunhong Jeong, and Joel Finbloom. It is always a pleasure working with you guys, you're great ideas keep work exciting and interesting and I'm lucky to have learned from each of you. I look forward to seeing all the great things you will produce moving forward.

Outside of the lab I need to thank my west coast family. I've made some amazing friends who have kept me sane throughout the years especially Kanwal Palla, Steve Cardinali, Amber Ritchardson, Tobias Harrison-Noonan, Justine Savor, and Gordon Hoople. Also Danny Alvarez for putting up with my craziness, especially while I've been working on this thesis.

Finally I would like to acknowledge my brother Zach Slack, and my parents Robert Slack, Donna Slack and Kelley Carlton for their constant encouragement.

Thank you to everyone.

Symbols

$\mathbf{B}$	Magnetic field vector
B_0	Amplitude of static magnetic field
$\mathbf{I}$	Nuclear spin operators
$\mathbf{S}$	Electron spin operators
γ	Gyromagnetic ratio of spin
B_1	Microwave or radio frequency field
T_1^*	effective spin-lattice relaxation time
T_2^*	effective spin-spin relaxation time
T_1	spin-lattice relaxation time
T_2	spin-spin relaxation time
$\mathbf{M}$	Spin magnetization
$\mathbf{B_0}$	Magnetic field vector
B_0	Amplitude of the static magnetic field
ω_0	Larmor Resonance frequency

Acronyms

NMR	Nuclear magnetic resonance
hyperCEST	Hyperpolarized Xenon Chemical Exchange Saturation Transfer
SEOP	Spin-Exchange Optical-Pumping
RF	Radiofrequency
CPMG	Carr Purcell Meiboom Gill
OD	Outer diameter
ID	Inner diameter
Cry-A	Cryptophane-A
CB6	Cucurbit-6-uril
MBBA	N-(4-Methoxybenzylidene)-4-butylaniline
pf1	Bacteriophage (aqueous liquid crystal)

Physical Constants

h	Planck constant, 6.626176×10^{-34} J· s
$\hbar$	Reduced Planck constant, h/2π
k_B	Boltzmann constant, 1.380662 times 10^{-23} J/K
e	Electron charge, 1.602177×10^{-19} C
m_e	Electron rest mass, 9.109383×10^{-31} kg
m_p	Proton rest mass, 1.672622×10^{-27} kg

μ_0	Vacuum permeability, $4\pi \times 10^{-7}$ V $\cdot$ s/(A$\cdot$ m)
g_s	Electron g-factor, -2.00231930436153 $\pm$ 2.6 $\times 10^{-13}$
μ_B	Bohr magneton, e$\hbar/(2\mathrm{m}_e) = 9.274\times 10^{-24}$ J/T
μ_N	Nuclear magneton, e$\hbar/(2\mathrm{m}_p) = 5.051 \times 10^{-27}$ J/T

Chapter 1

Introduction

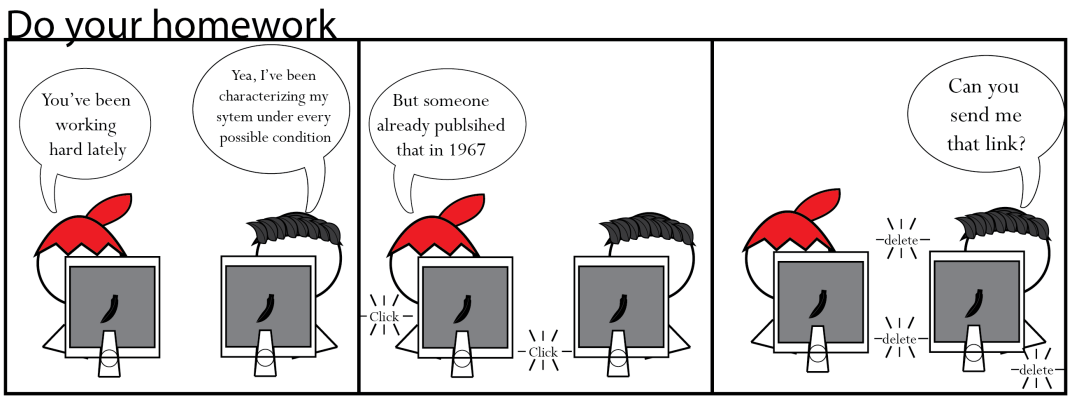

1.1 An Introduction

The need for sensitive molecular detection is inherent across many fields including medicine and pharmaceuticals, molecular biology, environmental toxicology and materials science. Obtaining spatial distribution information about a molecule as well as information about its local chemical environment can be extremely powerful. Current techniques used for molecular detection include fluorescence [4], ^{1}H MRI [5], electrochemical techniques [6], and imaging mass spectrometry [7]. None of these techniques can be used with opaque samples while being flexible enough to look at many kinds of systems. Using ^{129}Xe NMR we can circumvent many of the challenges associated with these techniques, while also introducing some unique advantages.

The goal of this dissertation is to take a critical look at currently existing techniques in Nuclear Magnetic Resonance (NMR) and discuss alternatives using ^{129}Xe. These techniques try to take advantage of signal enhancement by hyperpolarization, sensitivity from chemical exchange and simplified spectra, and the intrinsic benefits of xenon as an environmental probe. Before an argument for xenon based detection by NMR can be made an understanding

of the underlying physics is necessary. This section will focus on the basic principals of magnetic resonance as it applies to a general case, those already familiar with the topic may wish to jump ahead to Chapter 2 where we will focus more on xenon and how we can exploit its behavior in situ to gain additional information not available by traditional NMR. For a more indepth discussion of NMR and MRI the reader is referred to Keeler [8] or Levitt [9].

1.1.1 Nuclear Spin

In 1922 Stern and Gerlach discovered that particles have a magnetic moment (μ) by firing silver atoms though an inhomogenous magnetic field and observing different deflections corresponding to different spin angular momentum (S). μ can be calculated as follows:

$$\mu = \gamma S = \gamma \hbar I, \tag{1.1}$$

where the gyromagnetic ratio (γ) is an intrinsic property of the nucleus and $\hbar$ is the reduced Planck's constant with I representing the nuclear spin angular momentum ($\frac{1}{2}$ for protons and ^{129}Xe).

Commonly used γ values as well as those pertinent to this thesis are shown below in 1.1.

Nucleus	Spin Number	Gyromagnetic Ratio (rad sec^{-1} T^{-1})
^{1}H	1/2	267.522
^{2}H	1	41.066
^{13}C	1/2	67.283
^{15}N	1/2	-27.126
^{129}Xe	1/2	-74.521

Table 1.1: Gyromagnetic ratios for commonly used isotopes in NMR

The gyromagnetic ratio is proportional to the energy difference between the + and - spin states for a spin 1/2 nucleus when placed in a magnetic field (B_0) so that the field is described as (0, 0, B_0) in the right-handed coordinate system if B_0 is along the z-axis, as shown in 1.1. This is known as the Zeeman Splitting. The Hamiltonian representing a single spin in this system is given by:

$$H = -\gamma B_0 I_z \tag{1.2}$$

and given that I_z can be written at $m\hbar$ with m=$\pm\frac{1}{2}$ the eigenvalue for the energy of a single spin in a magnetic field is represented by,

$$E_m = -m\hbar\gamma B_0 = \pm\frac{1}{2}\hbar\gamma B_0, \tag{1.3}$$

Isidor Rabi from Columbia University discovered you could use radio waves to provoke nuclear spin flips in 1944; this would go on to be the basis behind NMR [10]. That work

would later be expanded by Bloch, Hansen and Packard to detect the protons in water molecules using inductive detection [11]. Typically the energy of a system is defined as E $= -\mu \cdot B_z$, where B_z is applied along the z-axis and the negative sign indicates that the prefered state is parallel to the field. For NMR we replace μ with $\gamma\hbar I_z$ as shown from the energy equation 1.3. From this we can define our Larmor frequency,

$$\omega_0 \equiv -\gamma B_0 \tag{1.4}$$

so in a magnetic field the Zeeman splitting can be written as a function of the Larmor frequency for that spin,

$$\Delta E = -\gamma\hbar B_0 = \hbar\omega_0 \tag{1.5}$$

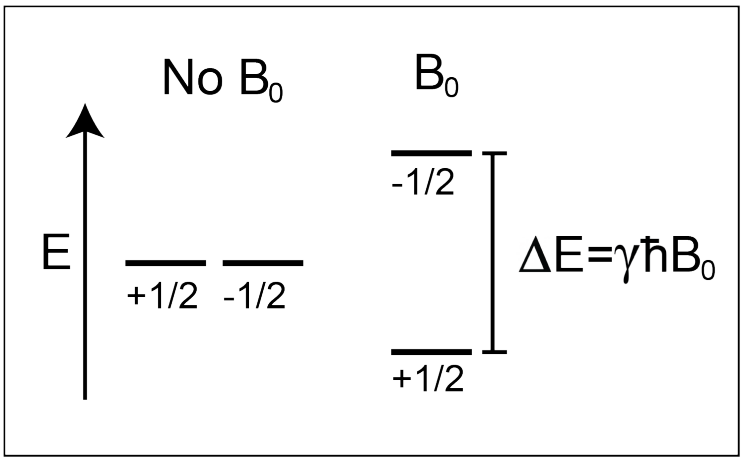

Figure 1.1: Energy levels for the different spin states split in a magnetic field where the spin aligned with the field decreases in energy and the antiparallel spin increases in energy [8].

A larger gyromagnetic ratio benefits by having a larger Zeeman splitting. The detection of NMR depends on having a population difference between the +1/2 and -1/2 spin states that can be perturbed using radiowaves. We will use ^{1}H NMR as an example.

1.2 ^{1}H NMR

The bulk of NMR techniques focus on the presence of protons either on the molecule of interest or in water. ^{1}H NMR is one of the key techniques used in organic chemistry for determining chemical structure and monitoring a synthetic process. Small changes in the local magnetic field experienced by a proton, from electron density in a bond for instance,

will change the Larmor frequency (ω_{eff}) and can be detected as different chemical shifts, with values typically given in parts per million (δ(ppm)) defined as,

$$\delta(ppm) = \frac{\omega_{eff} - \omega_{ref}}{\omega_0} \times 10^6, \tag{1.6}$$

While chemical shift defined in this way is not dependent on B_0, going to higher field does increase the resolution of the spectrum by increasing the absolute frequency difference between two signals. The question remains: where does this signal come from?

1.2.1 Magnetization

Once placed in a magnetic field we can determine the magnetization (M_0) of the sample given by,

$$M_0 = N_s \gamma \hbar P, \tag{1.7}$$

where N_s is the number density of spins and P is the polarization or population difference. P is given by the excess of spins in one direction (in this case aligned with the field or α) which is typically very small under thermal equilibrium on the order of a few ppm, making NMR and MRI relatively insensitive techniques, and is given by the Boltzmann distribution [9],

$$P = \frac{\alpha - \beta}{\alpha + \beta} = \frac{e^{\frac{\hbar\gamma B}{2k_B T}} - e^{\frac{-\hbar\gamma B}{2k_B T}}}{e^{\frac{\hbar\gamma B}{2k_B T}} + e^{\frac{-\hbar\gamma B}{2k_B T}}}, \tag{1.8}$$

where k_B is the Boltzmann constant and T is the temperature. The energy difference between the +1/2 (α) and -1/2 (β) states is very small so the polarization can be approximated as,

$$P \approx \frac{\gamma \hbar B_0}{2kT}, \tag{1.9}$$

Combining our magnetization with this approximation for the polarization we can roughly calculate our magnetization using,

$$M_0 = \frac{N_s \gamma^2 \hbar^2 B_0}{4kT} \tag{1.10}$$

Based on this equation we can see that decreasing the temperature or increasing the static magnetic field can both be used to increase the polarization. ^{1}H NMR of water is also aided in that for water the proton concentration is 110 M so N_s is very large. In other systems however, N_s isn't so gratuitously large, and so we must use optical pumping techniques to create a nonequilibrium spin polarization, such as using laser-polarized Rb atoms for ^{129}Xe [12].

1.2.2 The Vector Model

While spin is an inherently quantum mechanical property, once in a magnetic field the magnetization can often be described by a classical vector model. This allows us to understand the NMR experiment in simplisitic terms without getting bogged down in the quantum mechanics. The goal of most NMR experiments is to perturb the magnetization away from equilibrium and detect it as it relaxes. We will be using the rotating frame to discuss the vector model where we assume the frame of reference is fixed with the radio frequency (RF) pulse at -ω_{ref}.

From equation 1.10 we know what controls the amount of magnetization we accumulate in a static field, while lowering the temperature can be used in certain cases [13] [14] it is more common to push towards higher magnetic fields. For a simple pulse acquire experiment a B_1 field is applied typically along the x-axis which will rotate the magnetization down into the xy-plane where it can be detected as shown in 1.2. Once the magnetization is moved into the xy-plane it will undergo relaxation while precessing around the static magnetic field (z-axis) and the magnetization will begin to build back up along the z-axis.

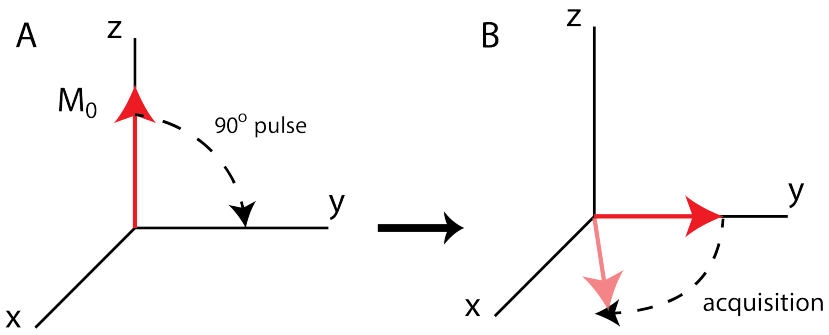

Figure 1.2: A) Initially the net magnetization is along the z-axis. Then an applied field along the x-axis rotates the nuclear magnetization into the xy-plane. B) In the xy-plane the magnetization precesses around the z-axis and can be detected.

A pulse applied along -x will change the field experienced by the spins to B_{eff} = (B_1,0,ΔB_0), where ΔB_0 is the residual field along the z-axis. This additional field will cause the spin to precess around the -x axis towards the y-axis. The angle of the rotation, β is determined by the strength of the B_1 field and the length of the pulse,

$$\beta = \frac{1}{2}\gamma B_1 \tau \tag{1.11}$$

Where τ is the time the B_1 field is applied. When $\beta = \frac{\pi}{2}$, τ is often referred to as the 90 time. By controlling the strength and length of the RF pulse we can move the magnetization to the xy-plane or invert it to the -z axis. The precession of the spins in the xy-plane is inductively detected by a receiver coil placed perpendicular to the static field. The resulting free induction decay (FID) is then Fourier transformed into the recognizable

NMR spectrum. A Fourier transform takes a function of time and decomposes it into the individual frequencies that make it up. This allows us to acquire a time dependent free induction decay which can correspond to many spins in a system then decompose that time dependent signal into the corresponding frequencies from the spins in our sample [15]. The Fourier transform is given below in 1.12.

$$F(\omega) = \int_{-\infty}^{\infty} f(t) e^{-i2\pi\omega t} dt \tag{1.12}$$

The rate at which the spin precesses around the z-axis is determined by its Larmor frequency and so if a sample contains many spins with different Larmor frequencies then they will all precess at different rates. Erwin Hahn discovered that you could use a 180^o degree pulse to refocus the magnetization in the xy-plane, this is called a Hahn Echo or spin echo shown below in 1.3 [16].

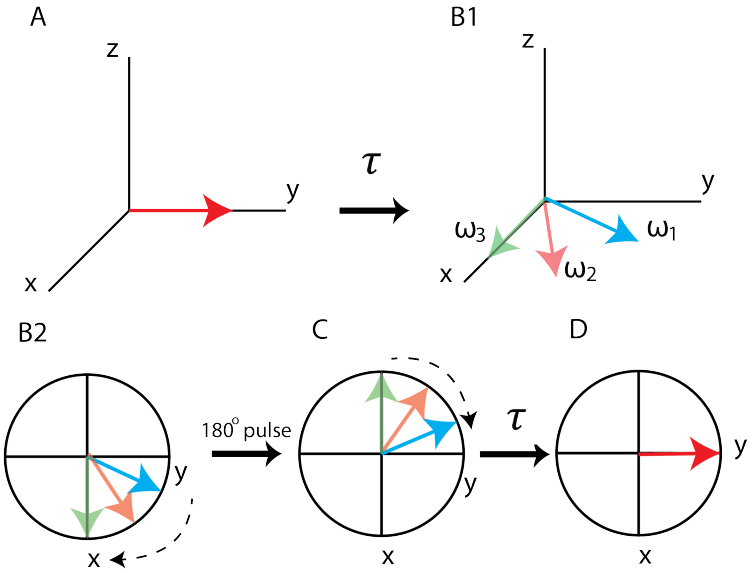

Figure 1.3: A) Magnetization has been rotated into the xy-plane B1) The magnetization begins to precess around the z-axis for a time τ at different rates for ω_1, ω_2, and ω_3. B2) Move to an overhead view of the xy-plane. C) a 180^o pulse is applied flipping the magnetizations over the y-axis. D) They continue to precess for a time τ and all return to the y-axis together at the same time.

1.2.3 Relaxation

There are two types of relaxation to consider in a typical NMR experimment, longitudinal (T_1) and transverse (T_2). The longitudinal relaxation is the retuen to the thermal distri-

bution of the spins along M_z. After an initial inversion of the equilibrium, magnetization is given by,

$$M_z(t) = M_{z,eq}(1 - e^{\frac{-t}{T_1}}) \tag{1.13}$$

This exponential return to equilibrium is characterized by the time constant T_1. This relaxation is often referred to as"spin-lattice relaxation" as it is caused by the exchange of energy between the spins and the surrounding system. The rate of T_1 relaxation defines the minimum amount of time you need to wait between experiments to ensure the magnetization has fully returned to the z-axis.

Once in the xy-plane transverse magnetization begins to decay exponentially characterized by T_2 according to,

$$M_{xy}(t) = M_{xy,t=0}(e^{\frac{-t}{T_2}}) \tag{1.14}$$

A special case of this effect called T_2^* is demonstrated in 1.3 where the Larmor frequencies of many spins spread out over a time τ due to interactions with neighboring spins that act as tiny dipoles. This is commonly referred to as"spin-spin relaxation." This loss of coherence between spins can also be due to inhomogeneities in the magnetic field, such that chemically equivalent spins experience different B_{eff} fields. While dephased the magnitude of the transverse magnetization vector decreases. The inclusion of magnetic field inhomogeneities gives the value T_2^*. This is not a true relaxation mechanism and can be removed using an echo as shown in 1.3.

Figure 1.4 shows the two types of relaxation where the longtiduinal relaxation is returning the polarization to the M_z axis and the transverse relaxation is the magnetization decaying away from the xy-plane.

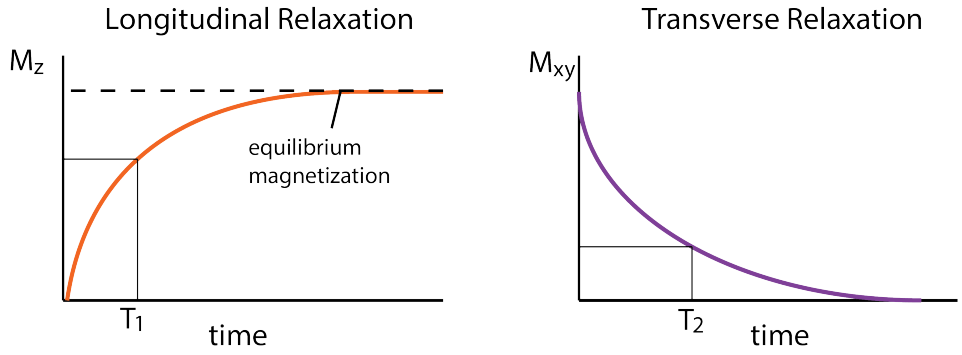

Figure 1.4: Curves showing the two types of relaxation, longitudinal where the magnetization returns along the z-axis, and transverse where the magnetization decays away from the xy-plane.

T_2 is necessarily shorter then T_1 for a system; if it were not then you would end up with the same amount of magnetization in the z-axis that you started with while some still

remained in the xy-plane. These relaxation times can be useful tools for generating contrast between different types of spin in the same sample, if one spin relaxes very rapidly and the other slowly by adding a delay before your acquisition you can selectively observe the slow relaxaing spin.

T_2 can be measured using the spin echo experiment described in 1.3, while T_1 can be measured using an inversion recovery experiment where you invert the magnetization onto -z then wait a time τ before flipping it into the xy-plane to detect varying τ over multiple scans. The pulse sequences for these as well as the simple pulse acquire are shown in 1.5.

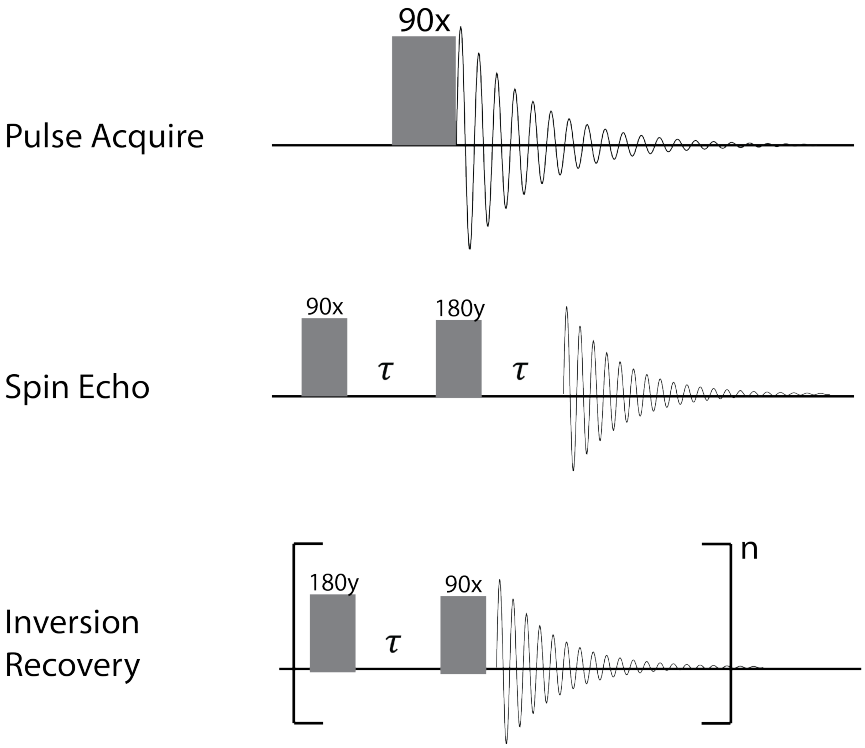

Figure 1.5: Pulse sequence schematic for the basic pulse acquire, spin echo, and inversion recovery experiments.

Now that we have an understanding of what is happening during a simple NMR experiment we can look at a spectrum one might acquire and see the various features.

1.2.4 the NMR spectrum

The signal acquired in NMR is in Hz but is often displayed in ppm, as that doesn't change based on the static magnetic field used. Different nuclei have different ppm ranges over which their chemical signals typically occur. The chemical shift ranges for common NMR active nuclei are shown in table 1.2.

Nucleus	ppm Range
^{1}H	-1 - 12
^{2}H	-1 - 12
^{13}C	0 - 220
^{15}N	0 - 800
^{129}Xe	-400 - 7500*

Table 1.2: Chemical shift ranges for common NMR nuclei. *relative to the Xe gas peak

For smaller nuclei like hydrogen the chemical shift range is quite small only 13ppm total, while for xenon, the largest nucleus shown, the range is more than 400 times that at around 8000ppm [17] [18]. A larger chemical shift range means that different chemical environments can be more spread out and easily distinguishable. The simulated ethanol spectrum in 1.6 shows some typical features of a ^{1}H NMR spectrum. Adjacent carbons with hydrogens on them will cause splitting of the peak due to^{1}H-^{1}H J-coupling. The methyl group has a carbon with two hydrogens adjacent to it so the signal generated by the three methyl hydrogens, which are all equivalent, is split into three different peaks as the hydrogens on carbon-2 can be either ↑↑, ↑↓, or ↓↓, if we consider ↑↓ and ↓↑ to be equivalent in energy. This sensitivity makes ^{1}H NMR great for determining molecular connectivity.

The intensity of the peak, or more accurately the integrated area, can also give you an idea of how many protons are contributing to each signal. If we set the integrated area for the alcohol peak to 1 (as it has the smallest integrated area) then we would see the integration for the quartet ≈2 and the integration for the triplet ≈ 3.

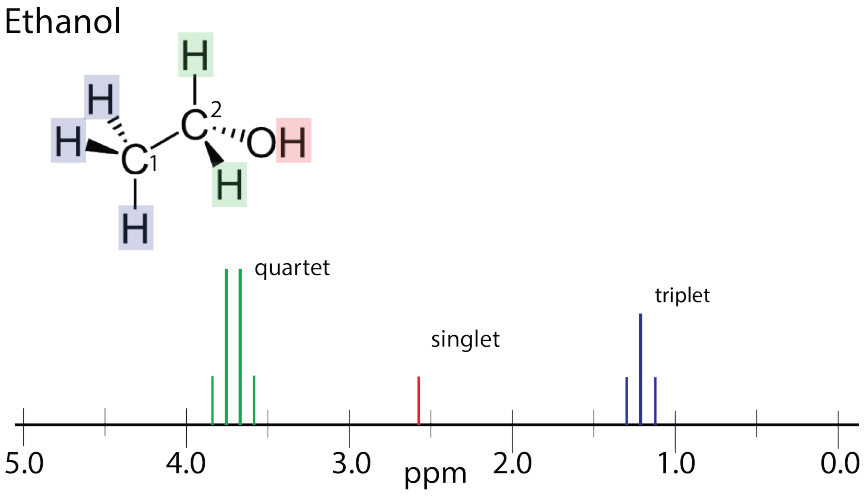

Figure 1.6: Ethanol produces peaks corresponding to three different chemical environments, a singlet around 2.6 ppm (red) from the alcohol group, a quartet 3.7 ppm (green) from the hydrogens on carbon-2 and a triplet around 1.2 ppm (blue)from the hydrogens on carbon-1.

For many samples the complexity of a ^{1}H NMR spectrum provides useful information on structure and conformation, but that type of information is not always necessary. ^{129}Xe NMR removes this complexity and instead only shows peaks cooresponding to Xe atoms in a unique chemical environment. This allows for the development of yes/no type sensors. Background specific to xenon NMR is given in chapter 2.

Chapter 2

^{129}Xe NMR Spectroscopy

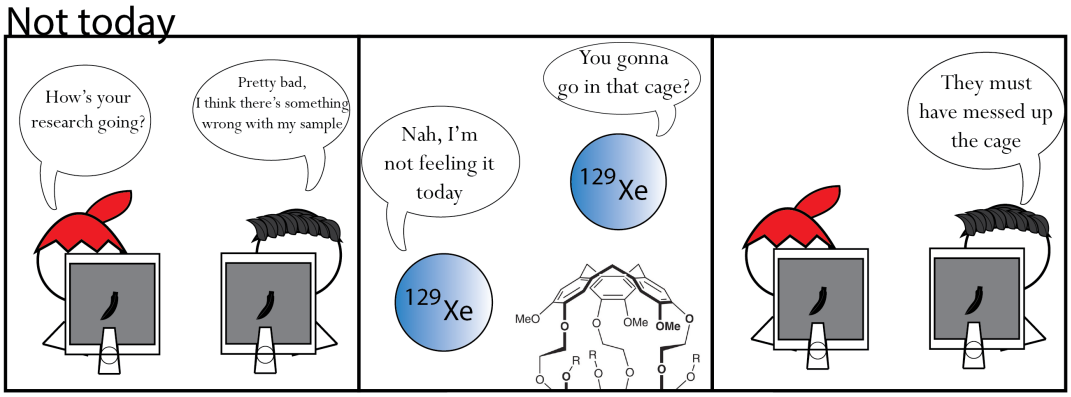

The usefulness of NMR stems from the non-invasive and non-destructive nature of the technique. Proton NMR has some distinct advantages, due to its ability to show connectivity and structural information, but there are systems where the proton spectrum can get very complicated. Being a highly insensitive technique; the presence of a large water signal can also inhibit detection at low concentrations of molecular targets. ^{129}Xe NMR is an excellent choice for studying systems where a yes/no indication is preferable or where you want your reporter to interact directly in some way with the system. The lack of background signal from xenon, as it exists naturally in only trace concentrations, means that any detected signal is generated experimentally and high contrast can be obtained with only a small population of gas atoms.

Xenon was successfully seperated from krypton in 1898 [19] and used in high-speed photography to produce 1-2 μs light pulses [20]. It was discovered to be an anesthetic at high concentrations ($\sim$35%) by Stewart C. Cullen in 1951 [21]. This study laid the ground work for demonstrating the biocompatibility of xenon, which would eventually lead to it being used to image void spaces in the body such as the lungs, something not easily done using proton NMR. Building off the infrastructure of traditional magnetic resonance imaging (MRI), a technique first utilized by Lauterbur in 1973 [22], xenon MRI was used in 1994 by

Albert et al. to image an excised mouse lung [23]. This work showed xenon could be used as an alternative to expensive ^{3}He gas for imaging gas filled cavities. Xenon has a second NMR active isotope (^{131}Xe) with a spin=$\frac{3}{2}$ used in quadrupolar relaxation studies [24]. Furthermore xenon is able to be hyperpolarized through spin exchange optical pumping (SEOP) and functionalized through host-guest interactions with molecular cages. In this chapter we will outline the properties of xenon as an NMR based detector and different approaches to xenon NMR.

2.1 Physical Properties of Xenon

^{129}Xe the spin $\frac{1}{2}$ NMR active isotope has a relatively high natural abundance at 26.4% [25]. When compared to ^{3}He another NMR active inert gas (natural abundance 0.000136%) it's easy to see why working with xenon would be preferrable. Xenon is found in air at 87 ppb and has a molar mass of 131.293 g/mol with a van der Waals radius of 260 pm (43 Å^3). The large electron cloud of xenon makes it highly polarizable, which is why it has such a large chemical shift range as the local electronic environment can significantly change the electron distribution around the nucleus. Xenon condenses at 165 K and freezes at 161 K, so large quantities of hyperpolarized xenon can be collected in the solid phase by flowing through a liquid nitrogen (∼77 K) cooled system.

2.2 Solubility

One of the most important properties to look at is xenon's solubility in different solvents and suspensions (such as blood). The amount of xenon dissolved in water can be calulated using [25],

$$lnX_1 = A + B/T^* + ClnT^8 \tag{2.1}$$

where X_1 is the mole fraction of xenon in water, T^* is T/100 for the temperature in Kelvin, and the constants A, B, and C are empirically defined to be A = -74.7398, B = 105.201, and C = 27.466 giving a mole fraction for xenon in water at 25 ^{o}C to be 7.890 x 10^{-5}. For a noble gas xenon is quite soluble in water with an Oswald coefficient of 0.11, meaning at 25^{o}C and 1 atm pressure, 110 mL of xenon gas will dissolve in 1 L of water [1], this is 11.7 times higher than that of helium (0.00939). This means for a typical NMR sample (∼500μL) there will be 55μL of xenon dissolved in the sample, and 14.24μL of ^{129}Xe. This solubility gets better in organic solutions, table 2.1 shows the solubility in a variety of liquids.

Using our mole fraction calulation for xenon we can calculate the actual concentration of xenon ([Xe]$_w$) using,

$$[Xe]_w = (pXe)(\frac{P + 14.7}{14.7})[H_2O]X_1 \tag{2.2}$$

Liquid	Oswald solubility	Temperature
water	0.11	25^{o}C
hexane	4.8	25^{o}C
benzene	3.1	25^{o}C
dimethylsulfoxide (DMSO)	0.66	25^{o}C
water	0.0834	37^{o}C
blood plasma	0.10	37^{o}C
blood	0.14	37^{o}C

Table 2.1: Oswald solubilities for common solvents at room temperature (25^{o}C) and human body temperature (37^{o}C) [1] [2], Oswald coefficient is defined as the volume of a gas that dissolves in 1 unit of a liquid at a given temperature.

where pXe is 0.02 (the percentage of xenon in our mixture), P is the over pressure of gas in psig, [H_2O] is the concentration of water, and X_1 is our calculated mole fraction of xenon in water at 1 atm and 25 ^{o}C. For a typical experiment at 60 psig the concentration of xenon in water is 446 μM.

In general the solubility of a noble gas will decrease as the temperature of the system increases. Xenon is hydrophobic given that it can't form any hydrogen bond, or long lived dipole-dipole interactions so its solubility increases as the hydrophobicity of the solvent increases. This makes xenon an excellent reporter for looking at organic systems such as liquid crystals where the macromolecular host can interact with the environment and be detected by xenon. The solubility in water is sufficient for conducting a wide array of xenon based detection experiments, and generally we will be more limited by the solubility of the molecular host than by xenon itself.

2.3 Hyperpolarized Xenon NMR

Xenon can undergo spin exchange optical pumping (SEOP) to acheive polarization levels far greater then thermal polarization (up to 50,000x signal enhancement). Optical-pumping using rubidium (Rb) involves stimulating the transition between the m_j=$-\frac{1}{2}$ sublevel of the $^2S_{\frac{1}{2}}$ state to the m_j=$+\frac{1}{2}$ sublevel of the $^2P_{\frac{1}{2}}$ state known as the D1 transition. This is done using circularly polarized light ($\sigma+$) and a weak magnetic field to break the degeneracy of states. When abosrbing the light the system also absorbs the angular momentum of the light so electrons in the m_j=$-\frac{1}{2}$ sublevel transition to the m_j=$+\frac{1}{2}$ sublevel, but electrons already in the m_j=$+\frac{1}{2}$ sublevel cannot absorb the light because there is no sublevel with an additional +1 angular momentum. This causes selective driving of the D1 transition in Rb, shown in 2.1. Once the Rb electronic state is polarized to the m_j=$+\frac{1}{2}$, $^2P_{\frac{1}{2}}$ state it undergoes spin-exchange with xenon gas via collisions and hyperfine interactions. The polarization from the valence electron of the rubidium atom is transferred to the nucleus of the xenon in the presence of an N_2 buffer gas. For a more detailed explanation of optical

pumping I refer the reader to reference [26]

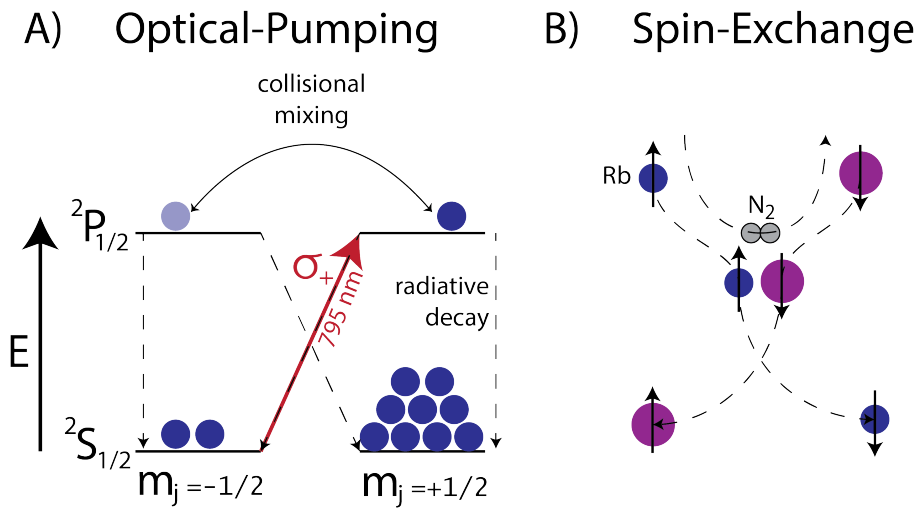

Figure 2.1: Spin Exchange Optical Pumping (SEOP) A) circularly polarized light pumps the D1 transtion of the Rb atom to the m_j=+$\frac{1}{2}$, $^2P_{\frac{1}{2}}$ electronic state then B) Spin Exchange occurs between ^{129}Xe atoms and the valence electron of the Rb atoms

2.3.1 Dissolution of Hp-^{129}Xe

Once polarized the xenon signal is dramatically increased as shown in 2.2. The xenon spectrum is less complex than typical proton spectra because each peak in the spectrum represents xenon in an unique electronic environment, instead of multiple peaks arising from a single molecule. In 2.2 we are looking at the xenon gas peak which is typically referenced to 0 ppm. Dissolution of the xenon into solution after polarization is done by bubbling into solution through a capillary at the bottom of our sample as shown in 2.3. Typically, samples are perfused with xenon by bubbling for 10 to 30 seconds followed by a short settling time before the acquisition pulse is started. This allows nondissolved gas, which can cause inhomogeneous broadening, to leave the solution before the spectrum is acquired. The Xe@water peak is seen at 191 ppm with the gas peak referenced to 0 ppm. The expected chemical shifts for xenon in various environments is shown in 2.4. The peaks for cucurbiturils (CB6 and CB7) are very wide and appear in the range of 80 ppm to 120 ppm. While exciting that we can get hyperpolarized xenon into solution we still need to modify our system in some way such that the information we obtain by xenon NMR is useful, this functionalization comes in the form of using macrocycles as molecular cages for xenon.

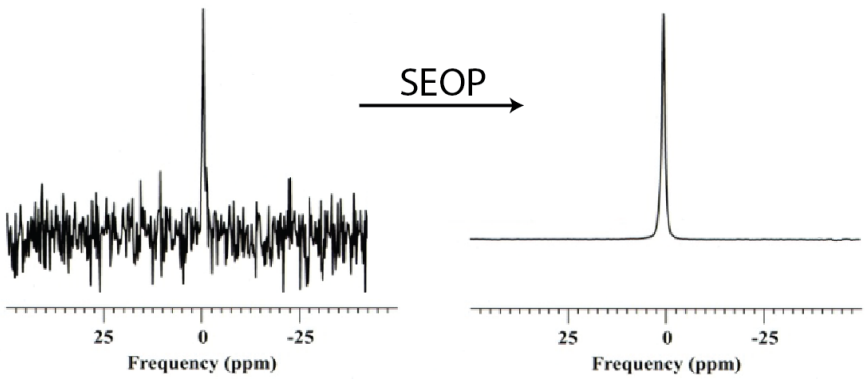

Figure 2.2: The left spectrum was taken using thermally polarized xenon gas and the right was taken after hyperpolarization affording a 50,000x enhancement in signal to noise

2.4 Macrocycles as Molecular Cages

Macrocycles are large molecular structures with a hollow cavity that xenon can exchange in and out of. This host-guest relationship, where the cage is the host and xenon is the guest, allows us to obtain a chemical signature from the xenon both in and out of the cage. Macrocycles can be modified to interact with components of the chemical environment generating two distinct signals, one where the host is interacting with its target, and one where it is not. Macrocycles also allow for the use of chemical exchange saturation transfer (CEST) which combined with hyperpolarized xenon (hyperCEST) can detect macrocycle concentrations much lower then traditional NMR experiments [30]. At higher concentrations the xenon inside the molecular cage (Xe@Cage) peak can be directly detected using a simple pulse acquire sequence. A 1998 study shows the ideal packing coefficient for a molecular cage is 55% [31]. Given xenon's van der walls volume of 43 $Å^3$, that means the ideal host would have an internal volume of 76 $Å^3$.

2.4.1 Cryptophanes

Cryptophanes are a class of molecular cages consisting of two cyclotriveratrylene caps connected by alkoxy linkers that can vary in length. They are classified by their linker length and whether they are in the *anti* or *syn* confirmation. Cryptophane-A (CryA) shown in 2.5 is the most commonly used macrocycle for studying systems with xenon NMR. CryA is in an *anti* confirmation and has an internal volume of 95 $Å^3$ (45% occupied by xenon) such that it will host only one xenon atom at a time [32] and has a binding constant K=17400 M^{-1} in water at 298 K [33]. This compound can exhibit diastereomeric properties when further functionalized. While CryA is difficult to synthesize, the acid side groups allow for functionalization making them incredibly versatile in their applications. CryA sensors used

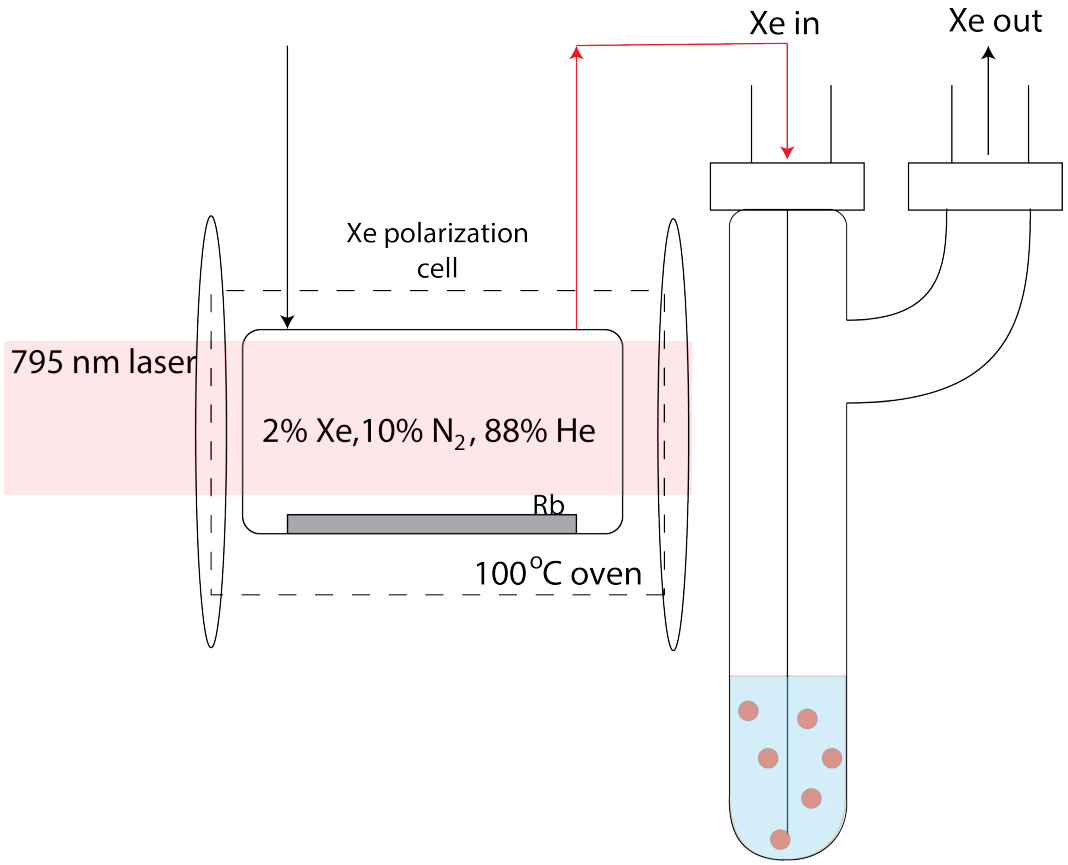

Figure 2.3: The mixture of 2%Xe, 10%N_2, and 88%He flows into a cell containing Rb heated to 100^{o}C in a small magnetic field where it undergoes SEOP, then flows out and is bubbled into the sample.

in this thesis have a solubilizing backbone of amino acids and a targeting group which can be varied.

CryA has an interesting property that once functionalized with a chiral group such as a peptide the cage becomes diastereomeric, and the xenon is so sensitive to its environment that the different chiralities of the cage manifest as two seperate peaks in the ^{129}Xe NMR spectrum. Previous studies found that xenon can detect chiral differences up to 10 bonds away with each diastereomer giving a slightly different chemical shift [34].

In order for CryA to be useful in Xe NMR the xenon has to bind the cage, but the interaction has to be weak enough that depolarized xenon can leave the cage and be replaced by new polarized xenon. The dynamics of this host-guest interaction have been well studied [35], [36], [37]. The equilibrium for this system is given by

$$Xe + cage \leftrightharpoons Xe@cage, \tag{2.3}$$

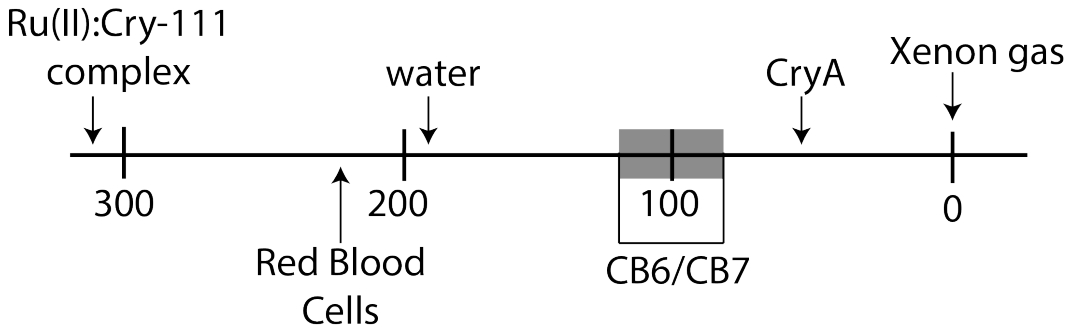

Figure 2.4: ^{129}Xe chemical shifts when bound to relevant macrocycles and complexes compared to Xe@water and Xe gas, taken from references [27], [17], [28], [29]

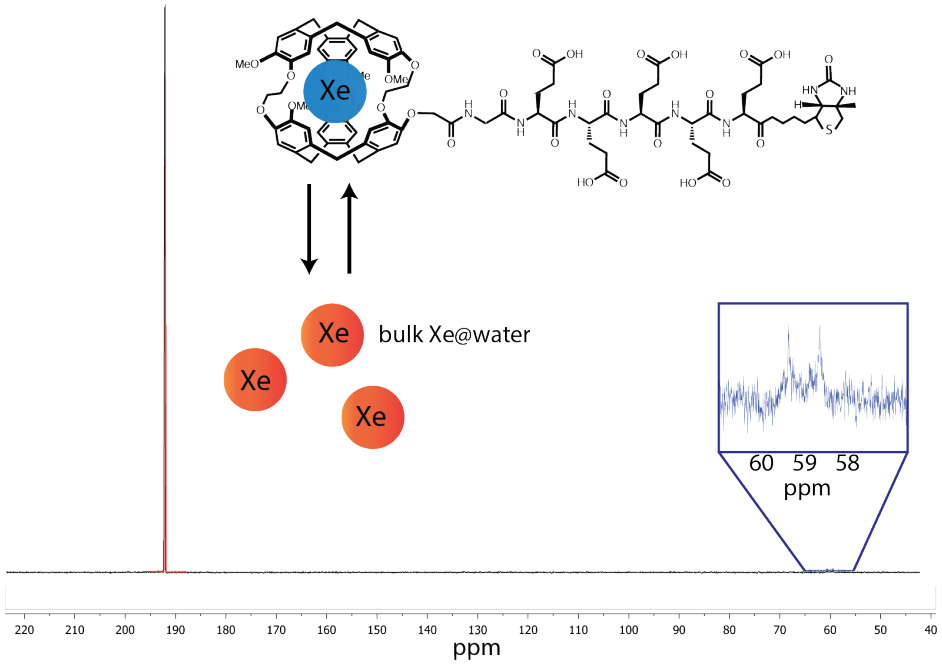

Figure 2.5: A cryptophane cage with a solubilizing linker and biotin as the targeting moiety showing the dissolved xenon peak at 191 ppm and diastereomeric cage peaks around 59 ppm.

$$K = \frac{[Xe@cage]}{[Xe][cage]} \tag{2.4}$$

shere Xe@cage is xenon in the cage. Having a high value for K means a significant portion of the cages in solution are hosting a xenon atom which makes for better detection.

To estimate this we can define,

$$[cage] = [cage]_i - [Xe@cage], \tag{2.5}$$

with $[\text{cage}]_i$ the total cage present and we will assume that the total amount of xenon ($[\text{Xe}]_i$) is in excess, so the fraction of bound xenon is very small such that,

$$[Xe] = [Xe]_i - [Xe@cage] \approx [Xe]_i. \tag{2.6}$$

With these we can approximate the fraction of occupied cage by,

$$\frac{[Xe@cage]}{[cage]_i} = \frac{K[Xe]_i}{1 + K[Xe]_i}, \tag{2.7}$$

With this the fraction of occupied cage can be calculated by knowing the binding constant K and the concentration of xenon in solution. The K for CryA at 25 ^{o}C is 17400 M^{-1} and our $[\text{Xe}]_w$ is 446 μM giving 88.6% occupied with our approximation.

The rate of exchange can be determined from the line width ($\Delta\nu$) of the Xe@CryA peak using the equation,

$$k_{ex} = \pi\Delta\nu. \tag{2.8}$$

This linewidth was empirically determined [38] to be,

$$k_{ex} = 0.738e^{0.147T} \tag{2.9}$$

The time it takes for xenon to exchange in and back out of CryA has been found to be 32 ms at room temperature (25^{o}C) and that is the value we will use for the remainder of this thesis [39].

2.4.2 Cucurbiturils

Recently cucurbiturils have become a popular macrocycle for xenon studies in particular due to their fast exchange dynamics which makes them a potent hyperCEST agent. They lack an easy way to be directly functionalized which has been an obstacle in finding useful applications. Cucurbiturils come in varying sizes CBn where n indicates how many repeated subunits make up the ring and a larger number indicates a larger internal volume as shown in 2.6.

The size of the cucurbituril has significant effects on its xenon exchange properties. The various sizes and structures are shown in table 2.2. The difference between the annular width and the equatorial width is about 2 Å, which creates a constrictive binding pocket [3] ideal for catalyzing reactions such as the formation of rotaxanes. The earliest rotaxane structures were synthesized based on the statistical probability that two dumbell shaped molecules would react in the presence of a macrocycle, locking it in place [40].

The different volumes of CBn's means they can bind a wide variety of targets including xenon. β-cyclodextrin (β-CD) is also listed as a comparison to cucurbiturils, where it has

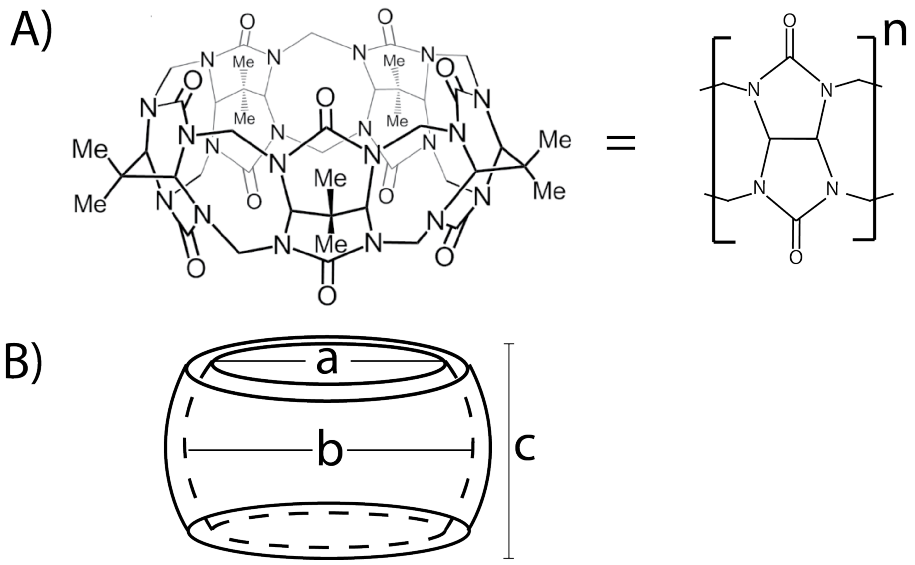

Figure 2.6: A) structure of cucurbit-5-uril (CB5) with 5 basic subunits in a ring B) functional structure of the cage with a being the diameter of the openings made by the ketone groups, b being the internal volume, and c being the height of the structure. For specific values please refer to table 2.2

CBn	a annular width Å	b equatorial width Å	c height Å	V Å^3	packing coeff.
CB5	2.4	4.4	9.1	82	52.4%
CB6	3.9	5.8	9.1	164	26.2%
CB7	5.4	7.3	9.1	279	15.4%
CB8	6.9	8.8	9.1	479	9.0%
β-CD	6.0	6.5	7.9	262	16.4%

Table 2.2: CBn structural data [3]

an annular width between CB7 and CB8 and an equatorial width between CB6 and CB7. Previous work has shown CB6 as a viable candidate for xenon hyperCEST, [39] finding CB6 in water has an exchange rate, k = 2100 s^{-1} (exchange time of 0.4 ms) and a binding constant, K$_A$= 2500 M^{-1}, much lower than CryA. Based on the value of 55% being the optimal occupation volume of xenon in its macrocyclic host, it would appear that CB5 would be the best candidate for xenon NMR, but due to slow exchange times it is not useful for hyperCEST and a significant wait is necessary between transients to acquire good signal-to-noise (SNR).

2.4.3 HyperCEST

Proton chemical exchange saturation transfer (CEST) has been investigated for use in MRI both as PARACEST [41] and DIACEST [42] [43] as a unique way of looking at proton exchange. Traditional CEST agents are molecules that exchange protons with the bulk water, while PARACEST involves the exchange of individual protons or entire water molecules that coordinate to a paramagnetic center. These techniques are powerful due to the large reservoir of water naturally present in many samples, but much like traditional NMR experiments in complex mixtures where many different protons may be exchanging, these spectra can get complicated. We can overcome the signal loss from not using water by hyperpolarizing xenon giving up to 5 orders of magnitude signal enhancement.

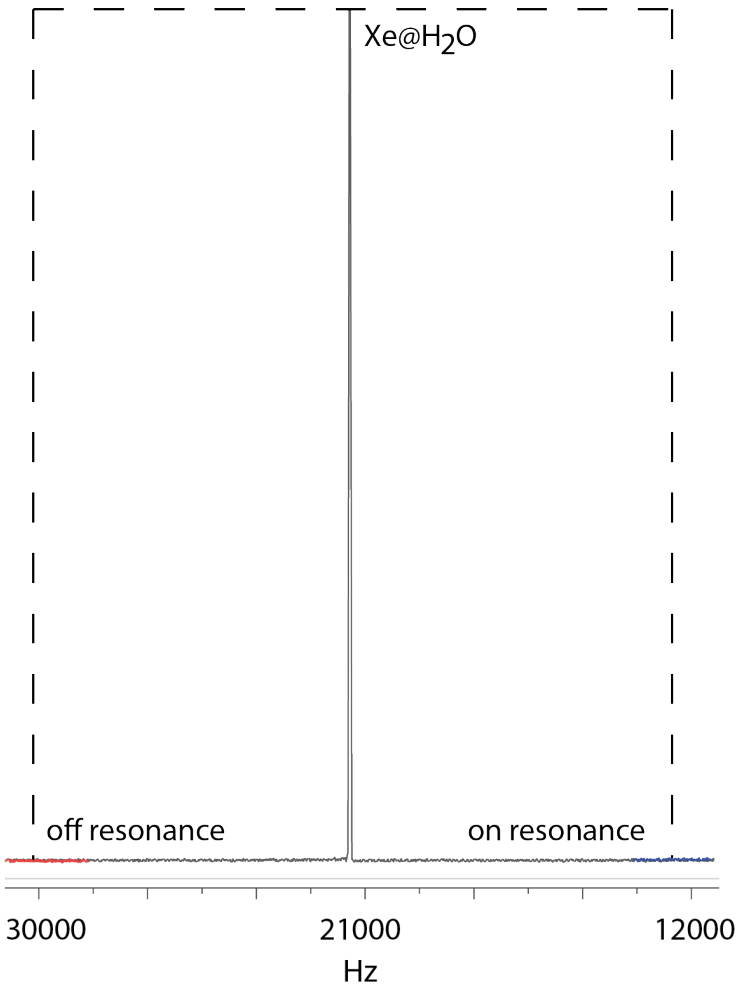

Figure 2.7: For a blunt sensor where you know the chemical shift of the Xe-cage complex of interest you can do a simple on/off resonance saturation and look for changes in the Xe@H_2O peak. Typically the off resonance is chosen to be equidistant on the other side of the dissolved xenon peak so that any overlap between the saturation pulse and the dissolved peak will be equal for the on and off resonance saturations.

For hyperCEST, or CEST using hyperpolarized xenon, effectiveness depends on two properties, the xenon association constant for the cage, K_A, and the xenon exchange rate, k_{BA}. For good hyperCEST signal you want both of these to be high, *i.e.* a large percentage of the cages are occupied by xenon at any given time, and xenon exchanges in and out of the cage very rapidly. Unfortunately these two properties are typically inversely related, as a high K_A is generally associated with a tighter binding of the xenon which causes a slower exchange. The most basic hyperCEST experiment involves saturating where you expect the NMR signal for a Xe-cage complex to be (on resonance) and then saturating an equal

distance on the opposite side of the bulk dissolved xenon peak (off resonance), a change in the dissolved peak will indicate the presence of the Xe-cage complex as shown in 2.7

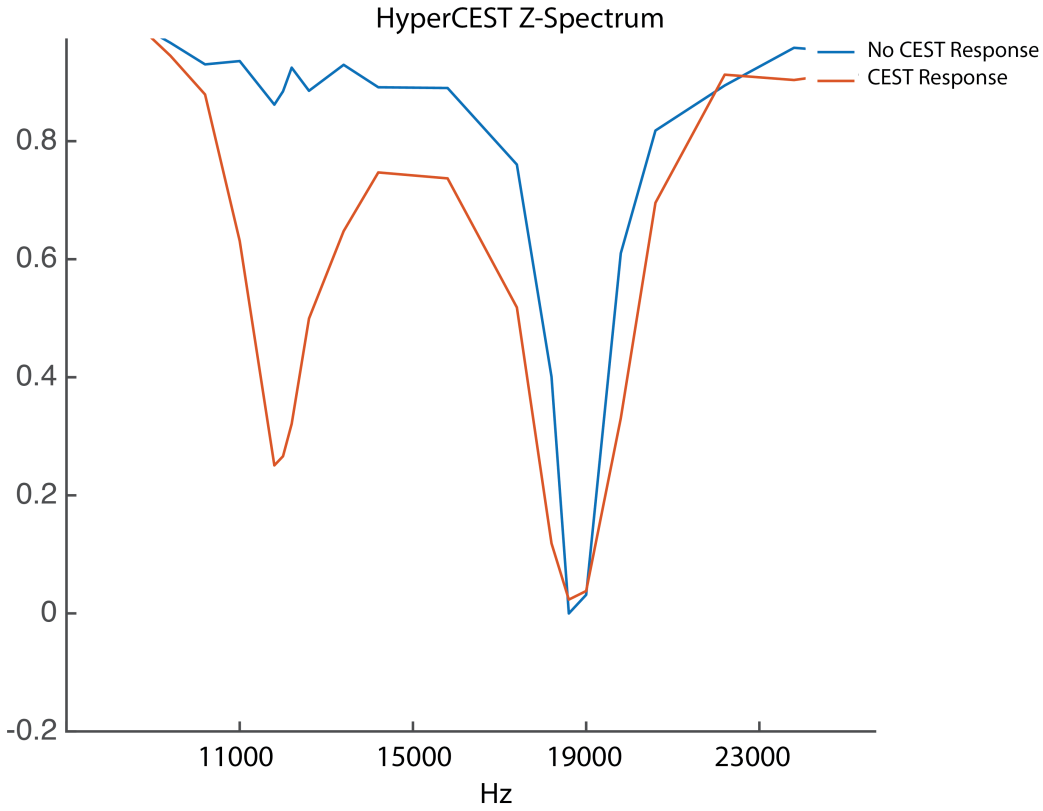

Figure 2.8: A z-spectrum for a xenon hyperCEST experiment where the saturation frequency was stepped between 9000 and 23000 Hz with a CEST response occuring at 11500 Hz with a cucurbituril present and no CEST response without a cage present. The dip at 19000 Hz corresponds to the Xe@water peak.

More complex hyperCEST experiments, where you may not know the exact chemical shift of the xenon in the cage, involve stepping saturation pulses over a frequency range and observing changes in the dissolve xenon peak, the peak should get smaller when the saturation is over the range where the Xe@Water peak occurs and also where the Xe@Cage peak occurs as the xenon in the cage will be depolarized by the saturation pulse then exchange back out into solution [30]. This technique retains chemical shift information making it an ideal way to amplify signal in a system with a reversible xenon binding pocket. An example of the z-spectrum from a system with a molecular cage and one without are shown in 2.8. Having a low concentration ^{129}Xe pool that is highly polarized allows for saturtion of exchanging xenon to have measurable changes in the observed xenon signal.

Z-spectra can be useful in many different ways. For rapidly exchanging macrocycles the width of the Xe@water peak will change depending on the macrocycle concentration. This

means even if you don't know where to saturate to find the cage peak, or your steps are spaced too far apart and you miss the peak, an observed change in the water peak can indicate the cage's presence. In 2.9 we see four different concentration of CB6 in solution and how it affects the width of the water peak. The difference between 10 and 100 nM is relatively small, but once we increase to 500 nM and 1 μM the fast exchange between dissolved Xe@water and Xe@cage is reflected in a large increase in the width of the Xe@water hyperCEST response.

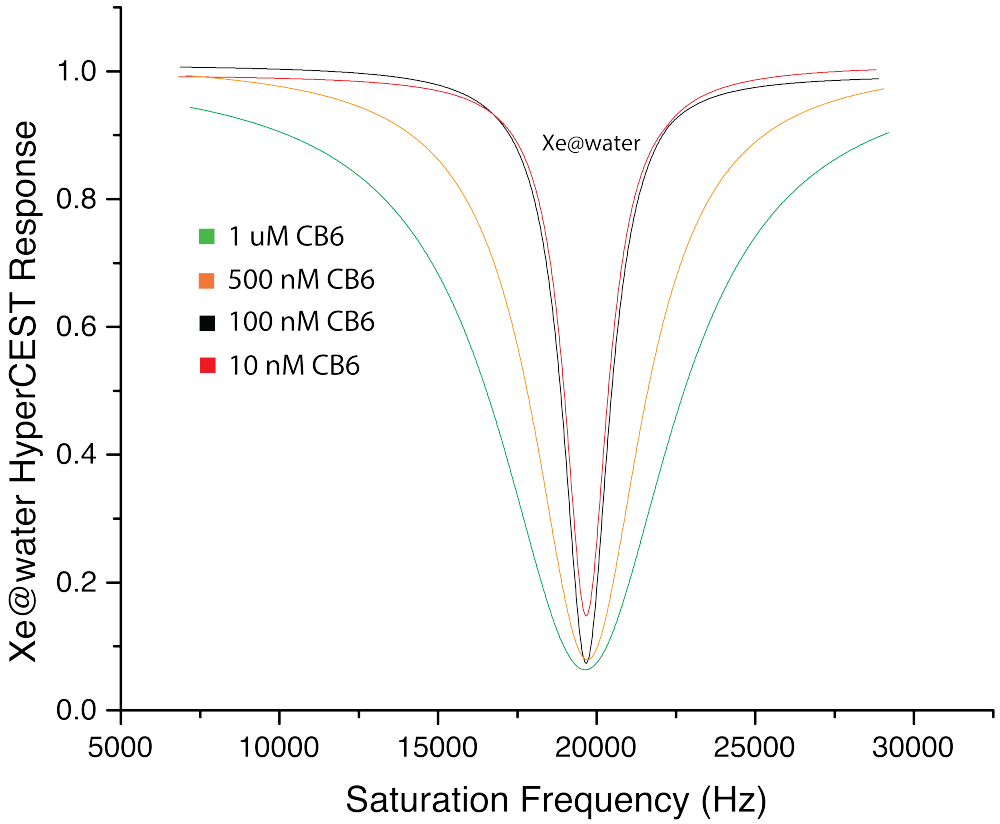

Figure 2.9: The Xe@water peak for four different concentrations of CB6 showing the effects of cage concentration on the bulk xenon peak width; cage concentrations range from 10 nM to 1 μM.

2.5 Conclusions

In the following chapters we will look at different CryA and CBn based chemical sensors, both by direct detection and hyperCEST in hopes to understand what systems are better probed by these different macrocycles and how to take advantage of their unique properties. CryA allows for easy functionalization and has been shown to work for both direct and hyperCEST detection, but it is not commerically available and can be expensive to obtain.

Cucurbiturils are commercially available and they have a fast xenon exchange rate making them excellent for hyperCEST detection, but less optimal for direct detection. They also cannot be easily modified directly and will require the use of secondary molecules such as rotaxanes for targetting.

Chapter 3

Investigation of DOTAMetal Chelation Effects on the Chemical Shift of ^{129}Xe

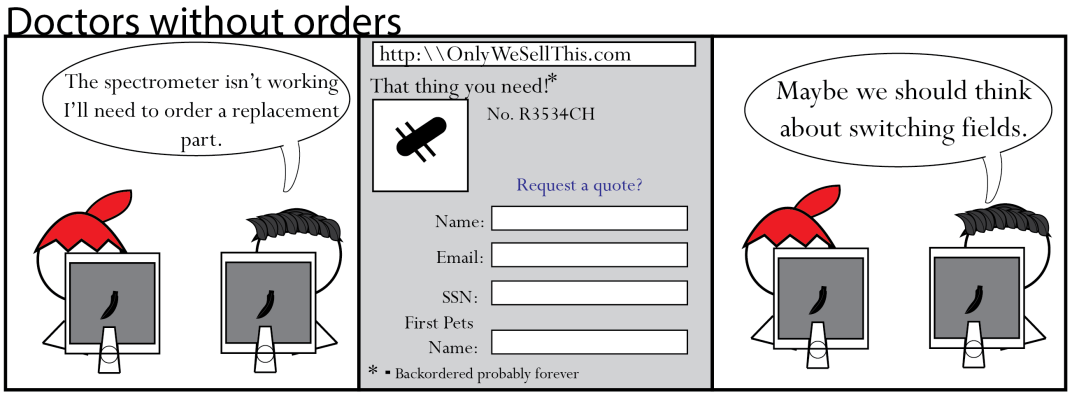

Taking advantage of the functionalizable CryA cage it seemed reasonable to try to induce changes in chemical shift through binding. By adding a metal ion chelating agent localizing a paramganetic center to the CryA cage we may be able to identify the chelated metal by the magnitude of the change in chemical shift. CryA sensors that take advantage of localized ruthenium has already been studied [44], but a sensor that can adequately detect and differentiate between multiple metals was still not developed.

This chapter was previously published in Ref. [28] and is republished here, with minor changes and additional information, with permission.

3.1 Abstract

We investigated the effect of chelating a wide range of metal ions to a cryptophane cage modified with DOTA to observe xenon chemical shifts. This water soluble sensor shows

different chemical shifts when Ca^{2+}, Cu^{2+}, Ce^{3+}, Zn^{2+}, Cd^{2+}, Ni^{2+}, Co^{2+}, and Hg^{2+} were bound. In addition the diastereomers of the cryptophane complex responded differently for the same metal ion indicating a strong dependence on how the sensor folds in solution, and not just the specific identity of the metal. A correlation was observed between coordination number in the DOTA complex and ^{129}Xe chemical shift. By expanding our understanding of how xenon chemical shift responds to metal ion chelation these sensors may be used to detect and quantify important metal ions.

3.2 Introduction

Metal ions can have an enormous impact on biological and environmental systems [45]. Some, including Fe^{3+}, Cu^{2+}, Co^{2+}, Zn^{2+}, and Ni^{2+}, play essential roles in human metabolism, while others, including Hg^{2+}, Cd^{2+}, and Pb^{2+}, are toxic [46]. Although there are well-established methods for the in vitro detection of metals, including atomic absorption spectroscopy and various electrochemical techniques,[4] a practical technique that can simultaneously and nondestructively detect multiple metal ions would be a valuable addition to the existing analytical methods. Conventional NMR spectroscopy can distinguish between different chemical species, but is difficult to apply to complex mixtures. Although many metals have spin-active isotopes that can be detected by NMR spectroscopy, the sensitivity is generally very low. Here, we exploit the strong signals of hyperpolarized xenon, which are associated with a cryptophane cage carrying a metal chelator, to report the presence of metals through binding-induced shifts.

Hyperpolarized ^{129}Xe NMR/MRI has emerged as a promising quantitative in vivo technique that is being explored extensively for the imaging of the lungs by using inspired xenon [47] the study of brown fat and brain tissues by using dissolved xenon.[[48]. Additional work in vitro has established hyperpolarized ^{129}Xe NMR/MRI as a method for the selective, high sensitivie detection of proteins [49] [50] [51], enzyme activities [52], nucleic acids [53], and cell surface receptors [54]. ^{129}Xe is useful as a reporter for a number of reasons: 1) There is no naturally occuring ^{129}Xe in the body, so there are no background signals that must be suppressed. 2) ^{129}Xe displays a large chemical shift in response to its physical and chemical surroundings, making it a sensitive reporter of environment. 3) The ^{129}Xe NMR signal is long-lived. Spin exchange optical pumping of xenon can achieve almost complete polarization of the ^{129}Xe nuclei and allows the detection of low concentrations of ^{129}Xe dissolved in solution [55].

Recent work by Zhang et al. [56] and Kotera et al. [57] developed cryptophane sensors that respond to Zn^{2+} , inducing a change in the chemical shift of the cryptophane-bound ^{129}Xe NMR peak upon metal binding. Changes in the chemical shifts were also observed upon binding Pb^{2+} and Cd^{+} ions. [58] In the current work, we use the chelator 1,4,7,10-tetraazacyclododecane- 1,4,7,10-tetraacetic acid (DOTA), which binds a wide range of metals with very high affinity, coupled to cryptophane-A and a solubilizing Glu5 peptide (M0 ; 3.1). We investigated a larger group of metals compared with previous work, including several that are paramagnetic. A comparison of the shifts induced by the different metals provides insight

into the origin of the shifts, which may facilitate the design of improved multimetal sensors.

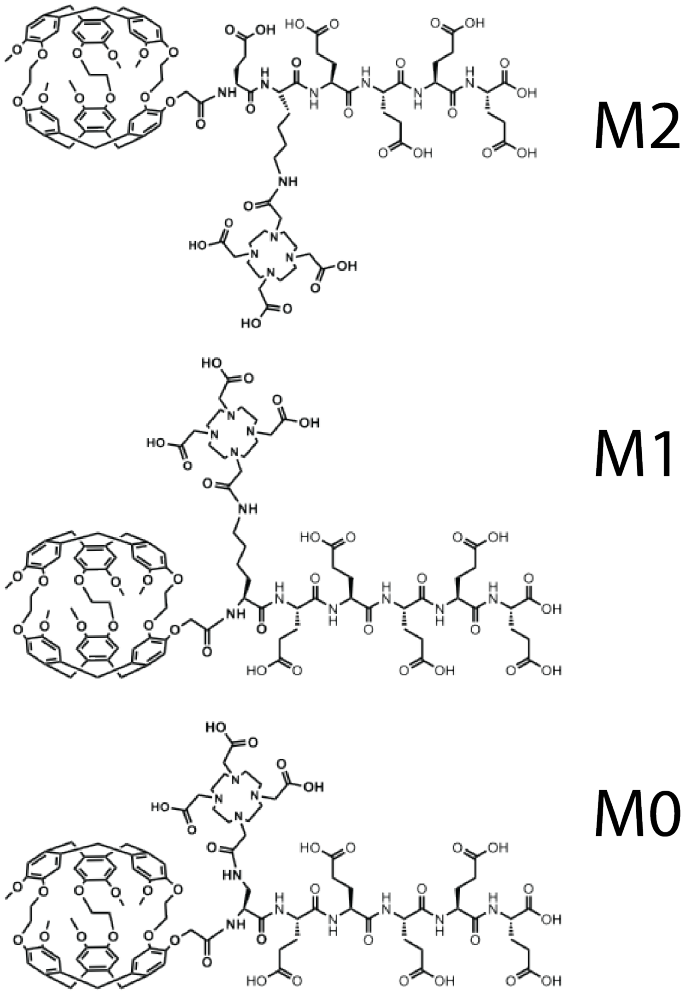

Figure 3.1: Sensor comprised of a cryptophane cage to bind xenon, a DOTA chelator, and solubilizing Glu5 peptide (M0, M1, and M2).

DOTA interacts strongly with transition-metal ions [log Ka = 22.2 (Cu^{2+}), 21.1 (Zn^{2+}), 21.3 (Cd^{2+}), 20.5 (Ni^{2+}), 20.3 (Co^{2+}), 16.4 (Ca^{2+}), 21.6 (Ce^{3+}), 24.4 (Fe^{3+}), and 23 (Hg^{2+}; from cyclam, estimated to have similar affinity with DOTA, due to its similar chemical structure)],[15] and essentially bind any free metals in a sample irreversibly. The affinity of metals for DOTA is stronger than most biological interactions, so, in a biological context, DOTA will act as a sink accumulating metals at a rate determined by their dissociation from the endogenous ligands.

DOTA is a flexible chelation agent with eight possible coordination points: four tertiary amines in the central ring and four carboxylate arms. The geometry of metal-bound DOTA is dependent on the specific metal present and its preferred coordination number (CN). Smaller metals prefer lower CN, for example six for Ga^{2+} 3.2. Larger metals, for example

those in the lanthanide series, favor high CNs using all eight ligand coordination points and incorporating a water molecule to give a CN of nine. The major geometries of interest are octahedral (CN = 6) and square antiprismatic (CN = 8). [59] Metals bound with octahedral geometry (CN=6) have two carboxylic acid arms unattached, which can interact with the cryptophane cage. Hyperpolarized ^{129}Xe in the cryptophane cage is positioned close to the metal ion, and even weak interactions between them can result in a distinct chemical shift, which depends upon the metal present. Cryptophane-A is intrinsically chiral, due to the handedness of the connection between the two cyclotriveratrylene units, and its synthesis yields an equal mix of the two enantiomers. When coupled to amino acids of pure chirality an equimolar mix of two diastereomers is created. For the current work, we used the mixture of the two, which turned out to be advantageous, because the metal-induced xenon shifts are different for each diastereomer.

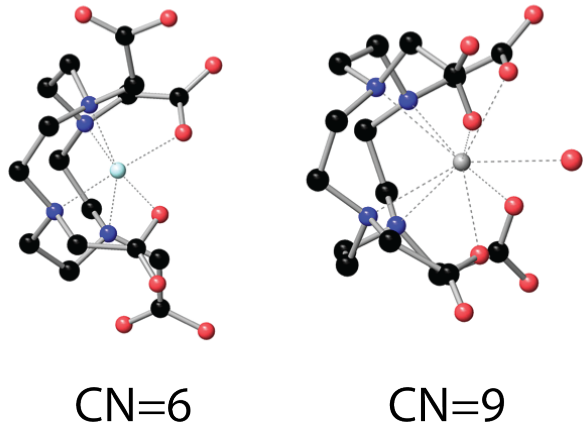

Figure 3.2: 1,4,7,10-tetraazacyclododecane-1,4,7,10-tetraacetic acid (DOTA) chelated in its 6 (left) and 9 (right) coordinate forms.

3.3 Methods

We synthesized a water-soluble sensor with the smallest possible distance between DOTA and the cryptophane cage to increase the effect of metal binding on the xenon chemical shift (M0) then moved the DOTA residue farther away from the cryptophane (M1, M2) as shown in 3.1. The cryptophane cage is hydrophobic, and the solubility of DOTA decreases upon formation of a complex with a metal ion. We added five glutamic acid residues to enhance solubility synthesized using solid-phase synthesis methods with a Wang resin. To minimize the distance between cryptophane and DOTA, we added diaminopropionic acid in the last coupling before addition of the cryptophane and cleavage from the resin. DOTA-NHS ester was used to attach DOTA to the primary amine of aminoproprionate in aqueous solution. The completed sensor was then purifed with reversed-phase high-pressure liquid chromatography (HPLC). The synthesis and structures are summarized in 3.3.

The sensor was dissolved at 50 μM concentration in phosphate buffer (pH 7.4). Upon bubbling a polarized gas mixture containing ^{129}Xe (2% natural isotopic abundance Xe, 10% N_2, 88% He) into solution, the two diastereomers of the structure yielded two distinct peaks similar to previous work [34]. Initial experiments were done combining individual, heavy metal ions with a sensor solution in a 1:1 molar ratio. These were bubbled with polarized xenon, and the ^{129}Xe NMR spectra were measured on a 9.4 T Varian NMR spectrometer [60]. Because the ^{129}Xe chemical shift is sensitive to temperature and pH [61], all spectra were obtained under the same conditions (pH 7.4, 20 ^{o}C 0.1 ^{o}C). Each chemical shift was referenced to the dissolved ^{129}Xe signal [56].

3.4 Results and Discussion

Changes in the chemical shift of xenon were determined upon the binding of the different metal ions, for example Cd^{2+} and Cu^{2+} (3.4). The induced changes in shift for a larger range of metals are shown in graphical format in 3.5. It is interesting to note that the metal-induced shift changes are different for the two diastereomers and distinct for each metal ion. These differences in shift are presumably associated with the way the peptide chain and DOTA moiety interact with the cryptophane cage through transient contacts. All of the ions featured in 3.5 have a 2+ charge. There is no systematic pattern of change with atomic number or a consistent difference between paramagnetic and diamagnetic metals. The direction of the shift was most consistent for the diastereomers for which the free ligand is upfield of the bound ligand. The glutamate that resides in the solubilizing peptide can potentially interact with metals, so we also studied the cryptophanepeptide construct without the DOTA-chelating agent. The cryptophane cage with five glutamic acids attached was mixed with the same metal ions, but no ^{129}Xe NMR shifts were observed, thus supporting our view that the DOTA-bound metals induce the shift in the sensor and not the glutamate residues in the peptide. The distance between the bound metal and the xenon atom is large enough that paramagnetic relaxation does not dominate the xenon linewidth even with strongly relaxing metal ions, such as Ni^{2+}.

The first-row transition metals, Cr, Co, Ni, Cu, and Zn, form hexadentate complexes (CN=6) with DOTA (all have an ionic radius between 0.69 and 0.74 Å). Metals with larger ionic radii, that is, Ca, Cd, and Hg (0.971.1 Å), form octadentate structures (CN=8) with DOTA.[15c] Both diastereomers tend to have more upfield shifts within the CN=8 complexes than the CN= 6 metals. Chemical-shift studies of even larger metals yielded multiple peaks as shown in 3.6 for the sensor bound to Ce^{3+}. Previous ^{1}H NMR studies of lanthanides bound to DOTA revealed a similar phenomenon where a slow exchange between different isomers of a capped square antiprismatic geometry (CN = 9) resulted in multiple peaks.[19] These two isomers represent the two helical structures that the acetate arms of the DOTA complex can take when bound to a metal ion, with an H_2O molecule acting as a cap on the complex. It has been previously shown that xenon detects differences in chirality; [34] here this sensitivity can be exploited to observe the difference between isomeric pairs of metal complexes with the same coordination number. Other lanthanide metals were also tested

3.7 but broadening of the peaks and poor signal make them less ideal for observing this isomerization.

The changes in chemical shift are modest for all metal ions (1 ppm), but they are much larger than the observed line-widths making it possible to identify peaks for multiple metals in a single sample 3.4. Titrations of the sensor, starting with no metal ions and increasing to a 1:1 ratio with Fe^{3+} in increments of one quarter of the total concentration of M0, show resonances for the free and metal-bound forms in slow exchange (as expected from the high affinity of DOTA for all of the metals studied). The relative sizes of the resonances show that the intensities reflect the stoichiometry allowing for their potential use in the quantitative determination of metal-ion concentrations 3.8. At 1:1 we have an equimolar ratio of Fe^{3+} to M0, which appears to correspond to less than 100% bound due to a systematic error in the addition of Fe^{3+} to the sample. The variability of the metal-induced shifts indicates the challenge to optimize xenon-based metal-ion sensors to give maximal shift differences for distinct metals for the analysis of mixtures. Simulations performed by the Jameson group predict that the chemical shifts of a cryptophane-bound xenon atom are a function of the average distance from the methoxy groups on the surface of the cage, and hence, that shifts vary when contact causes a change in the shape of the cryptophane structure [62] [63]. The high polarizability of xenon makes it very sensitive to its immediate environment, thus, very small changes owing to transient contacts can be detected. The binding of metal ions to the attached DOTA moiety causes distinct shifts for each diastereomer, which indicates that different interactions of the peptide/DOTA segment with the cage occur in the two diastereomers. A more complete understanding of the details may allow further optimization of the sensor for maximal response and its utility in metal analysis.

The shifts associtaed with the M1 sensor 3.9 had Co^{2+} with the largest shift response for both diastereomers, while the diamagnetic metals seemed to cause a shift in only a single diastereomer. Cd^{2+}, which showed about a 0.5 ppm shift downfield for both diastereomers for M0, only shifted the right diastereomer peak for the M1 sensor, but to a larger degree (1 ppm). This further confirms that the diastereomers react differently upon metal ion chelation and the magnitude of the effect is at least partially independent of the distance of the chelator in bond lengths from the cryptophane. It is also worth noting that for the M1 construct nearly all the shifts upon binding were upfield, while the M0 shifts were mixed, with more metals causing downfield shifts.

To look for any trends 3 metals (Zn^{2+}, Ni^{2+}, and Cu^{2+}) with a coordination number of 6 were also looked at in M2 and compared to M0 and M1 as seen in 3.10. For these 3 metals M0 exhibited the largest shifts while M2 exhibited barely any shift upon metal-ion chelation. The two diastereomers continue to be affected differently by chelation even for M2 where the DOTA is 13 bonds away from the cryptophane cage.

The signal-to-noise ratio in these experiments depends on the degree of polarization of the xenon and the fraction of ^{129}Xe in the gas. Increasing either of these would improve our ability to resolve the chemical-shift differences. Our experiments were performed with approximately 2% polarization of the natural isotope distribution of 26% ^{129}Xe. Using isotopically-enriched xenon and increasing the polarization would greatly increase the ob-

served signal-to-noise ratio. Continuous-flow polarizers generating 60 % polarization have been described, [64] and near-unity polarization has been achieved in batch processing polarizers. [65] In addition, the use of chemical exchange saturation transfer (CEST) [30] would provide further significant enhancement of the sensitivity. To maintain the resolution, optimization of the saturation power to avoid power broadening will be needed. Applying these approaches should make it possible to detect metal complexes in the low nanomolar concentration range. The ability to detect metals at low concentrations in the presence of more abundant ones will be determined by the separation between the xenon resonances of the particular species of interest. It has been shown that hyperpolarized xenon can be combined with MRI, and this combination makes it possible to image the spatial distribution of metals in a sample [66].

3.5 Conclusions

The modest shift observed for M0, M1, and M2 upon metal-ion chelation indicate the overall structure of this cryptophane sensor may not be optimal for metal-ion detection. While it is clear that the identity of the bound metal has a unique affect on the chemical shift, the resulting shifts are not strong enough to make the metals identifiable. Further work looking at the 3-dimensional folding of the molecule in both its diastereomeric forms before and after metal-ion binding may help us to understand these results. Although the chemical shift might not be ideal for applying these cryptophane sensors, paramagnetic metals, specifically gadalinium can be used as a relaxation agent in ^{1}H MRI and a change in relaxation could be observed for ^{129}Xe after chelation. In the next chapter we will explore using cryptophane sensors modified with DOTA as relaxation based detectors.

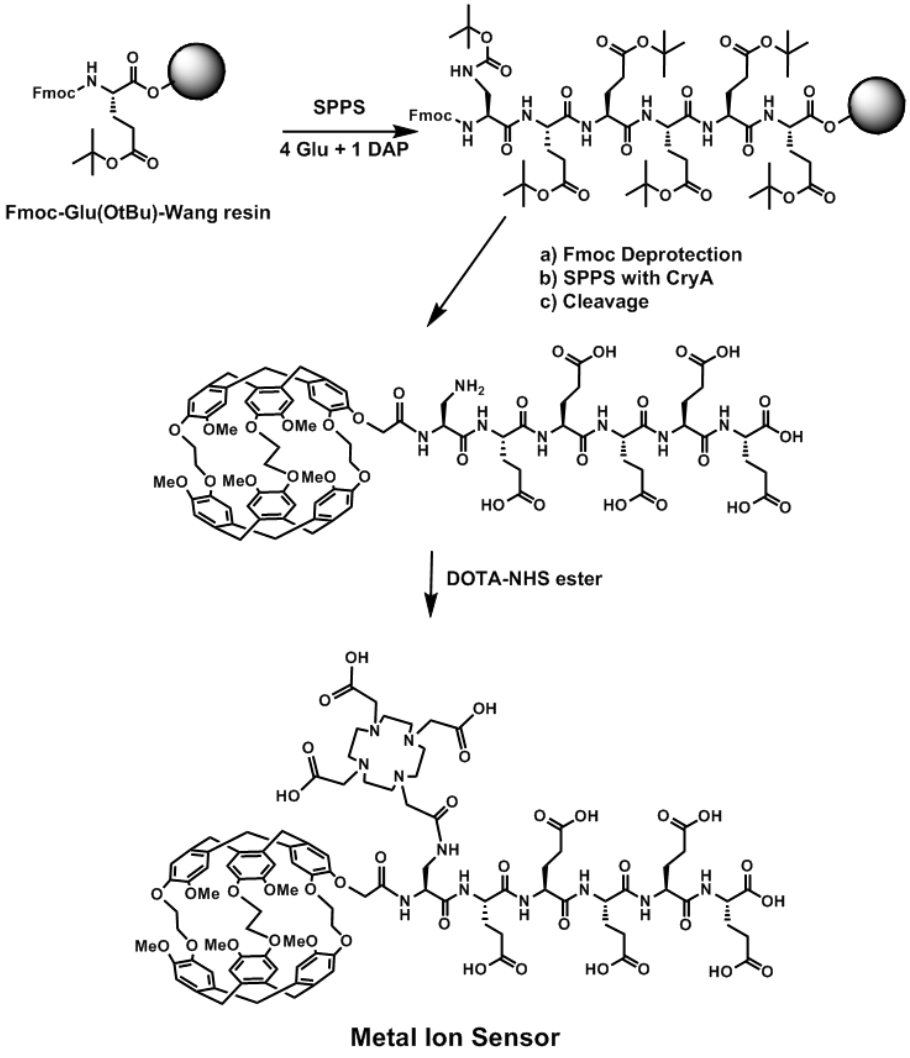

Figure 3.3: Synthesis of the M0 metal ion sensor. Five glutamic acid molecules, one diaminopropionic acid, and a cryptophane cage were attached to Wang resin. They were then cleaved from the resin and DOTA was attached in aqueous solution

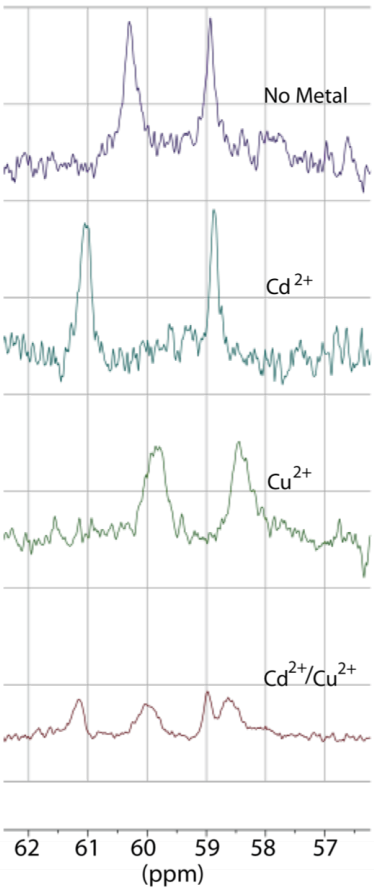

Figure 3.4: Chemical shifts for 50 μM samples of M0 complexed with: no metal, Cd^{2+}, Cu^{2+}, and a 50/50 mix of Cd^{2+} and Cu^{2+}.

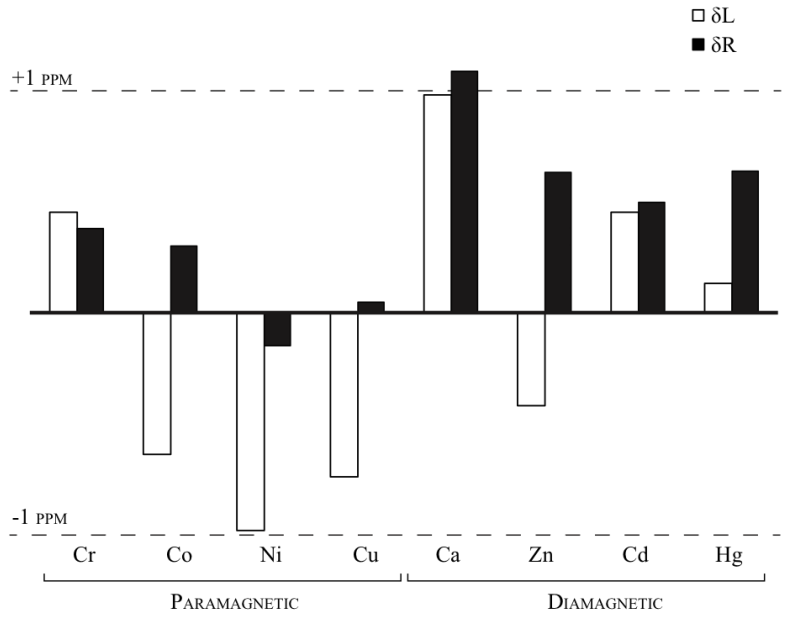

Figure 3.5: Comparison of shifts for individual diastereomers with both paramagnetic and diamagnetic metals chelated compared to the shift of a sensor with no metal. Metals are arranged from smallest to largest mass within each subset.

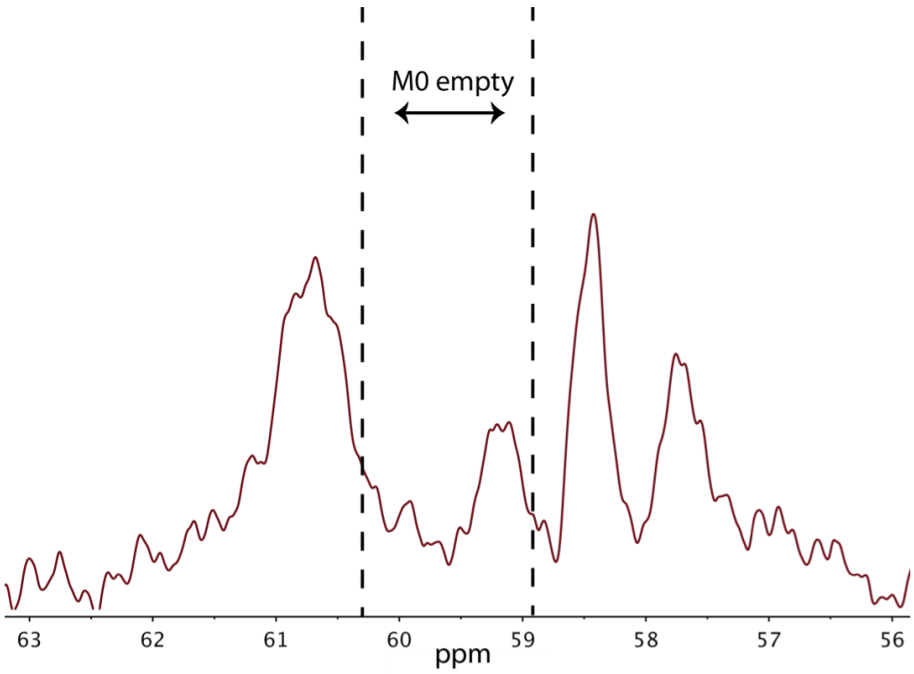

Figure 3.6: The ^{129}Xe spectrum of the cerium-bound sensor (CN = 9) shows four peaks versus two for the other metals, due to the two helical structures that the DOTA acetate arms form around the lanthanides. These two isomers are in slow exchange with each other giving rise to distinct peaks that are observable by using the sensor.

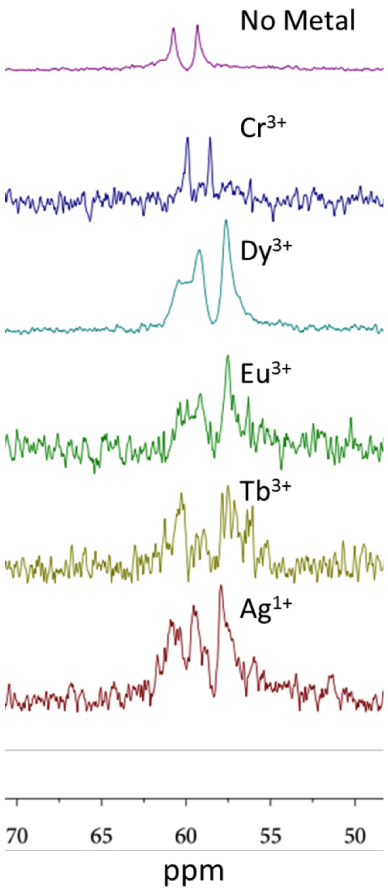

Figure 3.7: The ^{129}Xe spectrum of several lanthide-bound sensors (CN=9) compared to M0 empty and M0 bound to Cr^{3+} (CN=6) show broad multiplets caused by the presence of DOTA isomers

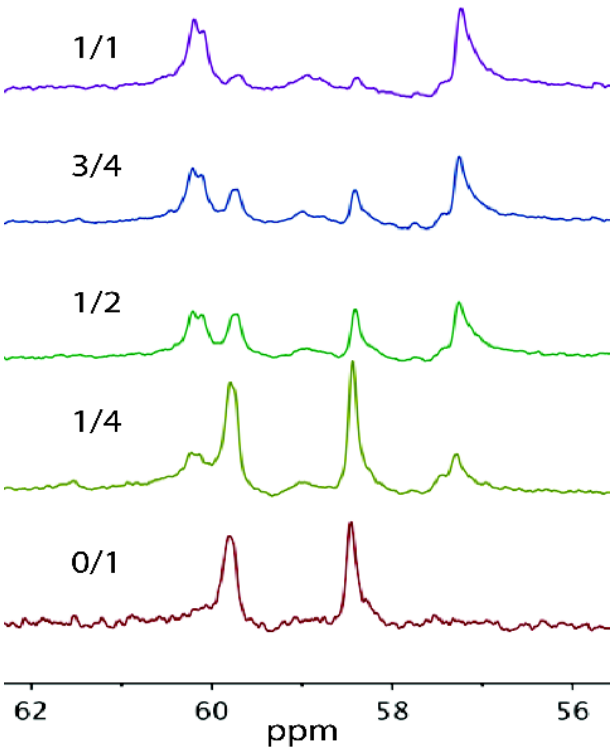

Figure 3.8: A series of spectra for the titration of Fe^{3+} into the sensor solution shows the simultaneous detection of the metal-bound and unbound sensor. The estimated ion-to-sensor ratio is shown alongside each spectrum, with 1/1 corresponding to approximately 95% bound.

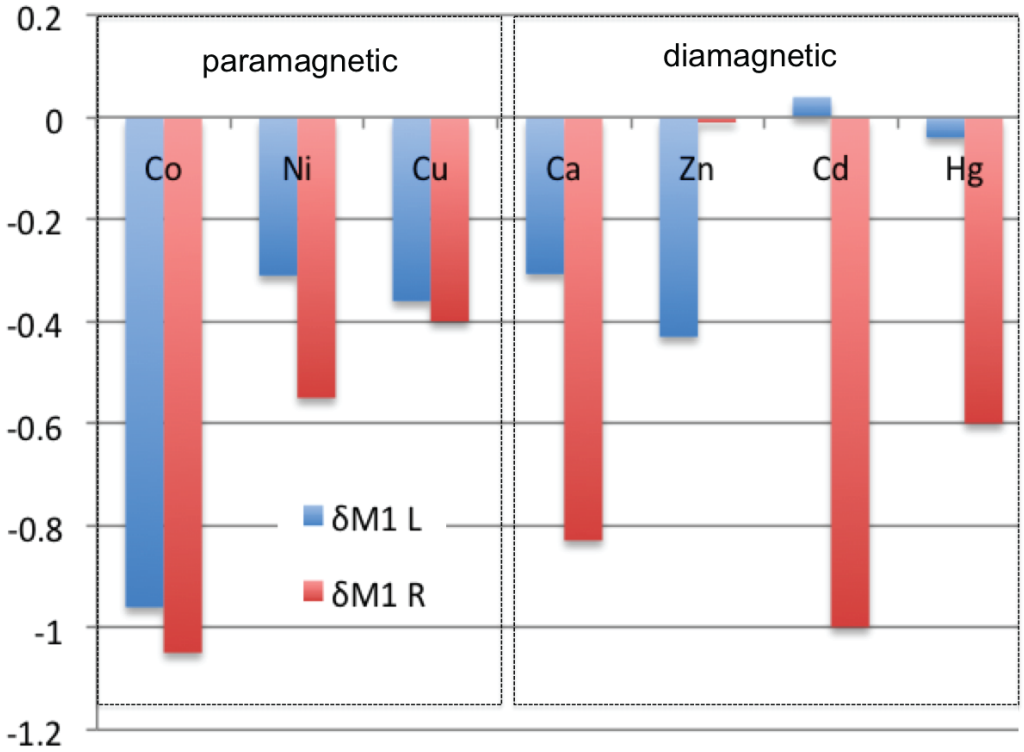

Figure 3.9: Comparison of M1 shifts for individual diastereomers with both paramagnetic and diamagnetic metals chelated compared to the shift of M1 with no metal. Metals are sorted into paramagnetic and diamagnetic.

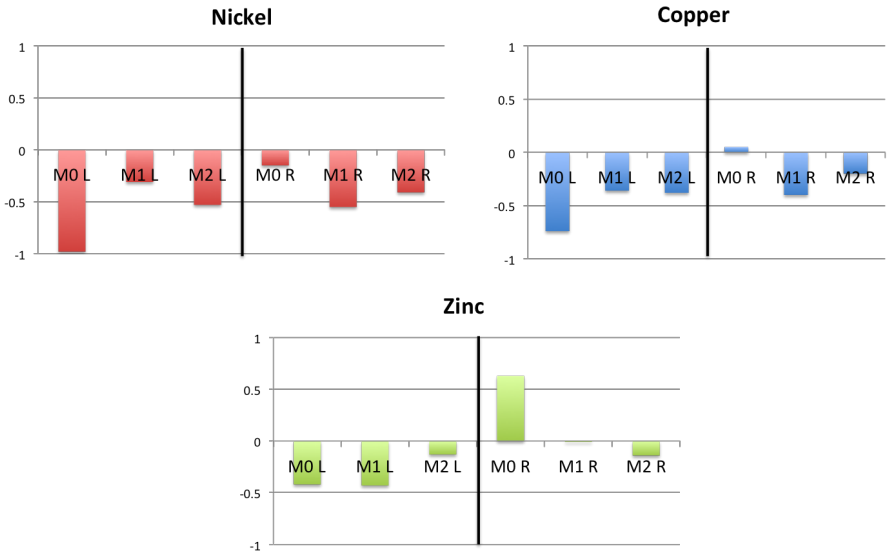

Figure 3.10: Zn^{2+}, Ni^{2+}, and Cu^{2+} chelated to M0, M1, and M2 comparing shifts of the different diastereomers

Chapter 4

^{129}Xe NMR Relaxation-Based Macromolecular Sensing

This chapter was previously published in Ref. [67] and is republished here, with minor changes and additional information, with permission.

4.1 Abstract

We report a ^{129}Xe NMR relaxation-based sensing approach that exploits changes in the bulk xenon relaxation rate induced by slowed tumbling of a cryptophane-based sensor upon target binding. The amplification afforded by detection of the bulk dissolved xenon, present at orders of magnitude greater concentration than the sensor, allows sensitive detection of targets. The sensor is comprised of a xenon-binding cryptophane cage, a target interaction element, and a metal chelating agent. Xenon associated with the target-bound cryptophane cage is rapidly relaxed (broadened and depolarized) and then detected after exchange with the bulk. Here we show that for macromolecular targets, such as avidin, slowing the rotational correlation time of the sensor has a substantial impact on the relaxation of the xenon. Paramagnetic centers were introduced to enhance relaxation but these are not necessary to

generate significant changes in relaxation. Upon binding of a biotin-containing sensor to avidin at 1.5 μM concentration, the free xenon T_2 is reduced by a factor of 4.

4.2 Introduction

Very strong NMR signals from hyperpolarized ^{129}Xe, generated by spin exchange optical pumping (SEOP) [17], enabled its use in applications such as lung imaging and probing porous materials. The solubility of xenon in water is sufficient to make measurement of dissolved hyperpolarized ^{129}Xe signals easy, and the sensitivity of xenons chemical shift to the local environment reports on interactions in the solution. Most interactions with xenon are weak and exchange among interaction sites is fast, so the shift reflects a population average over interacting sites. To enable sensing of a specific target we developed molecular sensors that combine a xenon binding cage, cryptophane-A [68] [69] [70] [71], with a target-binding element [72] [73] [74] [58]. The exchange of xenon in and out of the cryptophane cage is slow on the chemical shift time-scale, giving a highly-shifted, separate resonance for cryptophane-associated xenon.

Binding of the targeting element of the sensor to the target causes a small further shift of the encapsulated xenon, reporting on the interaction and, hence, the presence of the target. Although xenon exchange is slow enough to give a separate resonance, it is sufficiently fast that chemical exchange saturation transfer (CEST) effects can be large. We showed that hyperpolarized xenon CEST [30] (hyper-CEST) can be used for highly sensitive detection of targets into the pM concentration range [75] and can be used as contrast agents for xenon MRI to visualize the distribution of the target molecule in optically-opaque samples. Sensors for specific ions, proteins, and nucleic acids have been developed [39] [76] [53], and variants of cryptophane-A (binding constant 850 M^{-1}) and other compounds have been identified with even better exchange properties [75].

The hyper-CEST detection method requires selective saturation of the cage-associated xenon peak, which means that it must be resolved from the bulk xenon peak. Even at moderately high fields, resolving the peaks is not a problem, because the cryptophane-associated shift is about 120 ppm from the bulk dissolved xenon. Discriminating free and target-bound sensor is more challenging, because binding-induced shifts are a few parts per million [77]. Since the magnetization from hyperpolarization is independent of field we wanted to explore whether alternative sensors could be developed that would remove the hyper-CEST requirement. To this end, we prepared a new sensor for studies of binding induced xenon relaxation, M2B1 (4.1) that combines cryptophane for binding xenon, a targeting element, and a DOTA chelator to allow introduction of paramagnetic metals.

NMR relaxation rates are sensitive to the magnitude of magnetic interactions of the spins studied (e.g. dipole moments of other spins nearby and chemical shift anisotropy), and also their time dependence, arising from molecular tumbling in solution. In the context of this work, we exploit the difference in tumbling correlation time between a free sensor and one that is bound to a high molecular weight target [50] [78] [79] [80]. Relaxed xenon in the cage is exchanged into solution at a rate much higher than the relaxation rate of bulk xenon

and, hence, affects the bulk xenon relaxation as well. Detection of the target is achieved by determining the change in relaxation rates of the bulk xenon upon interaction of the sensor with the target, a form of relaxometry.

Here we show that there are significant differences in the relaxation rate for xenon in solution with the sensor alone and xenon in solution with the sensor bound to a macromolecular target, avidin. The changes are sufficiently large to allow use of relaxation rates to detect the association of the sensor with the target, and hence the presence of the target in the sample. We have used detection of avidin as a model system, but this sensing principle can be extended to a wide variety of possible targets. The only requirement is that the target issufficiently larger than the sensor (2 kDa) to substantially alter the rotational correlation time.

4.3 Methods

Mono-acid cryptophane-A cage was covalently attached to the N-terminus of a seven amino acid peptide chain (KKEEEEE) that was further derivatized with 1, 4, 7, 10-tetraaza-cyclododecane-1, 4, 7, 10-tetraacetic acid, DOTA, and biotin through the lysine amino groups (4.1). For binding studies with avidin, which is a tetramer with four biotin sites, the sensor was added to avidin in a 4:1 ratio. DOTA forms very stable complexes with most metals; in this work both metal-free and Gd^{3+}-bound forms were studied.

For all experiments, the sensors and controls were dissolved in 10 mM PBS (pH 7). Each sample was pressurized to 50 psi with a mixture of 2% natural isotopic abundance xenon gas, 10% nitrogen and 88% helium gas mixture (natural abundance of ^{129}Xe is 26%). ^{129}Xe in this mixture was hyperpolarized using a homebuilt SEOP xenon polarizer and then bubbled into the sample at a flow rate of 0.4 standard L/min. Bubbling was stopped before acquisition to allow bubbles to dissipate, so that the sample was homogenous. T_2 relaxation times of the bulk xenon resonance were measured with a standard CPMG pulse sequence. T_1 relaxation times of the bulk xenon resonance were measured by means of a single-shot decay signal using a Look-Locker pulse sequence [81]. This sequence minimizes the shot noise of each measurement and reduces the measurement time. Xenon T_1 and T_2 relaxation time constants for samples containing just the buffer were also measured as controls. Relaxation times for a solution containing stoichiometric amounts of sensor added to avidin were also measured. All data were collected on a 9.4 T Varian Inova NMR spectrometer at 293 K.

4.4 Results and Discussion

The relaxation of xenon in water is known to be very slow, because fluctuations of the water around xenon are very rapid, consistent with the values we observed (4.1). The addition of M2B1 to the solution decreases the T_2. The broadening of bulk xenon due to exchange in and out of the cage is quite small (less than 1% of xenon is bound, and the exchange rate is $20\ s^{-1}$), consistent with a modest decrease in relaxation time [34]. The

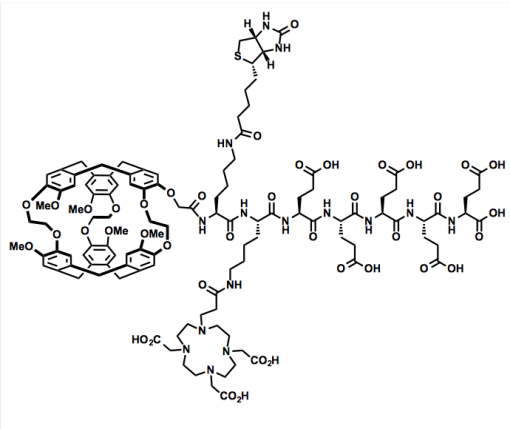

Figure 4.1: The relaxation sensor, M2B1, consists of a cryptophane cage modified with a DOTA for metal ion chelation, a biotin for avidin binding, and glutamate residues for solubilization. The designation, M2B1, refers to the placement of the metal-binding moiety at position 2 and biotin at position 1 of the peptide chain.

addition of avidin alone to the xenon solution causes exchange broadening, but the process is near the fast exchange limit reflecting transient binding of the xenon. Similar weak binding and broadening of xenon has been seen for many proteins [82]. Adding biotin to a solution of avidin increased the T_2 of xenon, because the biotin-binding pockets of the protein are no longer open to xenon. When M2B1 and avidin are both added to the solution, the biotin on the sensor binds to avidin, and the cryptophane cage is substantially immobilized. The sensor also interacts nonspecifically with the avidin that decrease the bulk T_2 of xenon.

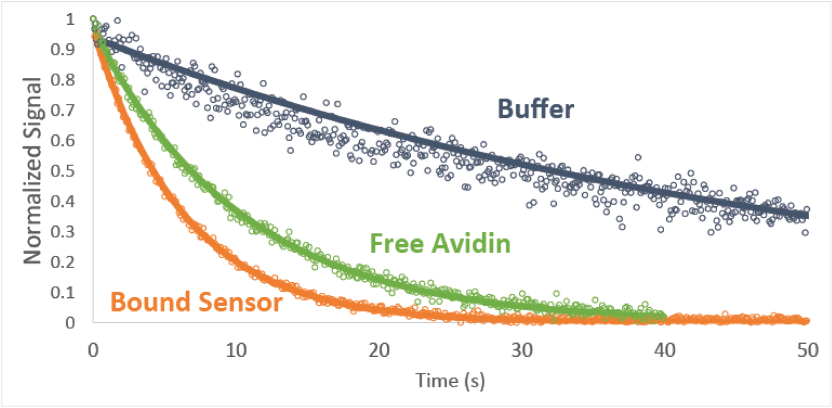

Figure 4.2: Plot of T_2 relaxation curves of xenon in buffer, xenon with avidin, and xenon with sensor bound to avidin showing dramatic enhancement of relaxation in the complex. All curves are shown fitted to single exponential decay.

To calculate the effects of bound state ^{129}Xe T_2 relaxation on the bulk ^{129}Xe, it is necessary to use the Carver Richards equation in its corrected form [83] that treats the second-

order exchange process and the effects of the Carr Purcell sequence. This host-guest system is unique in that free Xe and Xe@cage have significantly different chemical shifts and intrinsic relaxation rates. Using 2.7 we showed that cryptophanes in an excess of dissolved Xe have an occupancy of 88.6%, as more then half the sensors are occupied this system behaves in a pseudo first-order manner, with the xenon population incorporated into one of the rate constants using the notation of [83] given by,

$$k_{ge} = p_g k_{ex} \tag{4.1}$$

$$k_{eg} = p_e k_{ex} \tag{4.2}$$

$$[cage][Xe]_w k_{ge} = R_{ge} \tag{4.3}$$

$$[Xe@cage]k_{eg} = R_{eg} \tag{4.4}$$

As the $[Xe]_w$ concentration is effectively constant we introduce a new rate constant k_{ge} dependent only on the cage concentration,

$$\bar{h}_{ge} \equiv [Xe]_w k_{ge} \tag{4.5}$$

$$[cage]\bar{h}_{ge} = R_{ge} \tag{4.6}$$

The popualtions of the ground (p_g) and excited (p_e) in the above equation refer to the fraction of unbound and bound sensors respectively. If more than half of the population is in the excited (bound) state then the Carver Richards equation predicts that the T_2 of the bound site will affect the bulk relaxation rate. This is an exchange transferred T_2 effect, which is different from the exchange broadening effect.

$$p_g = \frac{[cage]}{[cage] + [Xe@cage]} \tag{4.7}$$

$$p_e = \frac{[Xe@cage]}{[cage] + [Xe@cage]} \tag{4.8}$$

When p_g is smaller than p_e, the bound T_2 affects the bulk T_2. The exchanged transferred T_2 relaxation can contribute significantly to the bulk xenon relaxation when the occupancy of the cage is significant and the cage bound T_2 relaxation is fast. The slowed tumbling of the cryptophane cage when bound to avidin results in faster relaxation of xenon in the cage giving a roughly four-fold reduction in the bulk xenon T2, shown in 4.1. The change in T_2 is apparent in the relaxation curves in 4.2. The enhancement of relaxation upon association of the sensor with the target protein is the key element of this sensing approach. The lowest concentration of avidin measured using this sensor is 130 nM. Other targets would have

different detection limits depending on the targets size and the nonspecific interactions of xenon and the sensor with the background.

Improved xenon polarization or an isotopically-enriched gas mixture would improve the signal-to-noise ratio and further improve the sensitivity of this technique. Higher molecular weight targets will give higher bound ^{129}Xe relaxation rates (proportional to the tumbling correlation time, roughly linear in molecular weight [84]) and, thus, also improve sensitivity.

It is worth noting that the slowed tumbling of the sensor also causes a reduction in the T_1 value of xenon (reflecting increased spectral density at the Larmor frequency), but this effect is smaller than that on T_2, which depends primarily on the spectral density at zero frequency.

In the design of M2B1 we included a tethered DOTA to bind a paramagnetic metal and potentially enhance the relaxation. Gd^{+3} is a very effective relaxation agent with seven unpaired electron and it binds very tightly to DOTA. M2B1 with Gd^{+3} bound was more efficient in both T_2 (2.4-fold higher relaxivity) and T_1 (1.05 fold higher relaxivity) relaxation than without the metal bound. The cryptophane cage and the DOTA itself sur-rounding the metal limit the closest approach of the xenon to the metal, so the effects on relaxation are much less pronounced than for water, which can bind the metal directly in conventional contrast agents.

When the metal-chelated M2B1 is bound to the avidin, there is no improvement in xenon relaxivity relative to metal-free M2B1. It seems likely that, upon binding, interactions of the sensor with the protein affect the distance between the metal ion and the caged xenon. Since the relaxation depends on the inverse sixth power of the distance even a modest increase in average distance could eliminate the enhancement seen in the metal-free sensor.

Sample	T_2(s)
1x PBS buffer	56.4 ± 0.6
5 μM M2B1	28.3 ± 0.4
1.5 μM avidin	11.2 ± 0.2
5 μM M2B1 with Gd^{3+}	11.2 ± 0.2
5 μM M2B1 with Gd^{3+} and avidin	4.01 ± 0.03
Biotin saturated 1.5 μM avidin	17.6 ± 0.2
5 μM M2B1 added to 1.5 μM biotin saturated avidin	7.32 ± 0.08
5 μM M2B1 with 1.5 μM avidin	6.40 ± 0.03
5 μM M2B1 with 130 nM avidin	26.9 ± 0.6

Table 4.1: Relaxation Times of Xenon in Biotin-Avidin Solutions with M2B1

A 1.5 μM solution of avidin (4.3 A) has a relaxation time of 11 s. Adding biotin to the avidin solution increased the relaxation time to 17.6 s (4.3 B) suggesting that the biotin-binding pocket also binds and relaxes xenon. The sensor in a 5 μM concentration yields a 28 s relaxation time. Mixing the sensor with avidin (4.3 C) reduces the xenon relaxation time to 6.4 s. The effectiveness of the sensor, however, also depends on nonspecific binding of the

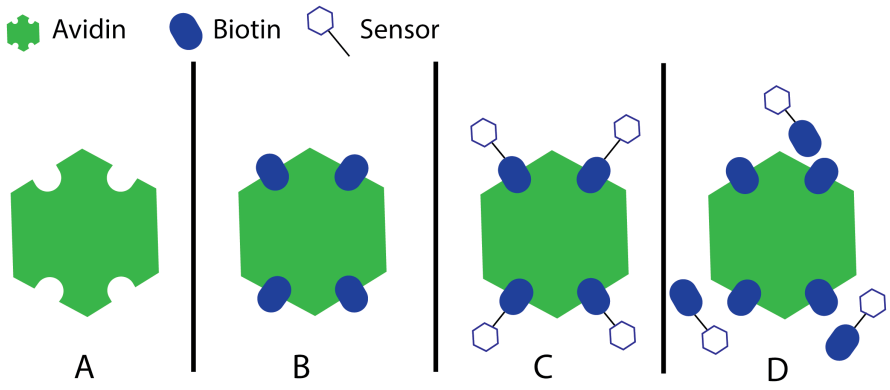

Figure 4.3: Tested relaxation environments for specific and nonspecific binding interactions with avidin, A corresponds to nonspecific binding of xenon gas to avidin with nothing bound to it; B is the relaxation of xenon with biotin-bound avidin; C is the sensor bound to avidin with the assumption that by adding stoichiometric amounts there is minimal nonspecific binding; D is nonspecific binding of the sensor to avidin bound to biotin.

sensor to avidin, made possible by the hydrophilic peptide that solubilizes the cryptophane. The premixed biotin-avidin solution (4.3 D) can no longer specifically bind the sensor, so adding it to the solution would, in the absence of any interaction, result in a relaxation time of 10.9 s calculated as the sum of relaxation rates of a solution containing only the sensor and a solution containing only avidin already bound to biotin. The measured relaxation time, however, was lower (7.3 s) confirming that there is a nonspecific sensor-avidin interaction. The sensor specifically bound to avidin relaxes at a rate approximately 40% faster, but strategies to reduce the nonspecific sensor-protein interaction would increase the overall contrast upon specific binding.

Due to the small amount of sensor necessary to observe relaxation contrast, shortening the solubilizing linker could significantly reduce nonspecific interactions while not reducing solubility to the point where it would no longer be effective. The solubility of the sensor is around 300 μM, so it should be possible to shorten its peptide chain while keeping it soluble at 5 μM. It is possible to imagine generating a solubilizing linker that acts as your targeting moiety for many systems or designing sensors that take advantage of the nonspecific binding.

Xenon NMR for sensing has exploited binding-induced shifts and saturation transfer for contrast generation, which both require resolution of chemically-shifted peaks. Here we demonstrate that a sensor with a xenon-binding cage can act as a relaxation agent that responds to altered correlation times upon binding a macromolecular target. Even with a moderately-sized protein target (avidin, 70 kDa) there is a dramatic enhancement of T_2 relaxation of the caged xenon, which is transferred to bulk dissolved xenon through exchange. This effect does not require chemical shift resolution. The relaxation effects will be increased for larger target molecules or complexes, because T_2 relaxation scales with molecular weight. This paper also shows that nonspecific interactions are strong enough to change the bulk

xenon T2, so studies for other targets should design the peptide for maximum specificity.

4.5 Conclusions

The potential for taking advantage of nonspecific interactions, as well as the persistence of relaxation based techniques at low field makes this a promising application of cryptophane based xenon sensors. Optimization of the sensors to interact with different types of protein surfaces could work as a blunt indicator, while looking at different binding moieties and targets may still yeild useful applications. The low concentrations necessary to do relaxation experiments is also a significant benefit over chemical shift based sensors, especially considering these senors tend to have low solubility unless modified with long solubilizing tails. Shortening the solubilizing tail would reduce the overall solubility of the constructs, but may also reduce the nonspecific binding of the sensor to the surface of proteins making the bound sensors relaxation contribution more pronounced.

Chapter 5

Rotaxane-mediated suppression and activation of cucurbit[6]uril for molecular detection by ^{129}Xe hyperCEST NMR.

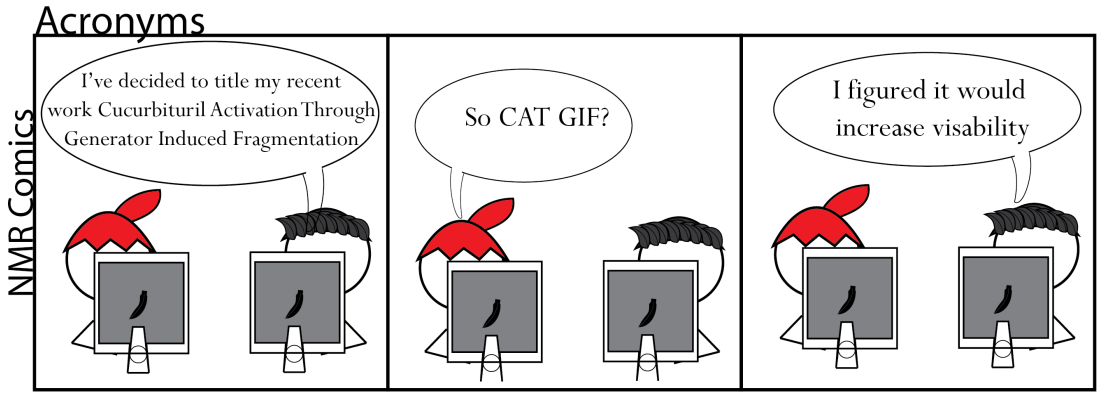

Previously we studied the use of cryptophane based sensors and saw that while the chemical shift change upon binding was not significant enough for sensitive detection, relaxation based approaches using CryA appear to be very promising. Now I'd like to pivot and look at a relatively different system using cucurbiturils as the source of hyperCEST contrast, which have been functionalized with a rotaxane.

This chapter was previously published in Ref. [29] and is republished here, with minor changes and additional information, with permission.

5.1 Abstract

We report a method for blocking interactions between ^{129}Xe and cucurbit[6]uril (CB6) until activation by a specific chemical event. We synthesized a CB6-rotaxane that completely blocked ^{129}Xe@CB6 interactions until cleaved, at which point CB6 was released and produced a ^{129}Xe@CB6 NMR signal. This activated ^{129}Xe NMR platform allows for modular synthesis and can be expanded to applications in detection and disease imaging.

5.2 Introduction

Localized molecular detection with high sensitivity and selectivity is of paramount importance in early disease detection. Current techniques such as magnetic resonance imaging (MRI), the clinical analogue to nuclear magnetic resonance (NMR), and x-ray computed tomography benefit from being noninvasive techniques with high resolution and excellent tissue penetration [85] [86] [87]. However, these techniques lack molecular information that could provide valuable insight during disease diagnosis. While advances in responsive ^{1}H NMR contrast agents that turn on only in select environments have led to the detection of enzymes [86], signaling molecules [88] [89], and redox conditions [90], none of these advances offer direct molecular detection with high signal contrast. Xenon MRI is poised to be a highly sensitive alternative to 1H MRI. The use of hyperpolarized ^{129}Xe can increase signal strengths by several orders of magnitude, and this approach exhibits non-existent background signals in most chemical and biological environments [91] [23]. Further, xenon can participate in a range of supramolecular interactions, producing distinct molecular signals for different xenon hosts. This enables xenon NMR to be used for molecular imaging applications [35] [50]. When coupled with chemical exchange saturation transfer (CEST) techniques between xenon and its host molecules, ^{129}Xe hyperCEST NMR provides highly sensitive molecular detection at levels that are required for the early detection of disease biomarkers [30].

Taking advantage of this sensitivity, hyperCEST has been used to detect cancer markers [92] [60] [93] [52] [70], small molecule analytes [77], and cell surface glycans [94]. These methods rely on either targeted delivery of xenon hosts to a region of interest, or small chemical shift differences between bound and unbound xenon sensors. It would therefore be desirable to suppress the ^{129}Xe@host signal completely until the sensor reaches a region of interest and can be selectively activated. Further, all of these previous examples have been limited by a reliance on cryptophane-A (CryA) xenon hosts that are hydrophobic, costly, and difficult to functionalize.

Cucurbit[6]uril (CB6) is an ideal xenon host for activated ^{129}Xe NMR detection, as it produces a unique ^{129}Xe@CB6 signal, has improved exchange parameters for hyperCEST when compared to CryA, is soluble in most buffers and biological environments, and is commercially available [75] [39]. While CB6 has only recently been reported for use with ^{129}Xe hyperCEST NMR [75], it is attracting significant attention over CryA-based sensors due to these advantages. However, one limitation of CB6 sensors is the difficult chemical

functionalization to generalize them for diverse spectroscopic applications [95].

While the covalent functionalization of CB6 remains a challenge, the ability to participate in a wide range of supramolecular host-guest interactions has been well studied [96] [97]. Competing CB6 guests have been shown to suppress ^{129}Xe@CB6 signals to varying degrees, although in each case an excess of competing molecules was used to suppress the ^{129}Xe@CB6 signal [75] [98]. Recently, Schroder et al. took advantage of CB6 host-guest interactions to design an enzyme-sensing platform based on a competition between ^{129}Xe and an enzyme product for binding of the CB6 cavity [98]. However, it would be beneficial to have a more modular ^{129}Xe sensor platform that does not rely on a specific molecules affinity toward cucurbituril. It would likewise be valuable to create a system that will block ^{129}Xe@CB6 interactions with greater control, as this approach could eliminate background signals until the CB6 reaches a region of interest, where it can be released and produce a ^{129}Xe@CB6 signal.

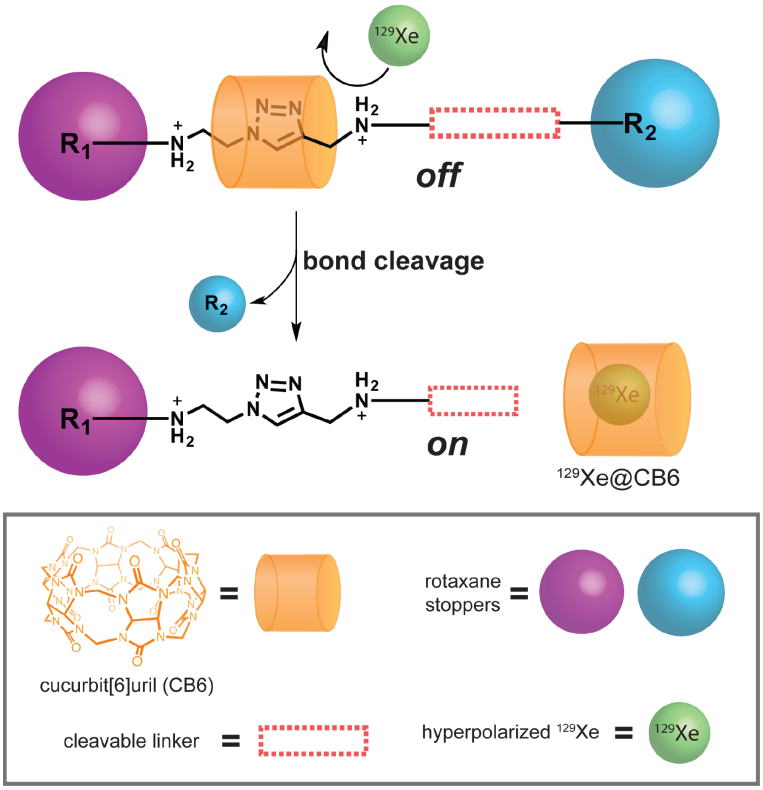

Figure 5.1: General strategy for activating CB6-rotaxanes for ^{129}Xe NMR. A rotaxane with a triazole-diammonium-CB6 center and a cleavable linker blocks ^{129}Xe@CB6 interactions and thus suppresses ^{129}Xe@CB6 NMR signals. Once cleaved, the CB6 ring can dissociate and serve as a host for hyperpolarized ^{129}Xe, producing a ^{129}Xe@CB6 NMR signal.

Herein, we report the design, synthesis, and implementation of a chemically activated CB6-rotaxane platform for ^{129}Xe NMR 5.1. In the proposed system, the Xe@CB6 inter-

actions are blocked by a mechanical bond, where the dumbbell stopper components of a rotaxane prevent ^{129}Xe from accessing the CB6 cavity. Upon cleavage of one of the rotaxane stoppers, the dissociation of the CB6 ring allows it to host ^{129}Xe, producing a ^{129}Xe@CB6 signal at levels far above background. While we focused on CB6 for this report, this system could be diversified using different synthetic strategies to afford rotaxanes with other moieties for tunable xenon exchange rates or competitive thermodynamics.

5.3 Methods

All solvents and reagents, including 1-pyrenecarboxaldehyde, cucurbit[6]uril hydrate, and β-cyclodextrin hydrate, were purchased from commercial suppliers and used without further purification. 2-azidoethylamine,5.2 and 1⊂CB6S2 were prepared according to literature procedures. Thin layer chromatography (TLC) was performed on silica gel 60 F254 (E. Merck) and visualized under a UV lamp at 254 nm. Column chromatography was carried out on silica gel 60 (E. Merck, 230400 mesh). A C-18 column was used for analytical and semi-preparative reverse phase high performance liquid chromatography (RP-HPLC) on an Agilent 1100 Series Capillary LC. Runs were eluted with H_2O/MeCN (0.1 % v/v TFA) and monitored using a UV-Vis detector. Nuclear magnetic resonance (NMR) spectra were recorded on Bruker Avance 400 and 600 spectrometers with working frequencies of 400 or 600 MHz for ^{1}H NMR, and 100 or 150 MHz for ^{13}C NMR, respectively. Data for ^{1}H NMR spectra are reported as follows: chemical shift (ppm), multiplicity, coupling constant (Hz), and integration. Data for ^{13}C NMR are reported in terms of chemical shift. Chemical shifts are referenced to the residual non-deuterated solvents for 1H (CDCl3: = 7.27 ppm, CD_3CN: = 1.94 ppm, $(CD_3)_2SO$: = 2.50 ppm) and 13C (CDCl3: = 77.0 ppm, CD_3CN: = 118.26 ppm, $(CD_3)_2SO$: = 39.52 ppm) nuclei. Matrix assisted laser desorption-ionization time-of-flight mass spectrometry (MALDI-TOF MS) was performed on a Voyager-DE system (PerSeptive Biosystems, USA) and data were analyzed using Data Explorer software.

5.3.1 Synthetic Procedures

2-azido-N-(pyren-1-ylmethyl)ethanaminium chloride (PyAA+). A portion of 2-Azidoethylamine (79 mg, 0.92 mmol) was added to a solution of 1-pyrenecarboxaldehyde (214 mg, 0.93 mmol) in a mixture of CH_2Cl_2 (5 mL) and MeOH (7 mL) under an atmosphere of nitrogen. After stirring at ambient temperature for 30 min, $NaBH_3CN$ (93 mg, 1.5 mmol) was added in one portion and the reaction continued stirring for 3 d. The solvent was then removed under a stream of N_2. The residue was taken up in CH_2Cl_2 (20 mL) and washed with 5 M HCl (10 mL), leading to the formation of a pale yellow precipitate, which was collected by vacuum filtration and dried under vacuum (170 mg, 54%).

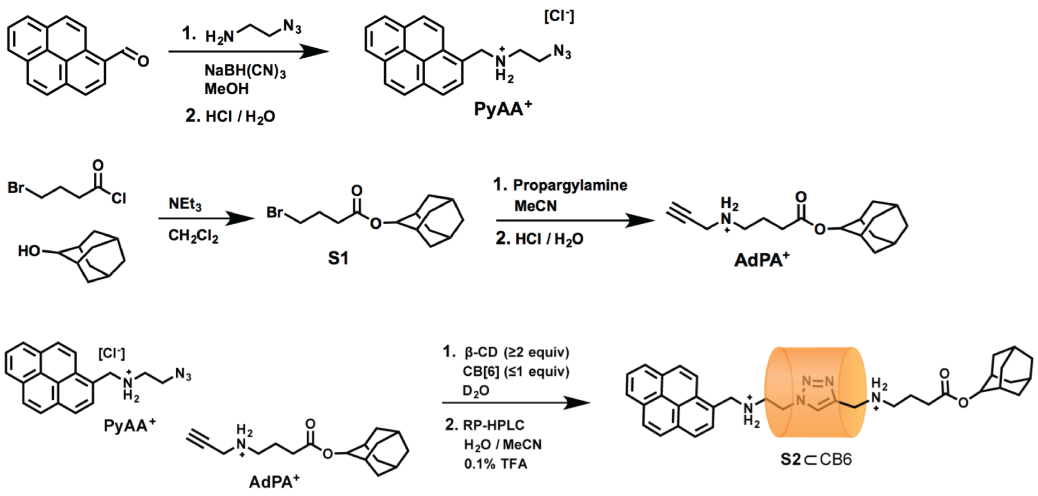

Figure 5.2: The three part synthetic process for generating S2⊂CB6 an activatable rotaxane that releases CB6 into the surrounding environment when exposed with LiOH.

2-Adamantyl 4-bromobutanoate (5.2). A portion of 4-Bromobutyryl chloride (1.6 mL, 14 mmol) was added to a mixture of 2-adamantanol (650 mg, 4.2 mmol) and triethylamine (1.6 mL, 11 mmol) in CH_2Cl_2/THF (1:1 v/v, 30 mL). The reaction stirred at ambient temperature for 3 h, under an atmosphere of N2. The reaction mixture was poured into 0.1 M HCl (20 mL) and extracted with CH_2Cl_2 (3 20 mL). The organic extracts were combined, dried ($MgSO_4$), filtered, concentrated, and subjected to flash column chromatography on SiO_2, eluting with CH_2Cl_2 to afford the product as a white solid (530 mg, 41%).

4-(2-adamantoxy)-4-oxo-N-(prop-2-ynyl)butan-1-aminium (AdPA+). Propargylamine (600 mg, 11 mmol) was added to a solution of compound S1 (315 mg, 1.04 mmol) in MeCN (6 mL) and the mixture was stirred at 60 C for 18 h, under an atmosphere of N_2. The solvent was removed under reduced pressure and the residue was combined with CH_2Cl_2 (4 mL), producing an orange precipitate of predominantly propargylammonium bromide. The precipitate was removed via filtration and the filtrate was diluted with CH_2Cl_2 (8 mL) and washed with 2 M HCl (10 mL). The organic layer was dried under vacuum to afford the product as a pale tan-colored solid (301 mg, 92%).

PyAA-CB6-AdPA-rotaxane (S2⊂CB6). Compounds PyAA+ (3.5 mg, 10 mol), AdPA+ (3.2 mg, 10 mol), CDXH_2O (40 mg), and CB6XH_2O (10.8 mg) were mixed in D2O (2 mL) and stirred at 60 C for 1 h under an atmosphere of N_2. ^{1}H NMR spectroscopy indicated that AdPA+ was converted quantitatively to the CD-capped CB6-rotaxane. The solution was purified by semi- preparative RP-HPLC, eluting in an aqueous gradient of 5% to 95% MeCN/0.1% TFA in H_2O/0.1% TFA over 40 min at a flow rate of 3.0 mL/min. After removal of the solvent, S2⊂CB6 was obtained as an off-white powder.

5.3.2 Responsive cleavage of CB6-rotaxanes

LiOH-induced cleavage of S2⊂CB6, monitored by HPLC and MS. To a solution of 5 mM S2⊂CB6 in 500 μL H_2O was added CDXH_2O (6.5 mg). The solution was heated to 40 C and gently sonicated until soluble to afford 2⊂CB6. To that solution was added 10 equiv of LiOH as a 1 M solution. The solution was stirred and heated at 40 C. Aliquots of 100 μL were taken at timepoints of interest and analyzed by RP-HPLC, eluting in an aqueous gradient 10% to 90% MeCN/0.1% TFA in H_2O/0.1% TFA over 20 min at a flow rate of 0.5 mL/min, monitoring at the Abs340 of pyrene. At the last timepoint of 8 h, a 100 μM solution was prepared in ddH_2O for analysis by ^{129}Xe NMR. At 8 h, an additional aliquot was taken for analysis by MALDI-TOF-MS to confirm the cleavage product 3VCB6. HRMS (MALDI-TOF-MS): m/z calculated for C62H66N29O14 [M+H]+ 1441.37, observed 1435.4.

5.3.3 Xenon NMR

Xenon polarization was obtained using a home built spin-exchange optical-pumping setup resulting in a 10% polarization of a xenon gas mixture (2 % Xe, 10% N_2, 88% He). The hyperpolarized gas was bubbled directly into a 5 mm phantom containing the solution of interest for 20 s then left to settle for 2 s. The sample was held at 3.4 atm and 25 C throughout. A 9.4 T (400 MHz) Varian VNMRS console was used for all hyperCEST experiments with optimized saturation power and duration for each sample (1CB6 sample: 15 dB, 5 s, 2⊂CB6 : 0 dB, 8 s). A standard hyperCEST pulse sequence was used sweeping the saturation frequency in 100 Hz or 500 Hz increments over a 200 ppm range.S4 Data processing was carried out using MATLAB. FIDs were zero-filled to 16384 points, baseline was corrected, apodized with an 11 Hz exponential, and a Fourier transform was performed. Each ^{129}Xe@H_2O areas in the spectra were integrated and the contrast of each spectrum was compared between the maximum and minimum area in each data series. Each profile was fitted with Lorentz profile using ORIGINLAB.

5.4 Results and Discussion

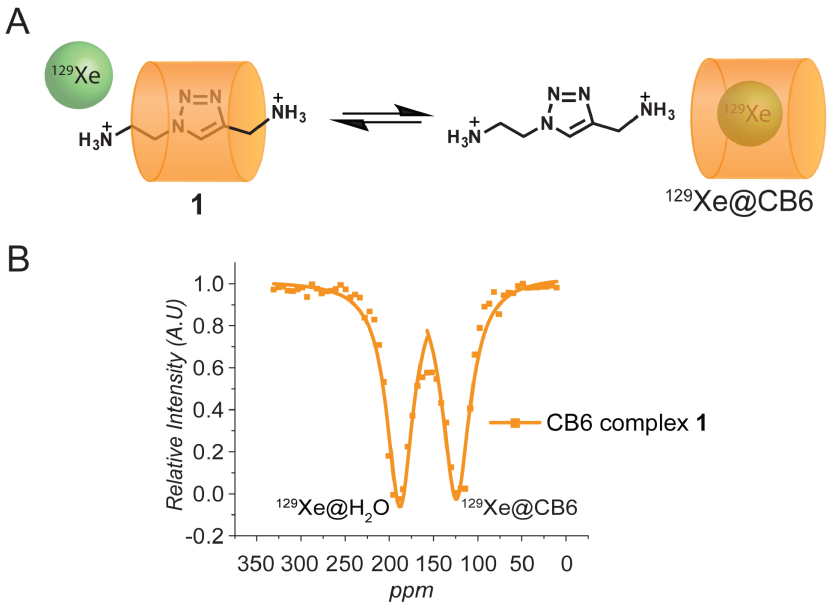

Figure 5.3: 1CB6 demonstrates competitive host-guest interactions between 1CB6 and ^{129}Xe@CB6. (A) Scheme outlining the dynamic host-guest interactions of 1CB6 and ^{129}Xe. (B) ^{129}Xe HyperCEST NMR spectrum of 1CB6 (100 μM). A strong ^{129}Xe@CB6 peak was observed.

The rotaxanes used in this work were synthesized by CB6-catalyzed azide-alkyne 1,3-dipolar cycloaddition, which is routinely used for CB6-rotaxane synthesis and is a facile method for the preparation of rotaxanes with diverse functional groups for various applications [99] [100] [101] [102] [103]. Dmochowski et al. previously reported that CB6 incubated with excess putresceine guests led to a suppression of ^{129}Xe@CB6 NMR signals [75]. However, in equal concentrations of competitors relative to CB6, little change in the ^{129}Xe@CB6 hyperCEST NMR signal was observed. Schroder et al. similarly observed that excess concentrations of cadaverine were able to suppress ^{129}Xe@CB6 signals. Since both of these competing guests were alkanediammonium ions, the triazole-diammonium recognition unit of our rotaxane platform might therefore pose a challenge to CB6 detection if it were able to overwhelm ^{129}Xe@CB6 interactions through complex competition. To test if this competition could inherently suppress ^{129}Xe@CB6 signals, we synthesized 1 complexed to CB6 (1⊂CB6, 5.3). Complex 1⊂CB6 lacks the stoppers of a full rotaxane, allowing the ring and axle components to exchange easily in solution. This construct therefore represents a model for the post- cleavage product of an activated CB6-rotaxane. A strong ^{129}Xe@CB6 peak was observed by ^{129}Xe hyperCEST NMR, approaching complete saturation of the dissolved xenon signal. While there is an active competition between 1CB6 and ^{129}Xe@CB6 complexes, at

equal concentrations of 1 and CB6, xenon was still able to exchange rapidly between the bulk water and the CB6 molecules, giving a strong hyperCEST response. These observations are in agreement with previous competition studies [75] [96] [97].

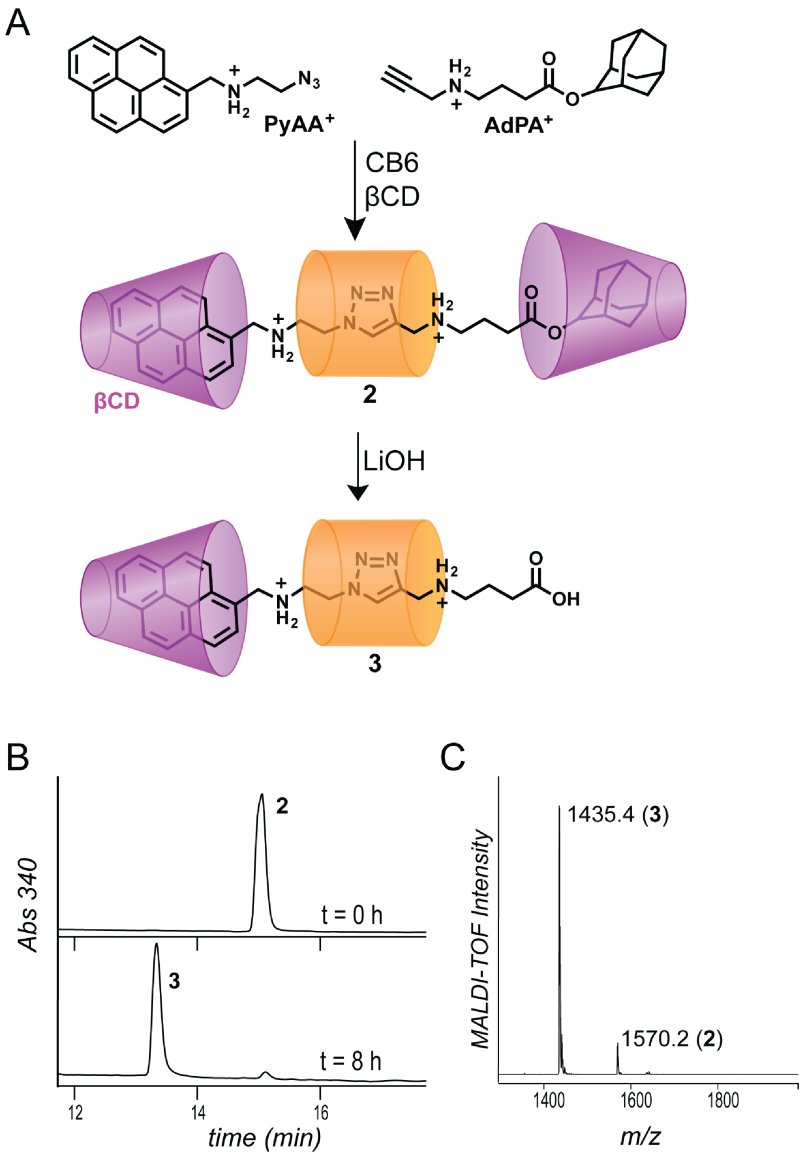

Figure 5.4: βCD2$\supset$2$\subset$CB6 exhibits responsive rotaxane cleavage. (A) CD2$\supset$2$\subset$CB6 containing a labile ester bond was synthesized with β-cyclodextrin (CD) caps to improve water solubility and to accelerate the rotaxane capture reaction. (B) HPLC traces monitoring the cleavage rate of βCD2$\supset$2$\subset$CB6 (15 min) when exposed to 10 equiv of LiOH at 40 C. Near complete conversion to βCD$\supset$3$\subset$CB6 (13 min) was observed by 8 h. (C) MALDI-TOF MS confirmed the presence of ester-hydrolysis product CD$\supset$3$\subset$CB6 at 1435 m/z.

Once it was confirmed that a competitive triazole-diammonium guest would not prohibitively block ^{129}Xe@CB6 interactions, we set out to synthesize a chemically activated CB6-rotaxane that could completely suppress the ^{129}Xe@CB6 NMR signal until undergoing a controlled cleavage and subsequent release of CB6 for xenon binding. CD22CB6 was synthesized with pyrene-functionalized 2-azidoethylamine (PyAA+) and an adamantly-ester-functionalized propargylamine (AdPA+) as rotaxane stoppers (5.4). - cyclodextrin (CD) caps were added to improve the solubility of the end groups and to accelerate the rotaxane capture reaction.15 Compared to previous xenon sensors, which have relied on direct CryA conjugates,7-9 this synthetic strategy provides a facile and modular approach. To confirm that the CD caps would not interact with xenon and affect the ^{129}Xe hyperCEST response of CD2⊃2⊂CB6, CD alone in solution was measured and revealed no measurable background ^{129}Xe hyperCEST signals.

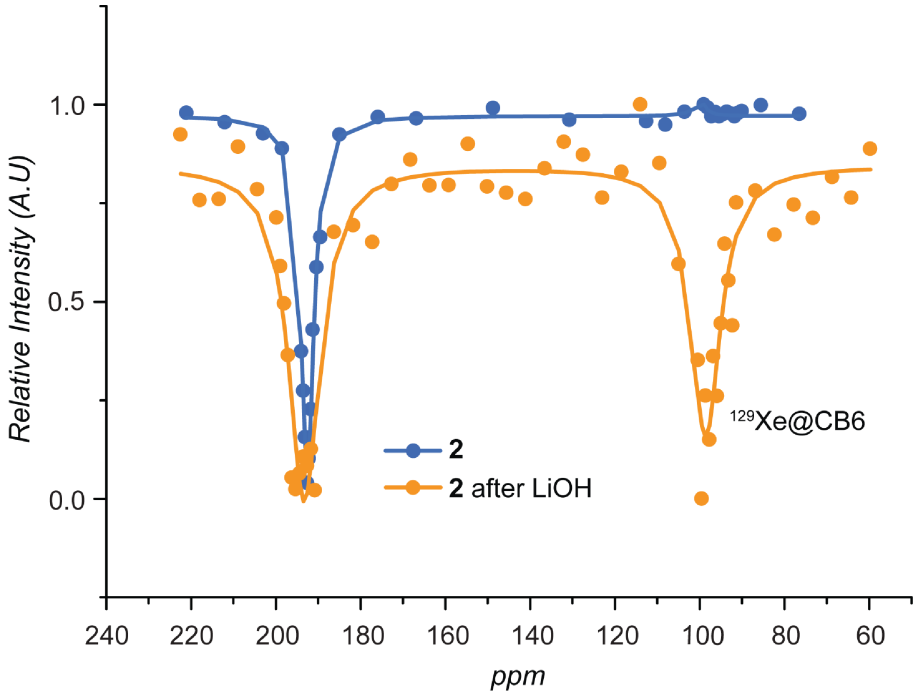

Figure 5.5: βCD2⊃2⊂CB6 can be activated for ^{129}Xe hyperCEST NMR. ^{129}Xe-hyperCEST NMR spectra of 100 M CD2⊃2⊂CB6 displayed no significant ^{129}Xe@CB6 signal. After exposure to 10 equiv of LiOH at 40 C a substantial increase in the ^{129}Xe@CB6 peak was observed.

The ^{129}Xe hyperCEST response of CD2⊃2⊂CB6 revealed no detectable ^{129}Xe@CB6 signal even at 100 M CD2⊃2⊂CB6 (5.5). Free CB6 in solution is easily detected at low nanomolar concentrations;10a,b thus it is revealing that even at relatively high concentrations of CD2⊃2⊂CB6, no CB6 was detected. These results demonstrate that ^{129}Xe is completely prevented from exchanging with the CB6 cavity and producing a hyperCEST response

when CB6 is locked to the rotaxane complex. In contrast to previous work that explored supramolecular CB6 competition between xenon and competing guests,10a,12 CD2⊃2⊂CB6 demonstrated complete suppression of ^{129}Xe@CB6 signals without using excess concentrations of 2 relative to CB6.

To create an activated CB6-rotaxane for ^{129}Xe NMR, CD2⊃2⊂CB6 was synthesized with a labile ester group that can be hydrolysed to CD⊃3⊂CB6 and lead to the release of CB6. Treatment with 10 equiv of LiOH led to the complete ester hydrolysis of CD22CB6 to CD⊃3⊂CB6 by 8 h, as confirmed by high performance liquid chromatography (HPLC) and mass spectrometry (MS) (5.4). After treatment with LiOH, a significant ^{129}Xe@CB6 peak was observed, demonstrating the activated nature of the CD2⊃2⊂CB6 complex. The activated CD⊃3⊂CB6 produced a nearly saturated ^{129}Xe@CB6 signal, similar to 10 μM free CB6 in solution (5.6). Thus, even in complexes containing a single bulky rotaxane stopper and a terminal carboxylate on the axle portion of the rotaxane, it is possible to maintain the exchange rates between xenon and CB6 that are necessary to produce a hyperCEST response.

S7. ^{129}Xe HyperCEST NMR of CB6

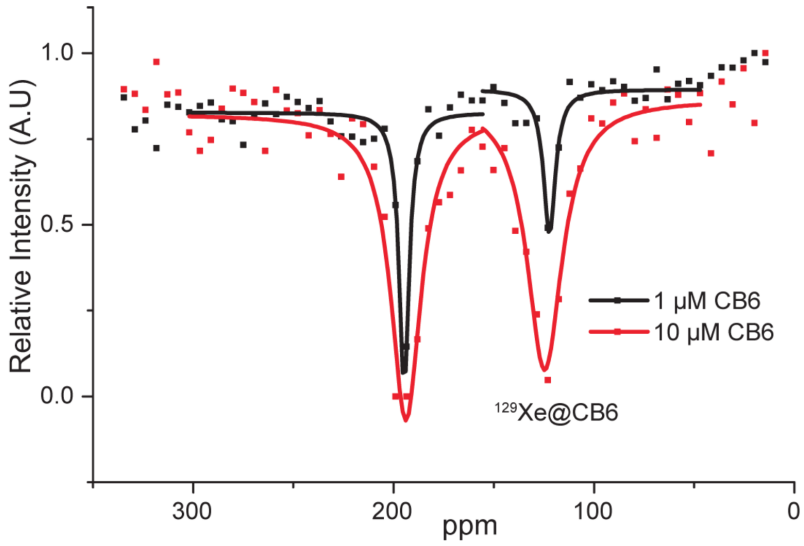

Figure 5.6: HyperCEST response of CB6 in water at 10 and 1 μM.

As CB6 continues to gain attention for its improved hyperCEST response over previously used CryA constructs, it is increasingly important to be able to manipulate CB6 for diverse applications in NMR detection and MRI. These results demonstrate that ^{129}Xe@CB6 NMR signals can be completely suppressed by locking CB6 into a rotaxane mechanical bond until a specific cleavage event occurs and releases CB6 to produce a ^{129}Xe@CB6 signal. This activated ^{129}Xe NMR sensor can be easily synthesized and modulated with different cleavable

linkers for tunable activation, and diverse rotaxane stoppers with varying functionalities. This design therefore presents the opportunity for CB6 to be used for applications in activated xenon NMR detection coupled with drug delivery, biomarker targeting, and multimodal imaging. Based on this study, future work will focus on expanding CB6-rotaxanes for different applications and stimuli, and exploring new rotaxane systems with higher sensitivities for in vivo detection.

5.5 Conclusions

The success of this CB6-rotaxane suggest that more specialized rotaxanes could be created with targetted regions for the detection of biologically significant enzymes. By replacing the backbone region that is cleaved using LiOH with a peptide sequence recognied by an enzyme we can generate a hyperCEST response activated by the presence of an enzyme. This would also require extending the rotaxane backbone giving the CB6 more freedom while techered, and the effects of this will be looked at in the following chapter.

Chapter 6

Rotaxane probes for protease detection by ^{129}Xe hyperCEST NMR

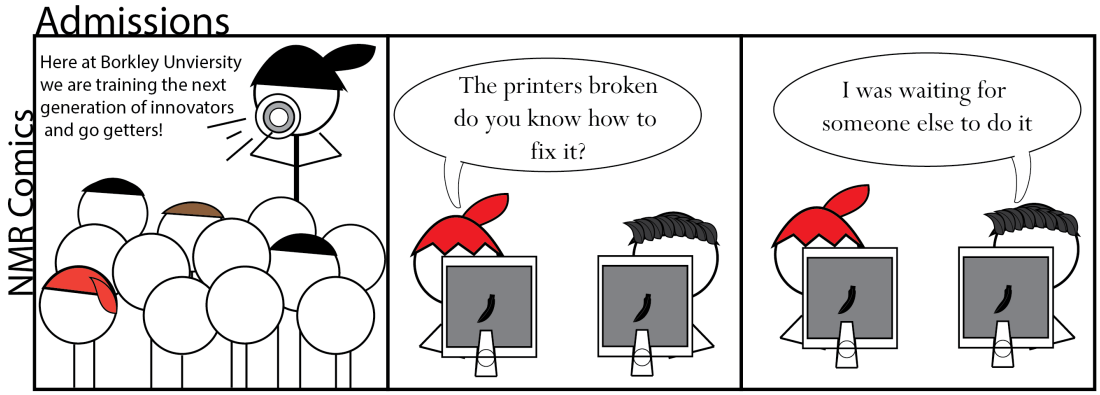

This chapter was done in collaboration with Joel A. Finbloom and will be published in a peer reviewed journal.

6.1 Abstract

Proteases are widely used targets for disease detection with small molecule probes. ^{129}Xe hyperCEST NMR is a promising analytical tool due to its high sensitivity and molecular detection capabilities, but the reports of protease probes for hyperCEST have been limited. We previously reported a new class of activated hyperCEST agents using cucurbit[6]uril (CB6) rotaxanes, whereby a hyperCEST response is produced upon the cleavage of a CB6 rotaxane by a chemical event. The subsequent increase in ^{129}Xe@CB6 interactions produces a hyperCEST response far above background levels. Herein, we take advantage of this platform for the design and implementation of CB6 rotaxanes as probes for protease detection, whereby a protease of interest cleaves a peptide recognition sequence on the rotaxane, increasing the accessibility of CB6 for xenon interactions. The peptide sequences on the axle component

of the rotaxanes were studied to determine which amino acids facilitated or hindered hyperCEST responses. Additionally, two different CB6 rotaxane probes for protease detection were synthesized for the detection of chymotrypsin as a model system, and for the detection of matrix metalloprotease 2 (MMP-2), which is overexpressed in cancer tissue. Both rotaxanes successfully produced hyperCEST responses when incubated with their target enzyme, demonstrating that these tunable CB6 rotaxane probes can be used for protease detection.

6.2 Introduction

Small molecule probes are promising tools for disease detection, and are used in a variety of platforms including fluorescence, ^{1}H nuclear magnetic resonance (^{1}H NMR) spectroscopy, and ultrasound imaging [104] [86] [105]. These methods rely on suppressing background signals until a chemical or biological event occurs and activates the probe, at which point a detectable signal is generated. This strategy has been used to detect enzymes [86] [105], [106] signaling molecules, and redox conditions, among other targets. Proteases, in particular, are widely used targets for disease detection, as certain proteases are overexpressed in disease tissues and cells [105] [107] [108]. Proteases have the added benefits of being catalytically active, such that only a small amount is required to activate the probe. They can also be highly specific in their recognition motifs. While proteases have been used in several detection platforms, the reports of such probes for ^{129}Xe NMR have been limited.

^{129}Xe NMR is a versatile tool that takes advantage of host-guest interactions to gain insight into a molecular environment [37] [35]. By use of spin-exchange optical-pumping for hyperpolarization, signals can be increased by more than four orders of magnitude, allowing for extremely sensitive detection [12] [64]. The polarizability of ^{129}Xe atoms makes them highly sensitive to their chemical environment, and thus they can be used to detect changes in temperature, pH, and liquid crystal ordering [71] [109]. Further developments using chemical exchange saturation transfer (CEST) with ^{129}Xe hyperpolarization (hyperCEST) have created a means for ultrasensitive magnetic resonance molecular detection. HyperCEST exploits the fast exchange of the xenon in and out of a macromolecular host on the NMR time scale to reduce the observed signal of the xenon dissolved in water. By saturating the signal from xenon that interacts with the molecular host (^{129}Xe@host) the overall dissolved signal is reduced, allowing for indirect but highly sensitive detection [30].

Since the development of ^{129}Xe hyperCEST techniques, ^{129}Xe hosts have been conjugated to targeting groups and chemical shift agents for applications in cancer imaging and analyte detection [110] [93] [77]. Typically, cryptophane-A (CryA) has been the ^{129}Xe host of choice for these applications; however, the low solubility of CryA creates difficult synthetic procedures and low yields. Previously, cucurbit[6]uril (CB6) was reported as a promising ^{129}Xe host for hyperCEST NMR [75] [39]. Recent work took advantage of known CB6 supramolecular host-guest interactions [96] to alter the ability of CB6 to participate in CEST in response to enzymatic reactions or protein binding. This strategy allowed for the detection of avidin, carbonic anhydrase II, and lysine decarboxylase [98] [111]. These approaches relied on competitive binding, where the target needed to be in significant excess to inhibit

xenon interactions. For more biologically complex systems, it is necessary for CB6 to be mechanically locked into a rotaxane such that CB6 can be effectively delivered to a region of interest without any background CB6 release. Our recent work described a model turn-on system whereby CB6 was released upon hydrolysis of an ester bond [29]. By mechanically locking CB6 into a rotaxane, we were able to suppress the CB6 hyperCEST response until a chemical event cleaved the rotaxane, producing a CEST response via increased ^{129}Xe@CB6 interactions. In this work, we describe a new CB6 rotaxane system that can allow sensitive and selective protease detection by ^{129}Xe hyperCEST NMR.

6.3 Methods

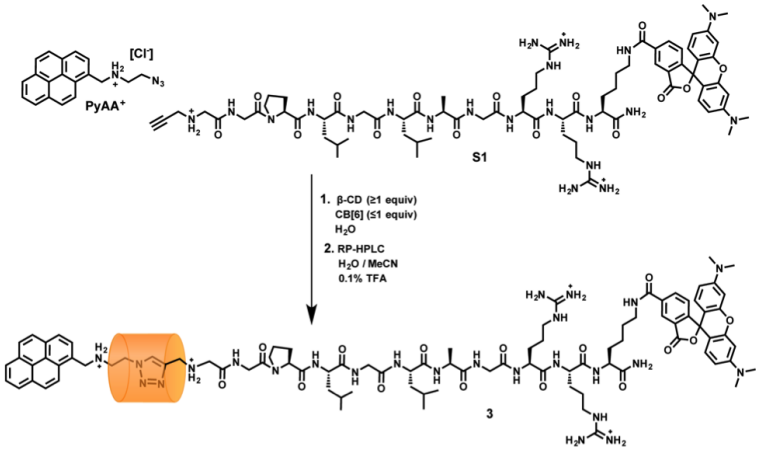

Figure 6.1: Synthetic procedure for CB6 rotaxane with an MMP-Cleavable peptide sequence

PyAA-CB6-peptide rotaxanes (2a-j, 3). Compounds PyAA+ (1 equiv, 2-10 mol) and CDXH_2O (1.3 equiv) were mixed in H_2O and stirred at 60 C to allow for complexation. Once PyAA+ dissolved, the solution was added to one of peptides 1a-j or S1 (1 equiv), and the solution was then transferred to an Eppendorf charged with CB6XH_2O (1 equiv). The solution was stirred at 60 C for 6 h repaired from light, and the reaction was monitored by MALDI-TOF MS (6.1). The solution was then filtered with a 0.2 m spin filter to remove unreacted CB6, and the product was purified by semi-preparative RP-HPLC, eluting in an aqueous gradient 10% to 90% MeCN/0.1% TFA in H_2O/0.1% TFA over 35 min at a flow rate of 3.0 mL/min. After lyophilization, rotaxanes 2a-j were obtained as off-white powders and 3 was obtained as a deep pink powder. HRMS (MALDI-TOF-MS): 2a. m/z calcd for $C_{68}H_{72}N_{33}O_{18}$ [M+H]+ 1638.27, observed 1638.65. 2b. m/z calcd for $C_{71}H_{76}N_{33}O_{18}$ [M+H]+ 1678.53, observed 1677.97. 2c. m/z calcd for $C_{72}H_{80}N_{33}O_{18}$ [M+H]+ 1694.57, observed 1693.38. 2d. m/z calcd for $C_{75}H_{84}N_{33}O_{18}$ [M+H]+ 1734.64, observed 1734.04. 2e. m/z calcd for $C_{72}H_{81}N_{34}O_{18}$ [M+H]+ 1709.35, observed 1708.46. 2f. m/z calcd for $C_{70}H_{74}N_{33}O_{20}$ [M+H]+ 1696.28, observed 1696.37. 2g. m/z calcd for $C_{75}H_{78}N_{33}O_{19}$ [M+H]+ 1744.32, observed 1744.23.2h. m/z calcd for $C_{72}H_{81}N_{36}O_{18}$ [M+H]+ 1737.35, observed 1737.16. 2i. m/z

calcd for $C_{72}H_{81}N_{36}O_{18}$ [M+H]+ 1737.35, observed 1738.04. 2j. m/z calcd for $C_{72}H_{81}N_{36}O_{18}$ [M+H]+ 1737.35, observed 1737.89. 3. m/z calcd for $C_{12}9_{H1}5_{9N}4_{9O}27$ [M+H]+ 2825.97, observed 2825.38.

Chymotrypsin-induced cleavage of rotaxane 2e, monitored by MS. To a solution of 50 μM 2e in 1 mL of 10 mM sodium phosphate buffer pH 7.0, was added chymotrypsin as a 32 μM solution for a final concentration of 5 nM chymotrypsin. The solution was incubated at 37 C for 72 h. The reaction was monitored by MALDI-TOF MS, and the cleavage product 4 was confirmed. After incubation, the solution was measured by ^{129}Xe hyperCEST NMR. HRMS (MALDI-TOF-MS): m/z calcd for 4 $C_{71}H_{76}N_{33}O_{18}$ [M+H]+ 1630.27, observed 1631.20.

MMP-2-induced cleavage of rotaxane 3, monitored by HPLC and MS. To a solution of 100 M 3 in 150 L MMP-2 buffer (40 mM TRIS-Cl, 8 mM Zn2+, 8 mM Ca2+, 8 mM Na2PO4/NaPO4, 0.04% Brij-35, pH 7) was added MMP-2 (active catalytic domain, Enzo Life Sciences, Farmingdale, NY) as a 0.1 mg/mL solution for a final concentration of 100 nM MMP-2, and the solution was incubated at 37 C. Aliquots (25 L) were taken at each timepoint of interest and analyzed by RP-HPLC eluting with an aqueous gradient of 10% to 90% MeCN/0.1% TFA in H_2O/0.1% TFA over 20 min at a flow rate of 0.5 mL/min, monitoring at the Abs560 of rhodamine. Cleavage products 2d and 5 were confirmed by MALDI-TOF MS. At 24 h, the solution was diluted in ddH_2O to 5 M 3 and 5 nM MMP-2, and a ^{129}Xe hyperCEST spectrum was obtained. HRMS (MALDI-TOF-MS): m/z calcd for 2d $C_{75}H_{84}N_{33}O_{18}$ [M+H]+ 1734.64, observed 1730.5. HRMS (MALDI-TOF-MS): m/z calcd for 5 $C_{54}H_{79}N_{16}O_{10}$ [M+H]+ 1112.3, observed 1109.5.

Xenon hyperCEST NMR. Xenon polarization was achieved using a home built spin-exchange optical-pumping setup resulting in a 10% polarization of a xenon gas mixture (2 % Xe, 10% N_2, 88% He) [23]. The hyperpolarized gas was bubbled directly into a 5 mm phantom containing the solution of interest for 20 s then left to settle for 2 s. The sample was held at 3.4 atm and 25 C throughout. A 9.4 T (400 MHz) Varian VNMRS console was used for all hyperCEST experiments with optimized saturation power and duration for each sample. A standard hyperCEST pulse sequence was used sweeping the saturation frequency in 1000 Hz increments 7000 Hz to 29000 Hz, also including a measurement at 11250 and 11500 Hz where CB6 is typically observed, and at 19500 Hz, corresponding to the center of the ^{129}Xe@H_2O peak covering a 200 ppm range in total. The saturation pulse length was 4 s for three cycles at 20 dB. For % CEST effect data, an on/off saturation experiment was conducted saturating at the center of the CB6 peak then switching to 29000 Hz on the other side of the ^{129}Xe@H_2O peak alternating 8 times for a total of 4 on saturation and 4 off saturation values. Data processing was carried out using MATLAB. FIDs were zero-filled to 16384 points, baseline was corrected, apodized with an 11 Hz exponential, and a Fourier transform was performed. Each ^{129}Xe@H_2O areas in the spectra were integrated and the contrast of each spectrum was compared between the maximum and minimum area in each data series. Each profile was fitted with Lorentz profile using ORIGINLAB.15

6.4 Results

6.4.1 Effects of peptide sequence on rotaxane hyperCEST response.

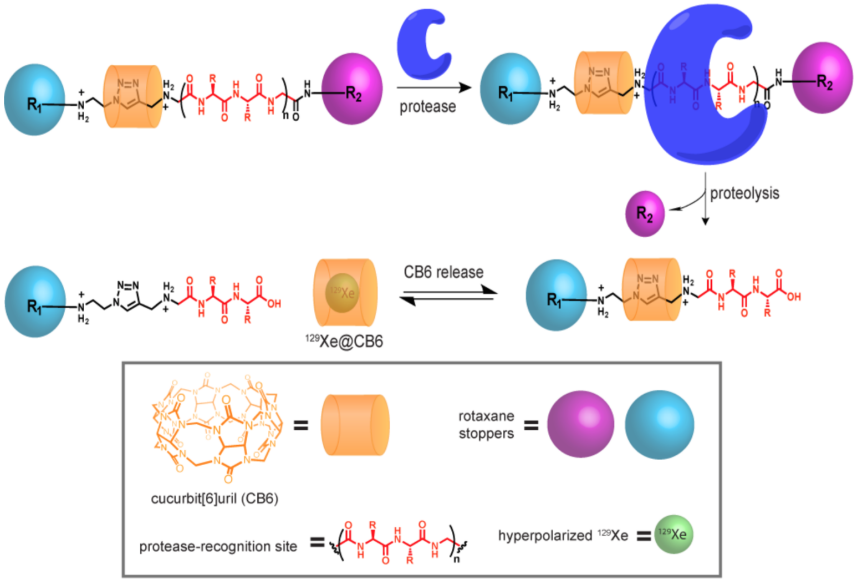

Figure 6.2: CB6 rotaxanes containing a protease cut sequence are cleaved specifically in the presence of an enzyme of interest. Upon cleavage of the rotaxane, CB6 becomes more accessible to host ^{129}Xe and produce a hyperCEST response.

To create CB6 rotaxane probes for protease detection, our design involved the incorporation of peptide sequences into the axle component of the rotaxane (6.2). These peptides can be synthesized to contain any sequence, including protease recognition sequences of interest. After proteolysis events, a portion of the peptide sequence remains on the axle component of the rotaxane, leaving a post-cleavage product whereby CB6 is not necessarily mechanically locked, and could be released from the rotaxane. In theory, this design can therefore be used to detect any of a wide variety of proteases using ^{129}Xe hyperCEST NMR if CB6 becomes more accessible for ^{129}Xe interactions following proteolysis.

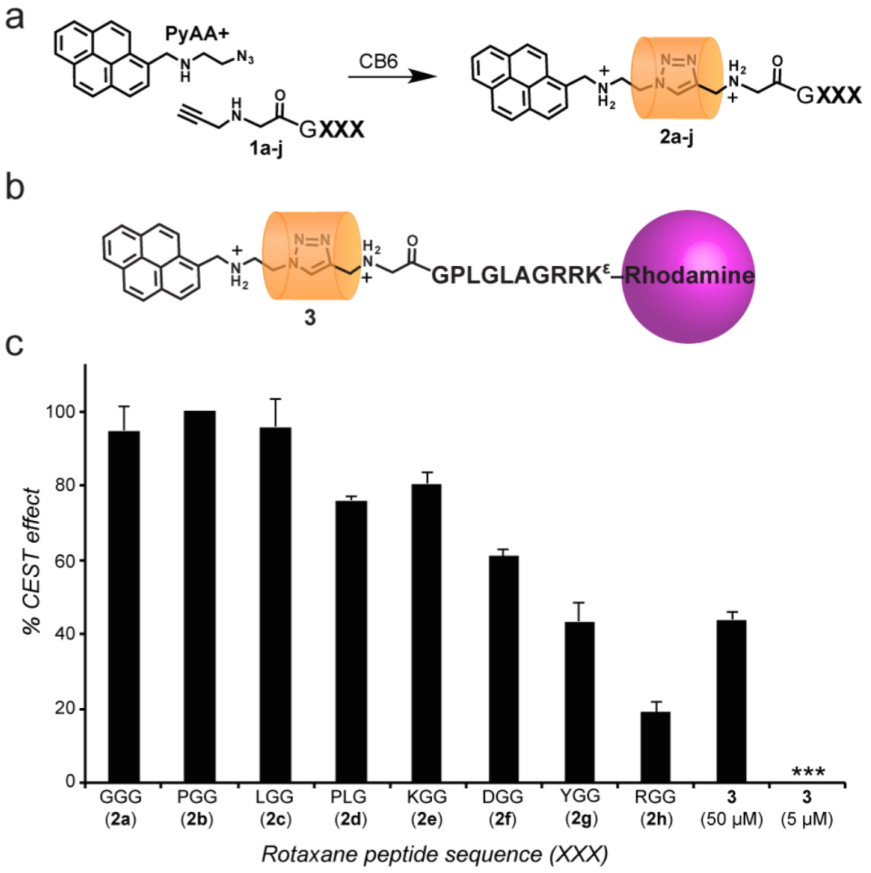

Figure 6.3: (a) CB6 rotaxanes with varying peptide sequences were synthesized using CB6-catalyzed azide- alkyne click chemistry. (b) A mechanically locked rotaxane was synthesized with a rhodamine dye as a stopper to prevent CB6 from dissociating. (c) The percent CEST effect was measured for the rotaxane series at 50 μM rotaxane in pH 7 phosphate buffer to determine the impact of amino acid identity on the ability of CB6 rotaxanes to undergo CEST. Error bars represent standard instrumental error for n=4. ***No detectable signal was observed for 3 at 5 μM.

We previously observed that CB6 bound to triazole-diammonium guests without any bulky stoppers or additional axle components reduced the hyperCEST effect when compared to free CB6 in solution. This is likely due to an equilibrium that exists between triazole-bound and unbound CB6 6.2.

To study how the steric and electronic contributions from the axle peptide sequences could affect CB6 release and subsequent hyperCEST response of the CB6 rotaxanes, we synthesized a series of peptide rotaxanes using a CB6-catalyzed azide-alkyne cycloaddition (6.3 a). This synthetic strategy is widely used in rotaxane synthesis and provides a one step, straightforward, and modular route to a variety of CB6 complexes [99] [100] [101]. Furthermore, many types of bulky molecules can be used as stoppers on these rotaxanes, allowing for

diverse applications and functionalities to be coupled with hyperCEST NMR detection. For this peptide rotaxane screen, the amino acids were varied to determine the effect of amino acid identity on the percent CEST effect of the CB6 rotaxanes. The temperature was held constant at 25 C and several different concentrations were tested. At high concentrations of rotaxane, complete saturation of the hyperCEST response limited comparisons between species. At 50 μM rotaxane, significant differences in the CEST response between species were obtained, and thereafter the concentration of rotaxanes was held constant so that any changes to the CEST response would be due to the peptide axle.

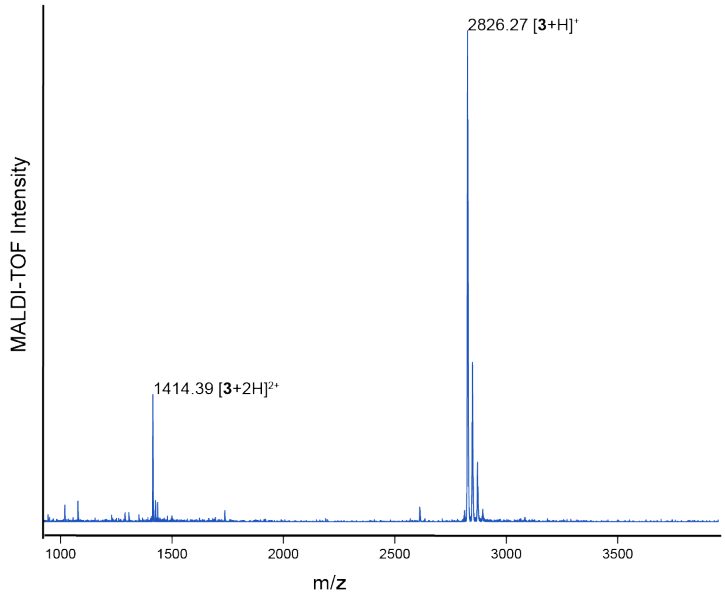

Figure 6.4: A Maldi-TOF of rotaxane 3 after synthesis showing sucessful creation of the rotaxane and no risidual CB6.

A hyperCEST spectrum for the mechanically locked rotaxane (3) was taken as a baseline to compare the varying peptide sequences, as there was no possibility for CB6 release from the rotaxane axle. Interestingly, a moderate CEST response was observed for the locked structure. Matrix assisted laser desorption time of flight mass spectrometry (MALDI-TOF MS) confirmed that rotaxane 3 remained intact after hyperCEST measurements were conducted, and no free CB6 was evident 6.4. This same hyperCEST response was not observed at the reduced 5 μM concentration of rotaxane 3, indicating that while bound, xenon is only able to interact weakly with the CB6 on the rotaxane. This phenomenon presents an interesting opportunity for the future functionalization of mechanically locked cucurbituril sensors that could act in the same "always on" way CryA has in past studies.

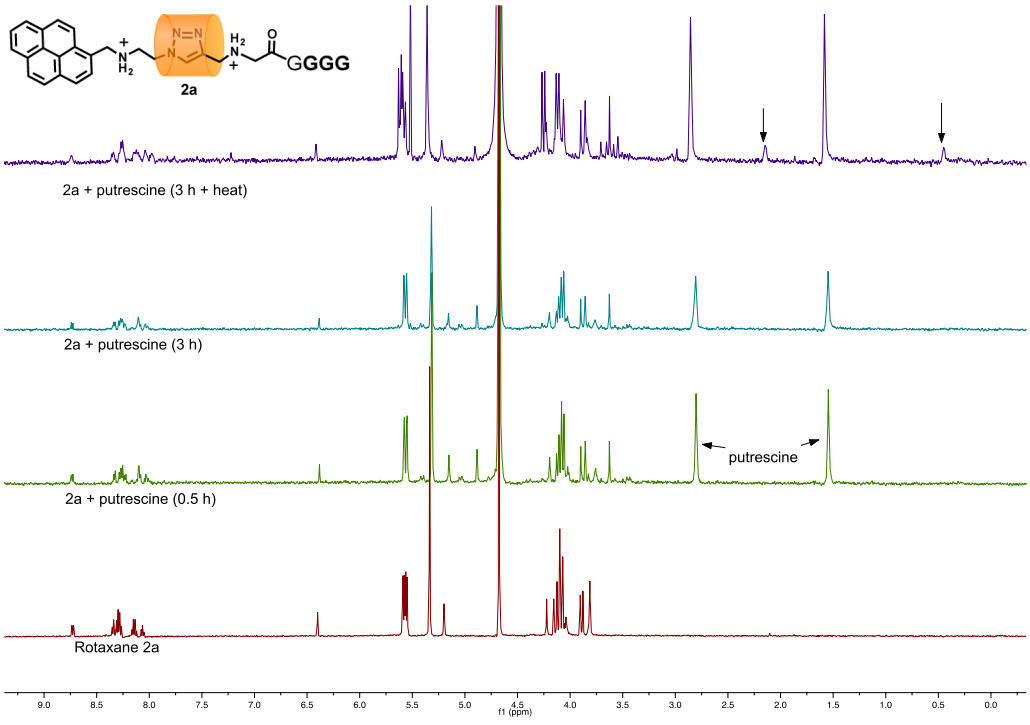

Figure 6.5: A competitive binding experiment with putracene showed no bound putracene peak (indicated with arrows) until the sample was heated to 100 ^{o}C indicating heating may allow more CB6 to free itself from the pseudo-rotaxane.

The most flexible of the peptide rotaxanes without a rhodamine stopper contained an oligoglycine chain (2a) and displayed complete saturation, a 100% CEST effect. To determine if the strong CEST effect of 2a derives from CB6 release from the rotaxane, a competition study was performed. Two equiv of putrescine, a known competitive guest of CB6 were added to a solution of rotaxane 2a, and NMR spectra were recorded over time 6.5. Upon addition of putrescine, and heating the sample to 100 ^{o}C and allowing it to cool, additional new chemical shifts were observed corresponding to putrescine-bound CB6, but without heating no new shifts were observed. This indicates that while the energetic barrier to CB6 release is high for rotaxane 2a, it is possible to induce CB6 release from the rotaxane for interaction with competing guests. Thus, in addition to any xenon interactions with the rotaxane-bound CB6, it may be that some amount of CB6 is released from the rotaxane, further increasing the CEST effect of rotaxane 2a.

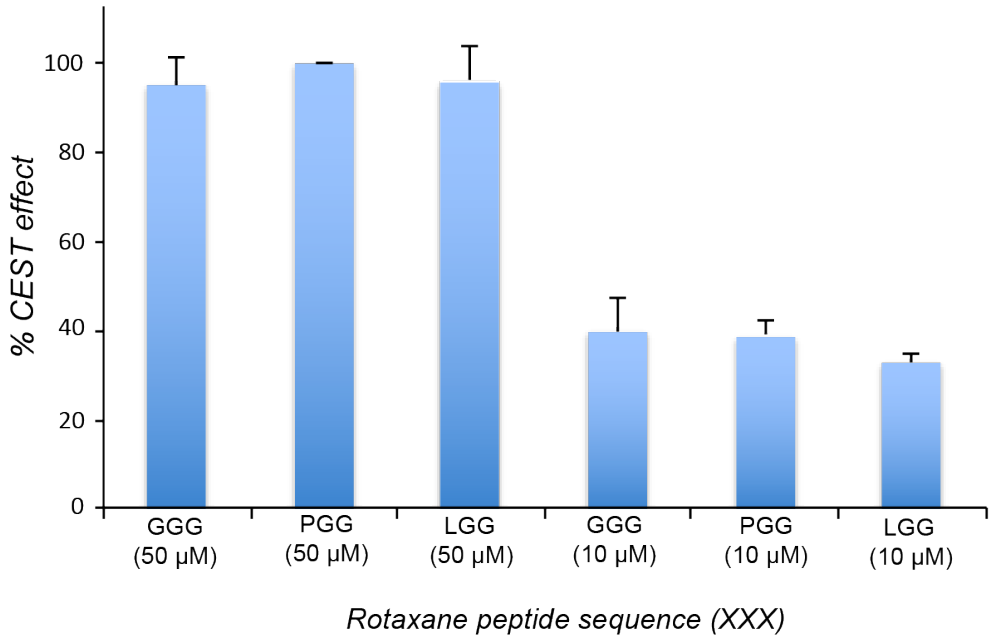

Figure 6.6: After dilution from 50 to 10 μM pseudo-rotaxanes 2a, 2b, and 2c still gave similar CEST responses indicating they similarly inhibit CB6 release.

The addition of Leu (2b) or Pro (2c) individually did not inhibit the CEST effect, and each gave a similar CEST effect of approximately 40% when the concentration was lowered to 10 μM 6.6. In a PLG sequence (2d), which corresponds to the post-cleavage product after proteolysis by matrix metalloprotease-2 (MMP-2), the CEST effect was reduced to 80% at 50 μM. This indicates that while the Pro turn or a bulky Leu R group alone did not significantly hinder ^{129}Xe@CB6 interactions, the combined steric bulk in the PLG sequence did inhibit CB6 accessibility to some extent, resulting in a minor reduction in CEST effect. To determine if electrostatics could affect the % CEST effect of the rotaxanes, Lys (2e) and Asp (2f) were incorporated into the CB6 rotaxanes. Both rotaxane 2e and 2f showed modest suppression of the CEST effect, possibly due to slight steric strain of finding a conformation where xenon could enter, or due to added charge-dipole contributions between the charged group and the CB6 urea moieties, slightly inhibiting CB6 accessibility.

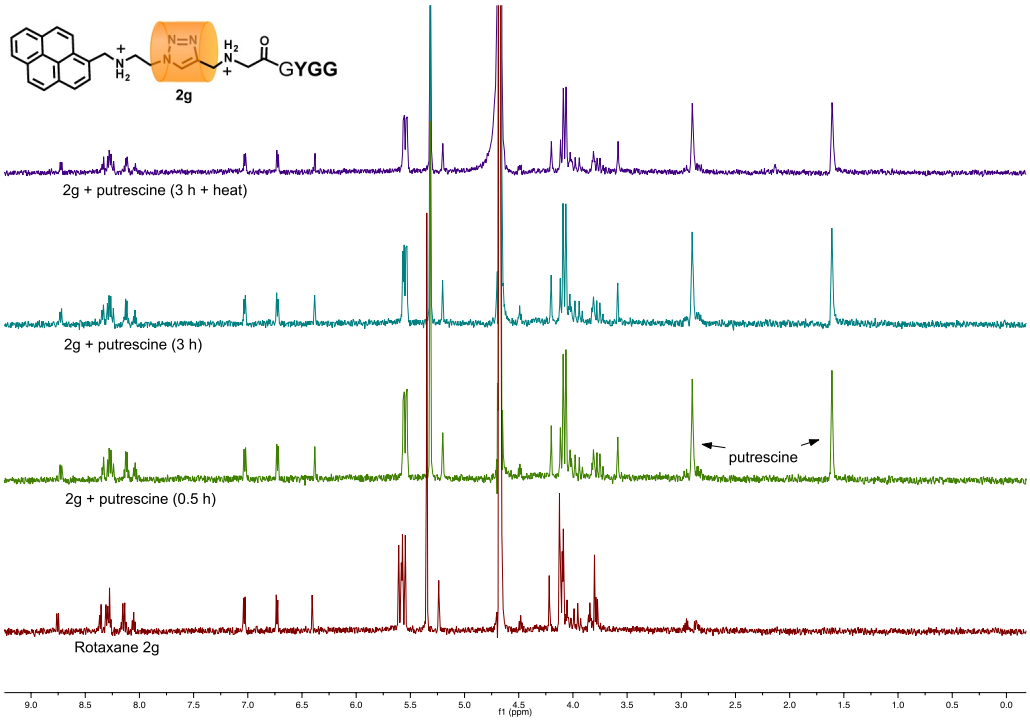

Figure 6.7: A competitive binding experiment with putracene showed only a very small amount of bound putracene peak after the sample was heated to 100 ^{o}C indicating the CB6 cannot leave pseudo-rotaxane 2g as easily as 2a.

We further observed that Tyr (2g) produced a similar CEST effect to rotaxane 3. In contrast to rotaxane 2a, when 2g was heated to 100 C in the presence of putrescine and allowed to cool back to room temperature, no new chemical shifts were observed (6.7). This indicates that CB6 bound to rotaxane 2g is not as accessible for competing guest interactions. The CEST response of 2g is therefore likely dominated by weak xenon interactions on the rotaxane-bound CB6, similar to rotaxane 3.

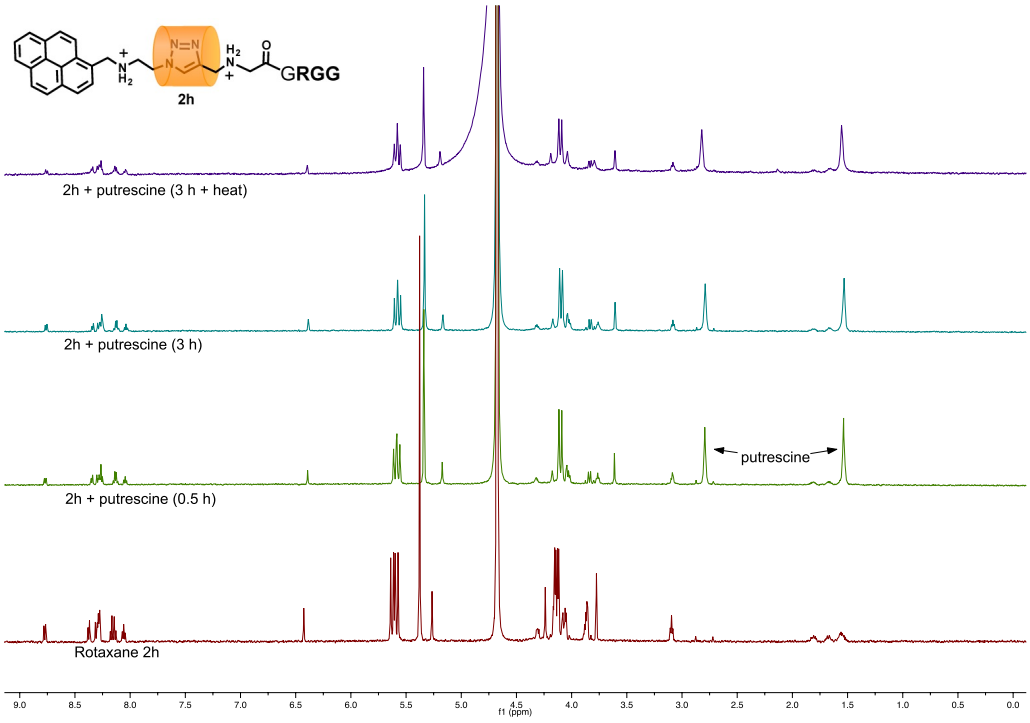

Figure 6.8: A competitive binding experiment with putracene showed only a very small amount of bound putracene peak after the sample was heated to 100 ^{o}C indicating the CB6 cannot leave pseudo-rotaxane 2h as easily as 2a.

Arg-bearing rotaxane 2h displayed minimal CEST (19% of max). Competition studies (6.8) confirmed that CB6 was unable to be released from rotaxane 2h upon competition with putrescine before and after heating the sample, similar to rotaxane 2e. However, the 19% CEST effect of 2h suggests that some additional interactions are at play, as the CEST response for 2h was weaker than for mechanically-locked CB6 in rotaxane 3. A potential charge-dipole interaction between the protonated Arg unit and the urea moieties of CB6 may be preventing both CB6 release and any rotaxane-bound ^{129}Xe@CB6 interactions. To elucidate this interaction, the Arg moiety was moved to three different positions on the rotaxane axle to see if it would change the observed CEST effect (6.9). By moving the arginine farther from the triazole, the CEST effect increases from 19% at the 3rd position (2h) to 66% at the 4th position (2i). Once the Arg is in the C-terminal position (2j) there is very limited suppression of the CEST effect, as there is no longer any branching with the oligoglycine axle.

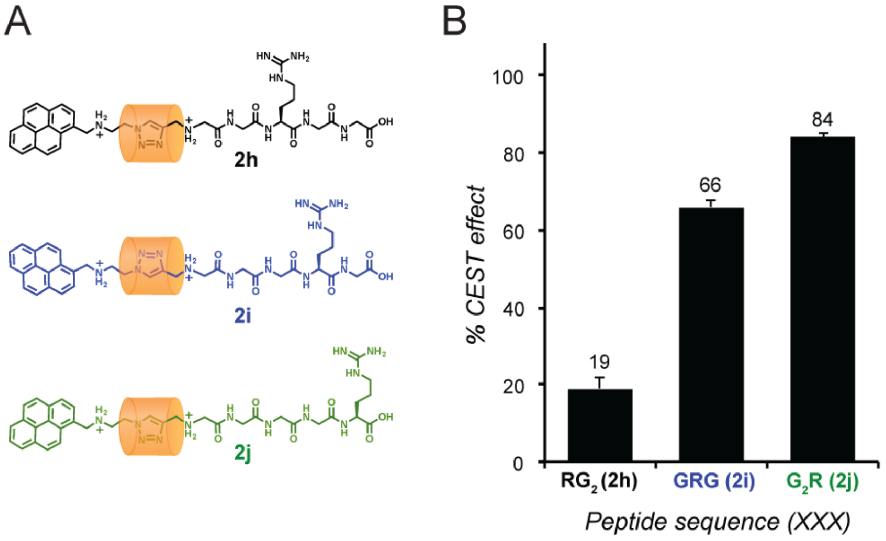

Figure 6.9: (a) Three CB6 rotaxanes (2h-j) were synthesized with varying distances between the Arg moiety and CB6 (b) Measuring the % CEST effect for each rotaxane demonstrates that Arg at the 3rd amino acid position (2h) significantly suppresses ^{129}Xe-CB6 interactions and therefore reduces the hyperCEST response. Moving the Arg further away from the CB6 (2i, 2j) incrementally increases the hyperCEST response of the rotaxanes. Measurements were conducted at 50 μM rotaxane in phosphate buffer pH 7. Error bars represent standard instrumental error for n=4.

Taken together, these results suggest that the change in hyperCEST response results from two independent factors: residual interactions of xenon with CB6 rotaxanes, and the ability of the CB6 to release from the rotaxane axle. This indicates that the nature of the CEST response will be dependent on the specific sequences and proteolytic cleavages under study. Nonetheless, the structural sensitivity suggests that CB6 rotaxane probes can be developed for a wide range of protease-peptide combinations.

6.4.2 Proteases activate CB6 rotaxanes for hyperCEST NMR.

Rotaxane 2e was synthesized to contain a chymotrypsin (Chy) recognition motif. Chy selectively cleaves after Tyr residues, removing the branched nature of the substrate (6.10). After the rotaxane was cleaved by Chy, a significant CEST effect was observed (6.10 c), indicating that CB6 became much more accessible for ^{129}Xe@CB6 interactions after proteolysis. Thus, even when the post-cleavage product contains bulky C-terminal residues on the rotaxane axle, proteases can still be detected using CB6 rotaxane probes.

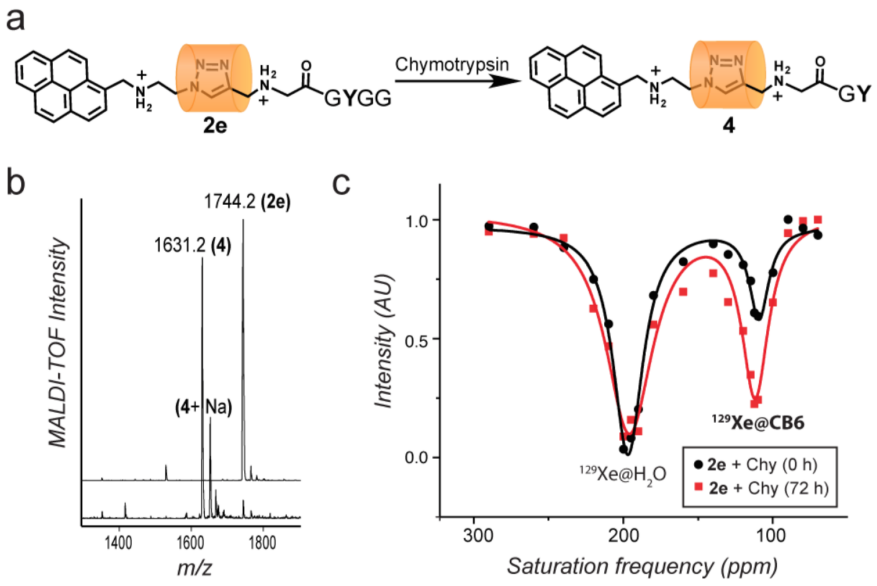

Figure 6.10: (a) Rotaxane 2e contains a GYG chymotrypsin recognition motif. Rotaxane 2e (50 μM) was incubated with chymotrypsin (5 nM) to cleave the rotaxane after the Tyr residue. (b) The reaction was monitored by MALDI-TOF MS and cleavage product 4 was confirmed after 72 h of incubation. (c) ^{129}Xe hyperCEST spectra of 2e (50 μM) immediately after addition of chymotrypsin (black), and after 72 h incubation (red). During this time, the ^{129}Xe hyperCEST response increased substantially.

To expand our rotaxane probes to address disease-related targets, rotaxane 3 (6.11 a) was synthesized containing the PLG-LAG recognition sequence of matrix metalloprotease-2 (MMP-2), which is overexpressed in a wide range of metastatic tumors [106] [112] [113], and is present in heart tissue after myocardial infarction [114]. MMP-2 has been used successfully as a target for a variety of drug delivery and imaging applications [106] [108] [112] [113]. Previously, a xenon sensor for MMP was developed with a peptide recognition sequence for MMP-7 covalently attached to CryA [52]. Upon cleavage by MMP-7, a change of approximately 0.5 ppm in the ^{129}Xe@CryA chemical shift was observed. In contrast, rotaxane 3 can detect MMP-2 by measuring the CEST effect increase between uncleaved and cleaved rotaxanes. This could allow better detection in biologically complex environments. Rotaxane 3 (100 μM) was incubated at 37 C with MMP-2 (100 nM) and monitored by HPLC and MS. Approximately 60% cleavage of 3 was observed after 24 h by HPLC (6.11 b), and post-cleavage products 2e and 5 were observed by MALDI-TOF MS (6.11 c), confirming the PLG-LAG cleavage by MMP-2.

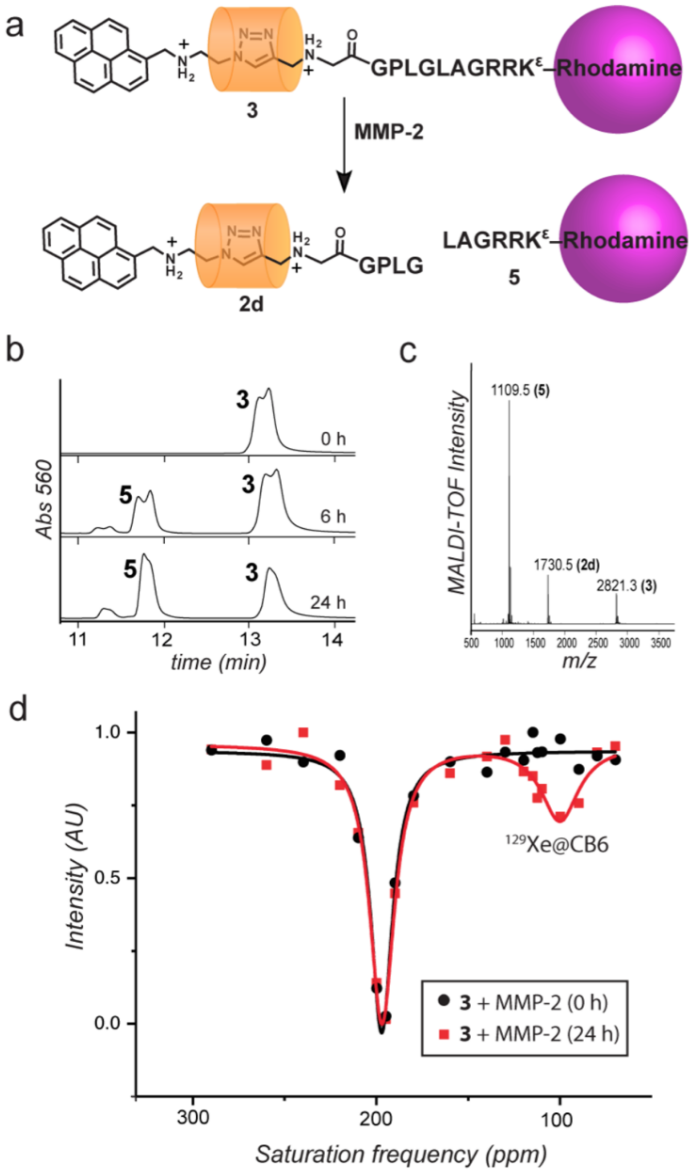

Figure 6.11: (a) Rotaxane 3 contains the PLG-LAG MMP-2 recognition sequence. Upon cleavage by MMP-2, CB6 is available for ^{129}Xe host-guest chemistry. (b) HPLC traces of 100 μM 3 (13 min) when exposed to 100 nM MMP-2 at 37 C. Approxmiately 60% cleavage to 5 (11.7 min) was observed by 24 h. Further degradation (11.3 min) was also observed. Double peaks were visible for both 3 and peptide S1 intermediate and are likely due to the 5,6 isomers of the rhodamine. (c) MALDI-TOF MS of rotaxane 3 incubated with MMP-2 for 3 h. Both cleavage products 5 and 2d were observed, as well as remaining rotaxane 3. (d) Rotaxane 3 (100 μM) was incubated with MMP-2 (100 nM) for 24 h at 37 C, and was diluted to 5 μM in ddH_2O before acquiring a hyperCEST spectrum. No detectable hyperCEST response was observed for 3 with MMP-2 immediately after incubation. After 24 h, a significant ^{129}Xe hyperCEST response was observed.

Rotaxane 3 cleavage by MMP-2 corresponded with an increase in hyperCEST response at 24 h (6.11 d). Before hyperCEST spectra were obtained, the rotaxane-enzyme solution was diluted to 5 μM rotaxane and 5 nM enzyme, where no background signal is detected from fully intact rotaxane 3 (6.3 c). After cleavage by MMP-2, xenon was able to interact strongly with CB6, producing a significant increase in hyperCEST response and allowing sensitive detection of MMP-2 with a ^{129}Xe hyperCEST probe.

6.5 Discussion

These results demonstrate that CB6 rotaxanes can be used as modular probes for protease detection. By tailoring the peptide axle to a protease of interest, these rotaxanes can be tuned for a wide range of disease detection applications. While certain amino acid sequences can have significant effects on the CEST response of these rotaxane probes, we demonstrated the flexibility in this design strategy by detecting two different proteases, and we elucidated key parameters that are important in the future design and optimization of these probes. Future work to interpret temperature and concentration dependence on the observed CEST effect of CB6 rotaxanes will help understand the mechanism of Xe@CB6 interactions and hyperCEST response. These studies will allow us to reach the nM concentration range for CB6 detection in biologically complex environments, and will help expand CB6 rotaxane probes for a wide range of disease detection applications.

Chapter 7

Non-Disruptive Dissolution of Hp-^{129}Xe into Viscous Aqueous and Organic Liquid Crystalline Environments

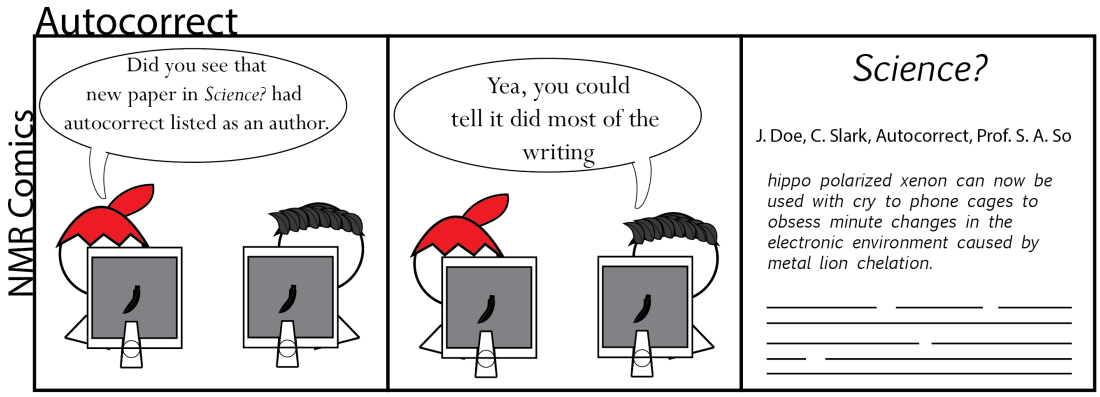

This chapter was previously published in Ref. [109] and is republished here, with minor changes and additional information, with permission.

7.1 Abstract

Studies of hyperpolarized xenon-129 (hp-^{129}Xe) in media such as liquid crystals and cell suspensions are in demand for applications from biomedical imaging to materials engineering but have been hindered by the inability to bubble xenon into them due to viscosity or perturbations caused by bubbles. We report a device that successfully and reliably dissolves hp-^{129}Xe into viscous aqueous and organic samples without bubbling. This method is robust, requires small sample volumes (60 μL), is compatible with existing NMR hardware and made

from readily-available materials. Experiments show the introduction of xenon into viscous and aligned media without disrupting molecular order. We detected dissolved xenon in an aqueous liquid crystal that is disrupted by the shear forces of bubbling, and we observed liquid-crystal phase transitions in MBBA. This tool allows an entirely new class of samples to be investigated by hyperpolarized-gas NMR.

7.2 Introduction

Hyperpolarized (hp-)^{129}Xe has proven to be an effective reporter for many biological and chemical systems, including in vivo medical imaging [55] [115] [116] [117]. Xenon NMR is also useful in material science as a highly sensitive, inert probe for properties of liquid crystal (LC) phases, nanochannels and porous structures, and as a real-time reporter for the progress of chemical processes [118] [119] [110] [120] [121] [122]. Anisotropic chemical environments such as LC phases can cause substantial shielding anisotropy in the xenon chemical shift tensor [123]. This is due to deformation of xenons electron cloud caused by the ordering of molecules near it. In an isotropic environment, unrestricted molecular tumbling averages this contribution to zero. When molecular motion is constrained by electrostatic, steric, or other non-covalent interactions in an ordered phase, an anisotropic contribution, proportional to the degree of LC order, adds to the observed ^{129}Xe chemical shift. For thermotropic LCs like N-(4-methoxybenzylidene)-4- butylaniline (MBBA), the degree of positional ordering and angle of the director axis with respect to the external field can be deduced from the xenon chemical shift anisotropy via variable temperature studies [118].

In addition to materials applications, the ability to study LC phases via hp-^{129}Xe NMR will be advantageous for biosensing. Hp-^{129}Xe has proven effective for detection and analysis of a growing number of biological samples, including gas vesicles, bacterial spores, bacteriophage, proteins, and cells [50] [124] [110] [125] [92] [126]. Biological processes, such as enzymatic cleavage and protein complex formation, have also been monitored by xenon NMR [49] [52] [74] [29]. In a number of these studies, hp-^{129}Xe associated with targeted cryptophane conjugates has modest changes in chemical shift upon binding to biological targets. The introduction of orientation-dependent interactions in an ordered environment is expected to enhance the shift change associated with xenon binding events. Increasing the separation of bound and unbound sensor resonances will allow better contrast, and faster, more sensitive biosensing.

NMR studies with hp-^{129}Xe require rapid delivery to avoid loss of signal through relaxation before detection. Hp-^{129}Xe has usually been introduced into samples through bubbling or shaking of Xe gas mixtures with the solution of interest, but these approaches are incompatible with viscous and/or easily damaged solutions such as liquid crystals or cell suspensions [50] [124] [110] [125] [92] [126] [52] [74] [29] [127]. An alternate approach has been to flow the solution of interest around Xe permeable membrane tubes pressurized externally with hp-^{129}Xe, then into the NMR probe, e.g. over alginate beads containing cells.[6] This family of setups relies on the ability to pre-dissolve hp-^{129}Xe into a flowing transport medium that is later added to a sample of interest in the magnet [128] [129] [17] [130] [131]. Unfortunately,

this approach is also incompatible with highly viscous or shear sensitive solutions.

By contrast, the dissolution of xenon into stationary liquids has been accomplished two ways: first, by pressurization with thermally polarized (TP-), isotopically-enriched, pure xenon sources [123] [49] [132] [133], and second, by using porous polypropylene hollow membrane fibers [121] [134]. Until now, the only way to visualize viscous media by ^{129}Xe NMR was via TP-xenon pressurization, which is costly and often time-consuming compared to hp-^{129}Xe experiments. In the latter case, the solutions studied were neither viscous nor sensitive to agitation. We have also noted that polypropylene hollow fibers tend to rupture and break easily compared to silicone, often leading to the generation or trapping of bubbles in viscous samples.

7.3 Methods

To enable hp-^{129}Xe studies of viscous, ordered or otherwise mechanically sensitive solutions we developed a new method for direct dissolution of hp-^{129}Xe into any solution via a silicone gas- exchange membranes, in situ in the NMR spectrometer. This approach is compatible with existing NMR probes. The membrane device, 4 mm in diameter, fits into a standard 5 mm NMR tube and requires less than 60 μL of sample. Samples are recoverable and no loss of performance was observed after repeated introduction and removal of samples.

A schematic of the assembled setup is shown in 7.1. The sample is injected by syringe through a polyimide fluid inlet tube and into the membranes via a plastic flow director cap.

Compared to previous xenon dissolution work, the positions of the hp-^{129}Xe gas and sample are reversed in our assembly: where other devices had xenon flowing from the inner volume of hollow fiber membranes to a surrounding sample liquid, we elected to place the sample inside the hollow fibers surrounded by hp-^{129}Xe gas [128] [129] [17] [130] [131] [121] [134]. By placing the sample inside the membranes and selectively exciting the dissolved xenon resonance, we utilize our pool of hyperpolarized xenon gas more efficiently compared to previous membrane-based dissolution setups while also requiring significantly less sample compared to typical bubbling experiments.

^{129}Xe spectra acquired using this system confirm the dissolution of xenon inside isotropic and ordered nematic solutions. The organic LC in this study was MBBA, which is uniaxial and thermotropic. Weakly aligning, uniaxial pf1 bacteriophage was studied as an example of an aqueous LC medium. Variable temperature studies of MBBA, and variable concentration studies of pf1 phage solutions were done with ^{2}H and ^{129}Xe NMR to confirm ordering and to demonstrate the utility of our approach for introducing hp-Xe into previously inaccessible systems.

We used both aqueous and organic liquid crystals to serve as examples of viscous and aligned media, demonstrating the broad applicability of the device. Pf1 bacteriophage and MBBA were used as model samples because neither can be probed by hp-^{129}Xe using bubbling or shake-and-bake experiments (which consist of pressurizing then physically agitating the sample to encourage mixing of the gas and solution). Both MBBA and pf1 are too viscous for bubbling to effectively dissolve xenon in a 5 mm tube. Shake-and-bake experiments

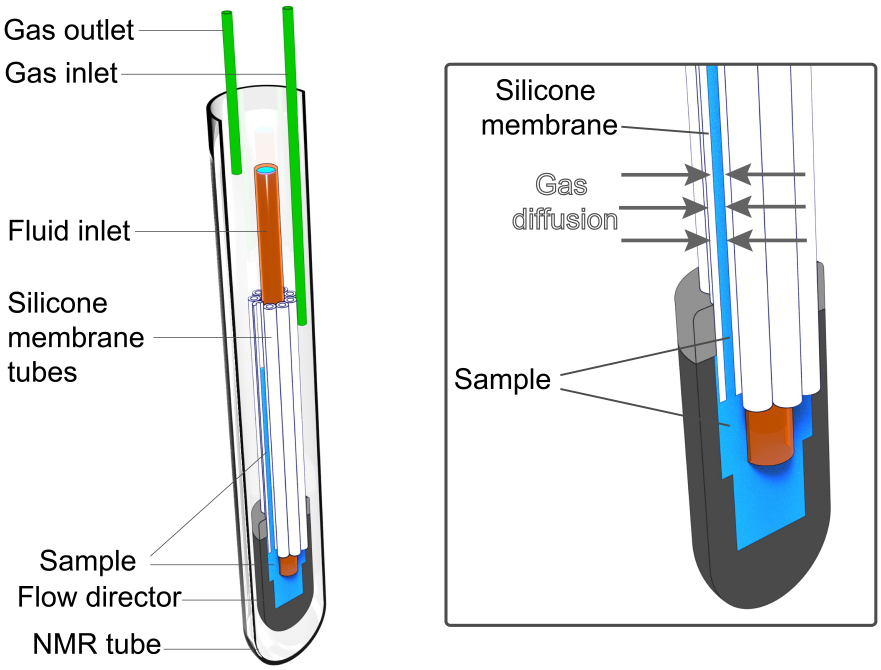

Figure 7.1: Membrane device,with cut-away, showing internal design of membrane fibers and the flow director. The sample (blue) is injected into the central polyimide fluid inlet tube (orange) and into the membranes via the flow director, which caps the bottom of the prototype. Xenon gas is introduced into and removed from the surrounding space through the gas inlet and outlet capillaries (green).

fail because of poor mixing, and long times required to reestablish macroscopic order after mixing. Pf1 further serves as a model for relatively fragile biological samples, since shear forces caused by shaking or bubbling can damage it [135]. Since pf1s ability to form ordered phases relies on its structure being intact, the observation of unperturbed molecular ordering by pf1 indicates that this setup should be useful to study other delicate samples, such as living cells.

Molecular ordering was monitored by ^{2}H NMR. Deuterium, a spin-1 nucleus, has a quadrupole moment and yields a distinct peak splitting in aligned media. Observation of ^{2}H splittings confirmed that alignment was maintained in both MBBA and pf1 during the introduction of xenon.

7.4 Results and Discussion

A peak corresponding to xenon inside the walls of the silicone membranes consistently appeared around 195 ppm (7.2, 7.3). The xenon-in-silicone peak moved an average 0.28 ppm/^{o}C upfield for aqueous samples and 0.23 ppm/^{o}C upfield for organic samples. This linear, upfield trend has also been observed for xenon adsorbed in polydimethylsiloxane

(PDMS) [136]. Dissolution of hyperpolarized xenon in aqueous and organic liquids of both low and high viscosity inside the membranes occurred in less than a minute, as monitored by the time evolution of the dissolved xenon peaks in arrayed single-shot spectra.

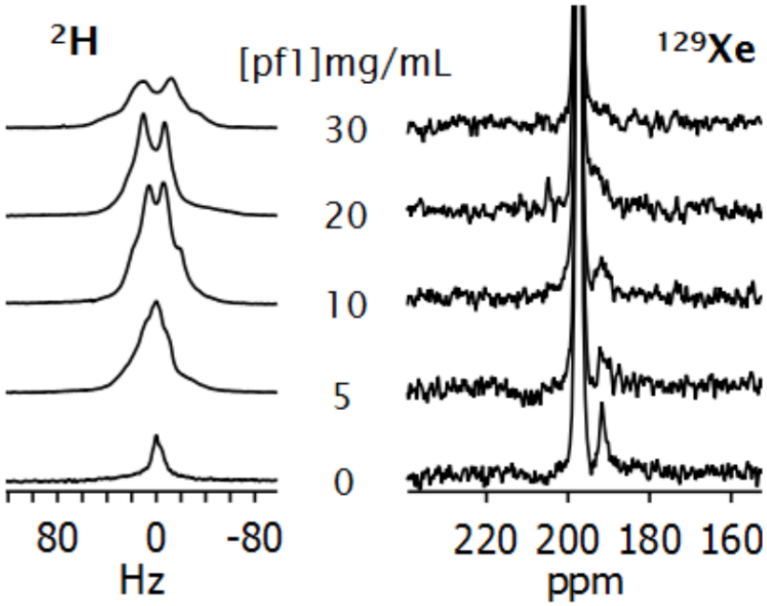

Figure 7.2: ^{2}H and ^{129}Xe spectra of 10% $^{2}H_2O$ in 0-30 mg/mL pf1 phage. ^{2}H quadrupolar splitting indicates increasing ordering of $^{2}H_2O$ molecules as phage concentration increases. The dissolved ^{129}Xe peak at 191 ppm broadens and coalesces with the silicone peak as phage concentrations increase.

The aqueous dissolved xenon peak was near 191 ppm (7.2), consistent with the value from bubbling xenon directly into solution. Viscous aqueous samples of pf1 bacteriophage provided weaker signals than the MBBA due in part to the lower solubility of xenon in water [137]. Nevertheless, the increase in ^{2}H quadrupolar splittings from $^{2}H_2O$, reflecting increased order of the $^{2}H_2O$ [9] with increasing concentrations of phage, (7.2, left) demonstrate that the ordering remains unperturbed inside the membranes. Recent theoretical work supports that the order we observe inside the membranes is due to external field-induced alignment and not wall interactions [138]. Drawing from a study that applied thermally polarized xenon to an aqueous, lyotropic LC, we believe the significant broadening of the ^{2}H resonances with increasing phage concentration may reflect a collapse of the liquid crystal phase [133].

MBBA has a well-characterized nematic-to-isotropic phase transition [139] [140] [141], with the temperature at which this phase transition occurs heavily dependent on the identity and amount of solute dissolved in the MBBA [142]. The 2H spectra (7.3 top) show quadrupolar splittings of benzene-d6 at low temperatures but disappear between 35^{o}C and 40^{o}C, demonstrating a loss of order. This interval is consistent with previous work on similar

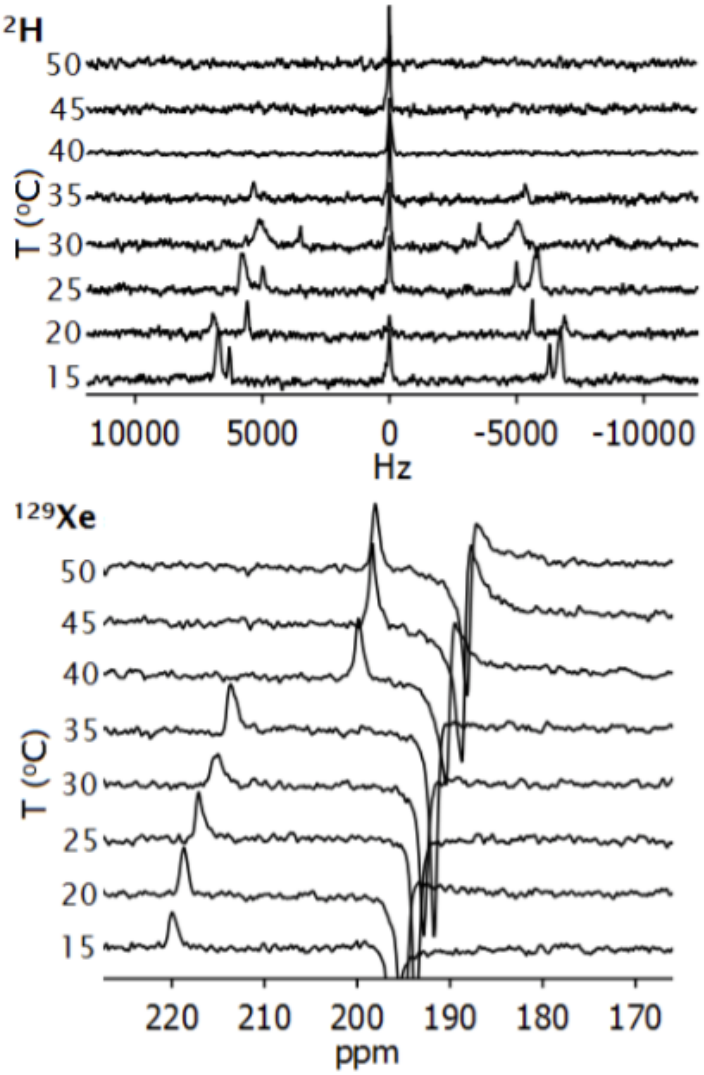

Figure 7.3: 2H (top) and ^{129}Xe (bottom) spectra of 3% benzene-d6 in MBBA samples inside the membrane assembly over a range of temperatures. The dissolved Xe peak appears at 200-220 ppm. The xenon-in-silicone peak at 190-196 ppm is not phase corrected for better resolution between it and the dissolved xenon peak and is likely negatively phased due to residual suppressed signal. ^{2}H quadrupolar splitting indicates a transition from an anisotropic to an isotropic phase between 35 and 40 ^{o}C, in good agreement with the jump in ^{129}Xe chemical shift of 13 ppm for the same temperature range.

samples [142].

^{129}Xe is spin-1/2 and, therefore, does not have a quadrupole moment, but the chemical shift is sensitive to phase transitions in ordered media. A linear variation in the xenon-in-MBBA chemical shift occurs due to the increasing temperature, with an abrupt 12.4 ppm

jump in the 35^{o}C to 40^{o}C interval (7.3, bottom). This marked increase in shielding indicates a positive anisotropy of diamagnetic susceptibility, a known quality of MBBA [143], and a common characteristic of liquid crystals whose director axes are parallel to the external field.

Both MBBA and pf1 bacteriophage are highly viscous samples into which xenon gas cannot be introduced by bubbling or shaking methods, previously precluding hyperpolarized gas experiments. With our device, it is now possible to obtain high quality hyperpolarized xenon spectra of these viscous solutions, or others prone to damage by agitation, in a moderate time without the requirement of isotopically enriched xenon sources, liquid flow, or shaking.

We have developed the first robust method for dissolving hp- ^{129}Xe directly into viscous liquids without bubbling, enabling completely new types of hyperpolarized gas studies. Proof-of- concept experiments demonstrated the quantitative abilities of this method in both aqueous and organic solutions, specifically in the detection of the nematic-isotropic phase transition of a thermotropic liquid crystal. These results mark the potential for new studies of hp-^{129}Xe in viscous and other anisotropic media, including those with cells, protein solutions, liquid crystals and polymers. This system also allows direct introduction of other gases into the sample, including oxygen and carbon dioxide for cell suspensions.

7.5 Conclusions

The ability to introduce hyperpolarized xenon without disturbing local orientation gives an excellent oppertunity to revist some early CryA based molecular sensors that may undergo a shape change upon target binding. The additional anisotropic component of the chemical shift could make the shift change upon binding significant enough to use for detection. Rotaxane based sensors may also prove interesting in oriented environments as they would tpyically align with the orienting environment due to their relatively linear structure and upon binding that structure can be altered.

Chapter 8

Preliminary Data for Cucurbit-7-uril Rotaxanes for "Always-On" Molecular Sensors

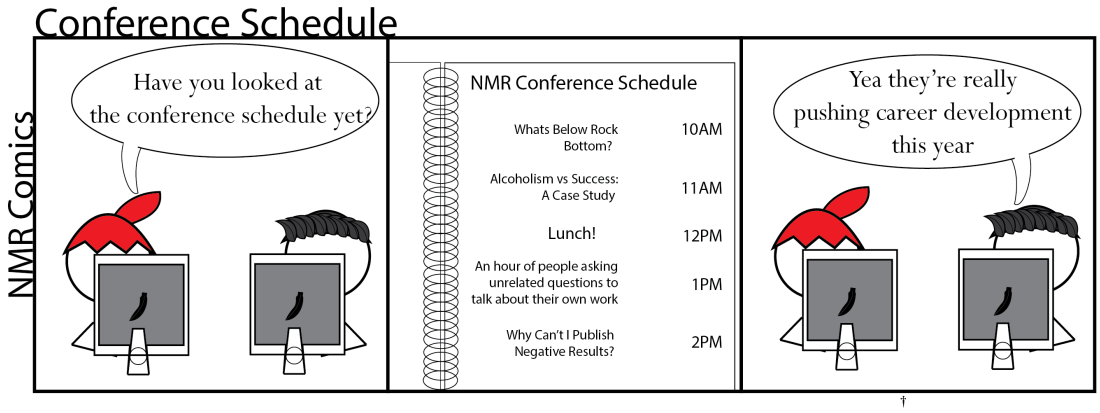

8.1 Introduction

The varied sizes of the cucurbiturils (2.2) allow for some flexibility when desiging what kind of binding pokcet you need for xenon exchange. CB7 has an internal volume of 279 $Å^3$ [3] which means that a xenon atom only occupies 15.4% of the internal space leaving plenty of room for another host molecule or another guest molecule. Cucurbits are well known for having incredibly high binding affinities for guest molecules, from 10^5 to 10^{15} M^{-1} with CB7 having the highest affinities reported [144] [145]. Xylylenediamine (XD) is a relatively non-bulky guest molecule for CB7 which still binds strongly; when in solution with CB7 and xenon we expect NMR signals from 3 unique host-guest complexes shown in 8.1.

If we use the 55% occupancy as ideal then even with two xenon atoms in a single CB7

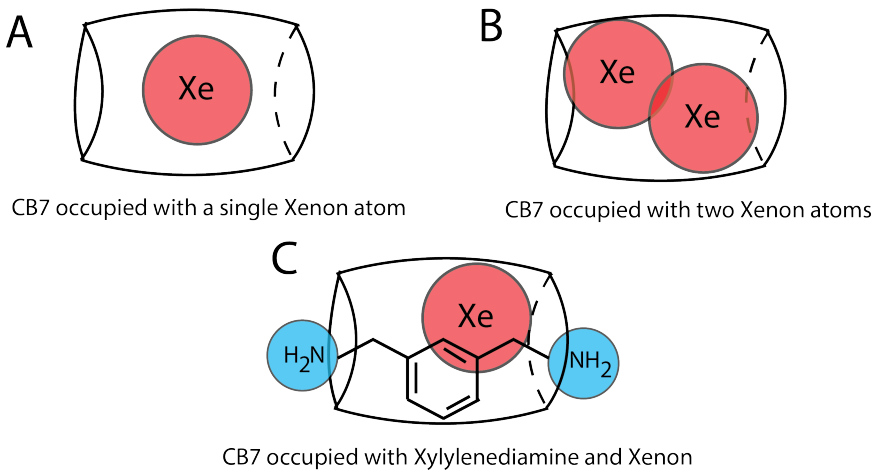

Figure 8.1:

only 30.8% of the cavity is occupied so the binding would still not be as strong a xenon in CryA (45% occupied). Approximating the van der Waals volume for the benzene ring to be about 130 $Å^3$ modeled as a cylinder using the para proton to proton distance as the diameter of the cylinder and the van der Waals diameter of carbon as the height gives CB7 a 46% occupance when hosting xylylenediamine and 61% occupancy when dual hosting Xe and XD, slightly higher than the 55% ideal. A 20 μM solution of CB7 was titrated with XD and spectra were taken at 20 ^{o}C the results are shown in 8.2.

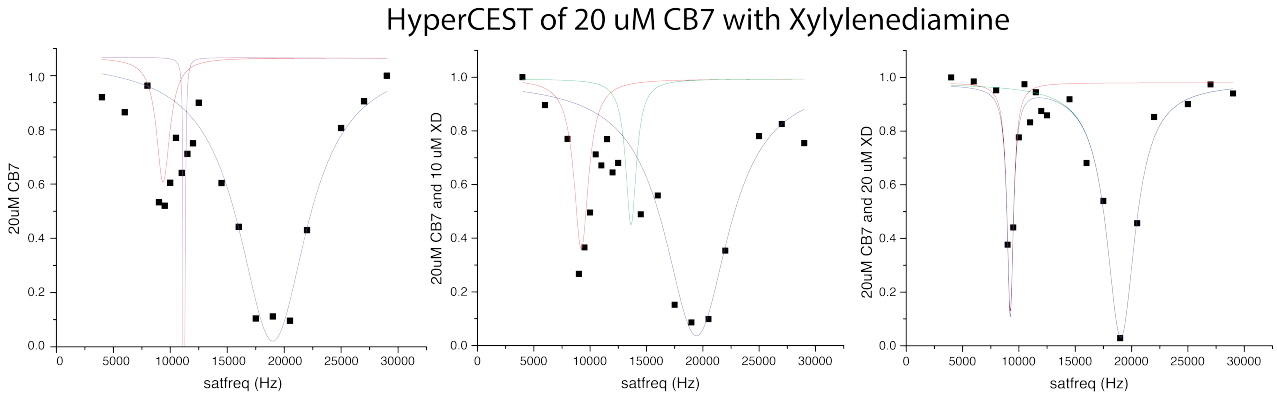

Figure 8.2: Titration of 20 μM CB7 with XD by ^{129}Xe HyperCEST at 20 ^{o}C with no XD present (left) 10 μM XD (center) and 20 μM XD (right) showing possilbe multiple host peaks.

Fitting the hyperCEST data using ORIGIN shows for the 20 μM CB7 (8.2 A) there are 3

peaks present 2 between 7500 Hz and 12500 Hz corresponding to CB7-Xenon complexes and a broad water peak centered at 19000 Hz. As there is no XD present in this first spectrum we assume the two peaks correspond to single and double hosting of Xe atoms in CB7 (8.1 A and B). For the second spectrum 20 μM CB7 and 10 μM Xd ORIGIN still recognizes 3 peaks with the reponse at 9000 Hz getting stronger and the second shifting towards the water centered around 13000 Hz. When XD is added to solution the response at 9000 Hz gets stronger and may correspond to a combination of single occupied CB7 and Xe-XD doubly occupied CB7 (8.1 A and C). When XD is added in a 1:1 ratio only the single occupied CB7 peak at 9000 Hz is observed and the water peak at 19000 Hz becomes significantly narrower (from $\approx$ 6500 to $\approx$ 4000 Hz at half max) indicating that the exchange of xenon in and out of the CB7 is slower, which we would expect in the CB7 was co-hosting a xylylenediamine molecule.

8.2 Mechanically Locked CB*n* Sensors

A CB7 rotaxane was also synthesized using a spermine linker (considerably smaller then xylylelenediamine) with fluorocene caps to prevent CB7 from coming off, and a hyperCEST spectrum was obtained shown in 8.3.

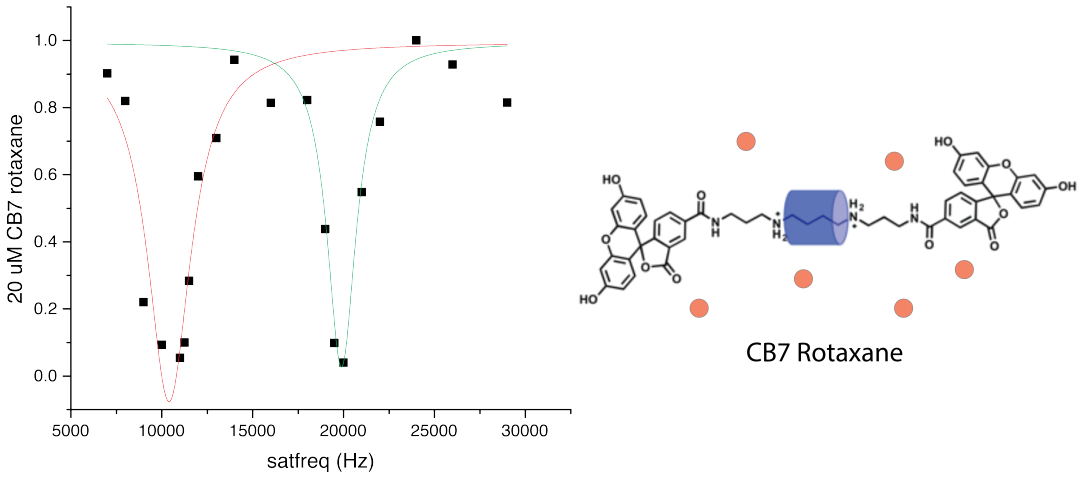

Figure 8.3: HyperCEST spectrum 20 μM CB7-rotaxane at 25 ^{o}C with a hyperCEST response at 11000 Hz and a water peak with a FWHM of 2500 Hz

The strong hyperCEST response around 11000 Hz is consistent with CB7 at 25 ^{o}C and the narrow water peak indicates that there is no free CB7 present as the exchange between the bulk water and CB7-rotaxane is slower then that for free CB7. The additional bulk of the fluorocene caps may slow xenon exchange contributing to the narrower water peak then was observed for the CB7-XD system.

Further work with CB8 rotaxanes would allow for more complex linkers to directly interact with xenon during dual hosting.

Bibliography

[1] Clever, H, ed. (1979) *Krypton, Xenon, and Radon-Gas Solubilities.* (Oxford: Pergamon Press) Vol. 2.

[2] Ladefoged, J & Andersen, A. (1967) Solubility of 133Xe at 37^{o}C in water, saline, olive oil, liquid paraffin, solutions of albumin, and blood. *Phys. Med. Biol.* **12**, 353–358.

[3] Lagona, J, Mukhopadhyay, P, Chakrabarti, S, & Isaacs, L. (2005) The cucurbit[n]uril family. *Angewandte Chemie International Edition* **44**, 4844–4870.

[4] Ntziachristos, V. (2006) Fluorescence Molecular Imaging. *Annual Review of Biomedical Engineering* **8**, 1–33.

[5] Sosnovik, D. E & Weissleder, R. (2007) Emerging concepts in molecular MRI. *Current Opinion in Biotechnology* **18**, 4–10.

[6] Gumpu, M. B, Sethuraman, S, Krishnan, U. M, & Rayappan, J. B. B. (2015) A review on detection of heavy metal ions in water - An electrochemical approach. *Sensors and Actuators, B: Chemical* **213**, 515–533.

[7] Weaver, E. M & Hummon, A. B. (2013) Imaging mass spectrometry: From tissue sections to cell cultures. *Advanced Drug Delivery Reviews* **65**, 1039–1055.

[8] Keeler, J. (2011) *Understanding NMR Spectroscopy.* (Wiley).

[9] Levitt, M. (2013) *Spin Dynamics: Basics of Nuclear Magnetic Resonance.* (Wiley).

[10] Kellogg, J. M. B, Rabi, I. I, Ramsey, N. F, & Zacharias, J. R. (1939) The magnetic moments of the proton and the deuteron. the radiofrequency spectrum of h_2 in various magnetic fields. *Phys. Rev.* **56**, 728–743.

[11] Bloch, F, Hansen, W, & Packard, M. (1946) Nuclear magnetic resonance. *Phys. Rev* **70**, 8.

[12] Walker, Thad G. (Department of Physics, University of Wisconsin-Madison, Madison, W. & Happer, William (Department of Physics, Princeton University, Princeton, N. J. . (1997) Spin-exchange optical pumping of noble-gas nuclei. *Reviews of Modern Physics* **69**, 629–642.

[13] Barnes, A. B, Corzilius, B, Mak-Jurkauskas, M. L, Andreas, L. B, Bajaj, V. S, Matsuki, Y, Belenky, M. L, Lugtenburg, J, Sirigiri, J. R, Temkin, R. J, Herzfeld, J, & Griffin, R. G. (2010) Resolution and polarization distribution in cryogenic dnp/mas experiments. *Phys. Chem. Chem. Phys.* **12**, 5861–5867.

[14] Tycko, R. (2013) Nmr at low and ultralow temperatures. *Accounts of Chemical Research* **46**, 1923–1932. PMID: 23470028.

[15] Boashash, B. (2015) *Time-frequency signal analysis and processing: a comprehensive reference*. (Academic Press).

[16] Hahn, E. L. (1950) Spin echoes. *Physical review* **80**, 580.

[17] Goodson, B. M. (2002) Nuclear magnetic resonance of laser-polarized noble gases in molecules, materials, and organisms. *Journal of Magnetic Resonance* **155**, 157 – 216.

[18] Pietrai, T & Gaede, H. C. (1995) Optically polarized 129xe in nmr spectroscopy*. *Advanced Materials* **7**, 826–838.

[19] William Ramsay, M. W. T. (1901) Argon and its companions. *Philosophical Transactions of the Royal Society of London. Series A, Containing Papers of a Mathematical or Physical Character* **197**, 47–89.

[20] Edgerton, H. E. (1956) Xenon Flash Tube of Small Size. *Review of Scientific Instruments* **27**, 821.

[21] Cullen, S. C & Gross, E. G. (1951) The anesthetic properties of xenon in animals and human beings, with additional observations on krypton. *Science* **113**, 580–582.

[22] Lauterbur, P. C. (1973) Image Formation by Induced Local Interactions: Examples Employing Nuclear Magnetic Resonance. *Nature* **242**, 190–191.

[23] Albert, M. S, Cates, G. D, Driehuys, B, Happer, W, Saam, B, Springer, C. S, & Wishnia, A. (1994) Biological magnetic resonance imaging using laser-polarized 129Xe. *Nature* **370**, 199–201.

[24] Stupic, K. F, Cleveland, Z. I, Pavlovskaya, G. E, & Meersmann, T. (2011) Hyperpolarized 131xe nmr spectroscopy. *Journal of Magnetic Resonance* **208**, 58 – 69.

[25] CRC Handbook. (2007) *CRC Handbook of Chemistry and Physics, 88th Edition*. (CRC Press), 88 edition.

[26] Seltzer, S. (2008) Ph.D. thesis (Princeton University).

[27] Fairchild, R. M, Joseph, A. I, Holman, K. T, Fogarty, H. A, Brotin, T, Dutasta, J.-P, Boutin, C, Huber, G, & Berthault, P. (2010) A water-soluble xe@cryptophane-111 complex exhibits very high thermodynamic stability and a peculiar 129xe nmr chemical shift. *Journal of the American Chemical Society* **132**, 15505–15507.

[28] Jeong, K, Slack, C. C, Vassiliou, C. C, Dao, P, Gomes, M. D, Kennedy, D. J, Truxal, A. E, Sperling, L. J, Francis, M. B, Wemmer, D. E, et al. (2015) Investigation of dota–metal chelation effects on the chemical shift of 129xe. *ChemPhysChem* **16**, 3573–3577.

[29] Finbloom, J. A, Slack, C. C, Bruns, C. J, Jeong, K, Wemmer, D. E, Pines, A, & Francis, M. B. (2016) Rotaxane-mediated suppression and activation of cucurbit[6]uril for molecular detection by 129xe hypercest nmr. *Chem. Commun.* **52**, 3119–3122.

[30] Schroder, L, Lowery, T. J, Hilty, C, Wemmer, D. E, & Pines, A. (2006) Molecular imaging using a targeted magnetic resonance hyperpolarized biosensor. *Science* **314**, 446–449. Science096MWTimes Cited:109Cited References Count:20.

[31] Mecozzi, S & Rebek, Jr., J. (1998) The 55the liquid state. *Chemistry A European Journal* **4**, 1016–1022.

[32] Collet, A, Dutasta, J.-P, Lozach, B, & Canceill, J. (1993) *Cyclotriveratrylenes and cryptophanes: Their synthesis and applications to host-guest chemistry and to the design of new materials.* (Springer Berlin Heidelberg, Berlin, Heidelberg), pp. 103–129.

[33] Aru Hill, P, Wei, Q, Troxler, T, & Dmochowski, I. J. (2009) Substituent effects on xenon binding affinity and solution behaviour of water-soluble cryptophanes. *Journal of the American Chemical Society* **131**, 3069–3077.

[34] Ruiz, M. M. S. E. J, Rubin, S. M, Lowery, T. J, Winssinger, N, Wemmer, P. G. S. D. E, & Pines, A. (2004) Development of a functionalized xenon biosensor. *Journal of the American Chemical Society* **126**, 15287–15294.

[35] Spence, M. M, Rubin, S. M, Dimitrov, I. E, Ruiz, E. J, Wemmer, D. E, Pines, A, Yao, S. Q, Tian, F, & Schultz, P. G. (2001) Functionalized xenon as a biosensor. *Proceedings of the National Academy of Sciences* **98**, 10654–10657.

[36] Brotin, T & Dutasta, J.-P. (2003) Xe@cryptophane complexes with c2 symmetry: Synthesis and investigations by 129xe nmr of the consequences of the size of the host cavity for xenon encapsulation. *European Journal of Organic Chemistry* **2003**, 973–984.

[37] Huber, G, Brotin, T, Dubois, L, Desvaux, H, Dutasta, J.-P, & Berthault, P. (2006) Water soluble cryptophanes showing unprecedented affinity for xenon: candidates as nmr-based biosensors. *Journal of the American Chemical Society* **128**, 6239–6246.

[38] Chavez, L. J. (2007) Ph.D. thesis (University of California Berkeley).

[39] Kunth, M, Witte, C, Hennig, A, & Schröder, L. (2015) Identification, classification, and signal amplification capabilities of high-turnover gas binding hosts in ultra-sensitive NMR. *Chem. Sci.* **6**, 6069–6075.

[40] Harrison, I. T & Harrison, S. (1967) Synthesis of a stable complex of a macrocycle and a threaded chain. *Journal of the American Chemical Society* **89**, 5723–5724.

[41] Shanrong Zhang, , , Matthew Merritt, , Donald E. Woessner, , Robert E. Lenkinski, , , & A. Dean Sherry*, , . (2003) Paracest agents: modulating mri contrast via water proton exchange. *Accounts of Chemical Research* **36**, 783–790. PMID: 14567712.

[42] Chan, K. W, Yu, T, Qiao, Y, Liu, Q, Yang, M, Patel, H, Liu, G, Kinzler, K. W, Vogelstein, B, Bulte, J. W, van Zijl, P. C, Hanes, J, Zhou, S, & McMahon, M. T. (2014) A diacest mri approach for monitoring liposomal accumulation in tumors. *Journal of Controlled Release* **180**, 51 – 59.

[43] McMahon, M. T, Gilad, A. A, DeLiso, M. A, Cromer Berman, S. M, Bulte, J. W, & van Zijl, P. C. (2008) New multicolor polypeptide diamagnetic chemical exchange saturation transfer (diacest) contrast agents for mri. *Magnetic Resonance in Medicine* **60**, 803–812.

[44] Fairchild, R. M, Joseph, A. I, Holman, K. T, Fogarty, H. A, Brotin, T, Dutasta, J.-P, Boutin, C, Huber, G, & Berthault, P. (2010) A water-soluble xe@ cryptophane-111 complex exhibits very high thermodynamic stability and a peculiar 129xe nmr chemical shift. *Journal of the American Chemical Society* **132**, 15505–15507.

[45] Quang, D. T & Kim, J. S. (2010) Fluoro- and chromogenic chemodosimeters for heavy metal ion detection in solution and biospecimens. *Chemical Reviews* **110**, 6280–6301.

[46] (1980) The replacement of the nondescript term heavy metals by a biologically and chemically significant classification of metal ions. *Environmental Pollution Series B, Chemical and Physical* **1**, 3 – 26.

[47] Oros, A. M & Shah, N. J. (2004) Hyperpolarized xenon in nmr and mri. *Physics in medicine and biology* **49**, R105.

[48] Mazzanti, M. L, Walvick, R. P, Zhou, X, Sun, Y, Shah, N, Mansour, J, Gereige, J, & Albert, M. S. (2011) Distribution of hyperpolarized xenon in the brain following sensory stimulation: Preliminary mri findings. *PLoS ONE* **6**, 1–7.

[49] Schlundt, A, Kilian, W, Beyermann, M, Sticht, J, Gnther, S, Hpner, S, Falk, K, Roetzschke, O, Mitschang, L, & Freund, C. (2009) A xenon-129 biosensor for monitoring mhcpeptide interactions. *Angewandte Chemie* **121**, 4206–4209.

[50] Lowery, T. J, Garcia, S, Chavez, L, Ruiz, E. J, Wu, T, Brotin, T, Dutasta, J.-P, King, D. S, Schultz, P. G, Pines, A, & Wemmer, D. E. (2006) Optimization of xenon biosensors for detection of protein interactions. *ChemBioChem* **7**, 65–73.

[51] Spence, M. M, Ruiz, E. J, Rubin, S. M, Lowery, T. J, Winssinger, N, Schultz, P. G, Wemmer, D. E, & Pines, A. (2004) Development of a functionalized xenon biosensor. *Journal of the American Chemical Society* **126**, 15287–15294. J Am Chem Soc.

[52] Wei, Q, Seward, G. K, Hill, P. A, Patton, B, Dimitrov, I. E, Kuzma, N. N, & Dmochowski, I. J. (2006) Designing 129xe nmr biosensors for matrix metalloproteinase detection. *Journal of the American Chemical Society* **128**, 13274–13283.

[53] Roy, V, Brotin, T, Dutasta, J.-P, Charles, M.-H, Delair, T, Mallet, F, Huber, G, Desvaux, H, Boulard, Y, & Berthault, P. (2007) A cryptophane biosensor for the detection of specific nucleotide targets through xenon nmr spectroscopy. *ChemPhysChem* **8**, 2082–2085.

[54] Schröder, L, Lowery, T. J, Hilty, C, Wemmer, D. E, & Pines, A. (2006) Molecular imaging using a targeted magnetic resonance hyperpolarized biosensor. *Science* **314**, 446–449.

[55] Schröder, L. (2013) Xenon for nmr biosensing inert but alert. *Physica Medica* **29**.

[56] Zhang, J, Jiang, W, Luo, Q, Zhang, X, Guo, Q, Liu, M, & Zhou, X. (2014) Rational design of hyperpolarized xenon nmr molecular sensor for the selective and sensitive determination of zinc ions. *Talanta* **122**, 101–105.

[57] Kotera, N, Tassali, N, Lonce, E, Boutin, C, Berthault, P, Brotin, T, Dutasta, J.-P, Delacour, L, Traor, T, Buisson, D.-A, Taran, F, Coudert, S, & Rousseau, B. (2012) A sensitive zinc-activated 129xe mri probe. *Angewandte Chemie* **124**, 4176–4179.

[58] Tassali, N, Kotera, N, Boutin, C, Léonce, E, Boulard, Y, Rousseau, B, Dubost, E, Taran, F, Brotin, T, Dutasta, J.-P, et al. (2014) Smart detection of toxic metal ions, pb2+ and cd2+, using a 129xe nmr-based sensor. *Analytical chemistry* **86**, 1783–1788.

[59] Viola-Villegas, N & Doyle, R. P. (2009) The coordination chemistry of 1,4,7,10-tetraazacyclododecane-n,n,n,n-tetraacetic acid (h4dota): Structural overview and analyses on structurestability relationships. *Coordination Chemistry Reviews* **253**, 1906 – 1925.

[60] Palaniappan, K. K, Ramirez, R, Bajaj, V, Wemmer, D, Pines, A, & Francis, M. (2013) Molecular imaging of cancer cells using a bacteriophage-based (129) xe nmr biosensor. *Angewandte Chemie-International Edition* **52**, 4849–4853.

[61] Witte, C & Schröder, L. (2013) Nmr of hyperpolarised probes. *NMR in Biomedicine* **26**, 788–802.

[62] Sears, D. N & Jameson, C. J. (2003) Theoretical calculations of the xe chemical shifts in cryptophane cages. *The Journal of chemical physics* **119**, 12231–12244.

[63] Ruiz, E. J, Sears, D. N, Pines, A, & Jameson, C. J. (2006) Diastereomeric xe chemical shifts in tethered cryptophane cages. *Journal of the American Chemical Society* **128**, 16980–16988.

[64] Ruset, I. C, Ketel, S, & Hersman, F. W. (2006) Optical pumping system design for large production of hyperpolarized ^{129}Xe. *Phys. Rev. Lett.* **96**, 053002.

[65] Nikolaou, P, Coffey, A. M, Walkup, L. L, Gust, B. M, Whiting, N, Newton, H, Barcus, S, Muradyan, I, Dabaghyan, M, Moroz, G. D, Rosen, M. S, Patz, S, Barlow, M. J, Chekmenev, E. Y, & Goodson, B. M. (2013) Near-unity nuclear polarization with an open-source 129Xe hyperpolarizer for NMR and MRI. *Proceedings of the National Academy of Sciences of the United States of America* **110**, 14150–5.

[66] Driehuys, B, Pollaro, J, & Cofer, G. P. (2008) In vivo mri using real-time production of hyperpolarized 129xe. *Magnetic Resonance in Medicine* **60**, 14–20.

[67] Gomes, M. D, Dao, P, Jeong, K, Slack, C. C, Vassiliou, C. C, Finbloom, J. A, Francis, M. B, Wemmer, D. E, & Pines, A. (0) 129xe nmr relaxation-based macromolecular sensing. *Journal of the American Chemical Society* **0**, null. PMID: 27472048.

[68] Kunth, M, Witte, C, & Schrder, L. (2015) Continuous-wave saturation considerations for efficient xenon depolarization. *NMR in Biomedicine* **28**, 601–606.

[69] Witte, C, Martos, V, Rose, H. M, Reinke, S, Klippel, S, Schrder, L, & Hackenberger, C. P. R. (2015) Live-cell mri with xenon hyper-cest biosensors targeted to metabolically labeled cell-surface glycans. *Angewandte Chemie International Edition* **54**, 2806–2810.

[70] Khan, N. S, Riggle, B. A, Seward, G. K, Bai, Y, & Dmochowski, I. J. (2014) Cryptophane-folate biosensor for 129xe nmr. *Bioconjugate chemistry* **26**, 101–109.

[71] Riggle, B. A, Wang, Y, & Dmochowski, I. J. (2015) A "Smart" 129Xe NMR biosensor for pH-dependent cell labeling. *Journal of the American Chemical Society* **137**, 5542–5548.

[72] Qing, K, Ruppert, K, Jiang, Y, Mata, J. F, Miller, G. W, Shim, Y. M, Wang, C, Ruset, I. C, Hersman, F. W, Altes, T. A, & Mugler, J. P. (2014) Regional mapping of gas uptake by blood and tissue in the human lung using hyperpolarized xenon-129 mri. *Journal of Magnetic Resonance Imaging* **39**, 346–359.

[73] Zamberlan, F, Lesbats, C, Rogers, N. J, Krupa, J. L, Pavlovskaya, G. E, Thomas, N. R, Faas, H. M, & Meersmann, T. (2015) Back cover: Molecular sensing with hyperpolarized 129xe using switchable chemical exchange relaxation transfer (chemphyschem 11/2015). *ChemPhysChem* **16**, 2476–2476.

[74] Stevens, T. K, Palaniappan, K. K, Ramirez, R. M, Francis, M. B, Wemmer, D. E, & Pines, A. (2013) Hypercest detection of a 129xe-based contrast agent composed of cryptophane-a molecular cages on a bacteriophage scaffold. *Magnetic Resonance in Medicine* **69**, 1245–1252.

[75] Wang, Y & Dmochowski, I. J. (2015) Cucurbit[6]uril is an ultrasensitive 129xe nmr contrast agent. *Chem. Commun.* **51**, 8982–8985.

[76] Meldrum, T, Seim, K. L, Bajaj, V. S, Palaniappan, K. K, Wu, W, Francis, M. B, Wemmer, D. E, & Pines, A. (2010) A xenon-based molecular sensor assembled on an ms2 viral capsid scaffold. *Journal of the American Chemical Society* **132**, 5936–5937.

[77] Garimella, P. D, Meldrum, T, Witus, L. S, Smith, M, Bajaj, V. S, Wemmer, D. E, Francis, M. B, & Pines, A. (2013) Hyperpolarized xenon-based molecular sensors for label-free detection of analytes. *Journal of the American Chemical Society* **136**, 164–168.

[78] Hall, L. D, Evans, S. D, & Nott, K. P. (1998) Measurement of textural changes of food by mri relaxometry. *Magnetic resonance imaging* **16**, 485–492.

[79] Jaeger, F, Bowe, S, Van As, H, & Schaumann, G. E. (2009) Evaluation of ^{1}h nmr relaxometry for the assessment of pore-size distribution in soil samples. *European Journal of Soil Science* **60**, 1052–1064.

[80] Wen, Y & Kantzas, A. (2005) Monitoring bitumen-solvent interactions with low-field nuclear magnetic resonance and x-ray computer-assisted tomography. *Energy & fuels* **19**, 1319–1326.

[81] Look, D. C & Locker, D. R. (1970) Time saving in measurement of nmr and epr relaxation times. *Review of Scientific Instruments* **41**, 250–251.

[82] Rubin, S. M, Spence, M. M, Pines, A, & Wemmer, D. E. (2001) Characterization of the effects of nonspecific xenon–protein interactions on 129 xe chemical shifts in aqueous solution: Further development of xenon as a biomolecular probe. *Journal of Magnetic Resonance* **152**, 79–86.

[83] Baldwin, A. J. (2014) An exact solution for r 2, eff in cpmg experiments in the case of two site chemical exchange. *Journal of Magnetic Resonance* **244**, 114–124.

[84] Gore, J. C & Anderson, A. W. (2007) *The Physics of Relaxation*. (John Wiley & Sons, Ltd).

[85] Shen, C & New, E. J. (2013) Promising strategies for gd-based responsive magnetic resonance imaging contrast agents. *Current opinion in chemical biology* **17**, 158–166.

[86] Major, J. L & Meade, T. J. (2009) Bioresponsive, cell-penetrating, and multimeric mr contrast agents. *Accounts of chemical research* **42**, 893–903.

[87] Lee, N, Choi, S. H, & Hyeon, T. (2013) Nano-sized ct contrast agents. *Advanced Materials* **25**, 2641–2660.

[88] Que, E. L, New, E. J, & Chang, C. J. (2012) A cell-permeable gadolinium contrast agent for magnetic resonance imaging of copper in a menkes disease model. *Chem. Sci.* **3**, 1829–1834.

[89] Liu, G, Li, Y, & Pagel, M. D. (2007) Design and characterization of a new irreversible responsive paracest mri contrast agent that detects nitric oxide. *Magnetic Resonance in Medicine* **58**, 1249–1256.

[90] Lippert, A. R, Keshari, K. R, Kurhanewicz, J, & Chang, C. J. (2011) A hydrogen peroxide-responsive hyperpolarized 13c mri contrast agent. *Journal of the American Chemical Society* **133**, 3776–3779.

[91] Oros, A.-M & Shah, N. J. (2004) Hyperpolarized xenon in nmr and mri. *Physics in medicine and biology* **49**, R105.

[92] Shapiro, M. G, Ramirez, R. M, Sperling, L. J, Sun, G, Sun, J, Pines, A, Schaffer, D. V, & Bajaj, V. S. (2014) Genetically encoded reporters for hyperpolarized xenon magnetic resonance imaging. *Nature chemistry* **6**, 629–634.

[93] Rose, H. M, Witte, C, Rossella, F, Klippel, S, Freund, C, & Schröder, L. (2014) Development of an antibody-based, modular biosensor for 129xe nmr molecular imaging of cells at nanomolar concentrations. *Proceedings of the National Academy of Sciences* **111**, 11697–11702.

[94] Witte, C, Martos, V, Rose, H. M, Reinke, S, Klippel, S, Schröder, L, & Hackenberger, C. P. (2015) Live-cell mri with xenon hyper-cest biosensors targeted to metabolically labeled cell-surface glycans. *Angewandte Chemie International Edition* **54**, 2806–2810.

[95] Ayhan, M. M, Karoui, H, Hardy, M, Rockenbauer, A, Charles, L, Rosas, R, Udachin, K, Tordo, P, Bardelang, D, & Ouari, O. (2015) Comprehensive synthesis of monohydroxycucurbit[n]urils (n = 5, 6, 7, 8): High purity and high conversions. *Journal of the American Chemical Society* **137**, 10238–10245.

[96] Masson, E, Ling, X, Joseph, R, Kyeremeh-Mensah, L, & Lu, X. (2012) Cucurbituril chemistry: a tale of supramolecular success. *RSC Adv.* **2**, 1213–1247.

[97] Márquez, C, Hudgins, R. R, & Nau, W. M. (2004) Mechanism of host-guest complexation by cucurbituril. *Journal of the American Chemical Society* **126**, 5806–5816.

[98] Schnurr, M, Sloniec-Myszk, J, Döpfert, J, Schröder, L, & Hennig, A. (2015) Supramolecular assays for mapping enzyme activity by displacement-triggered change in hyperpolarized 129xe magnetization transfer nmr spectroscopy. *Angewandte Chemie International Edition* **54**, 13444–13447.

[99] Mock, W. L, Irra, T. A, Wepsiec, J. P, & Adhya, M. (1989) Catalysis by cucurbituril. the significance of bound-substrate destabilization for induced triazole formation. *The Journal of Organic Chemistry* **54**, 5302–5308.

[100] Tuncel, D & Steinke, J. H. G. (2002) The synthesis of [2], [3] and [4]rotaxanes and semirotaxanes. *Chem. Commun.* pp. 496–497.

[101] Ke, C, Smaldone, R. A, Kikuchi, T, Li, H, Davis, A. P, & Stoddart, J. F. (2013) Quantitative emergence of hetero [4] rotaxanes by template-directed click chemistry. *Angewandte Chemie International Edition* **52**, 381–387.

[102] Angelos, S, Yang, Y.-W, Patel, K, Stoddart, J. F, & Zink, J. I. (2008) ph-responsive supramolecular nanovalves based on cucurbit [6] uril pseudorotaxanes. *Angewandte Chemie* **120**, 2254–2258.

[103] Hou, X, Ke, C, Bruns, C. J, McGonigal, P. R, Pettman, R. B, & Stoddart, J. F. (2015) Tunable solid-state fluorescent materials for supramolecular encryption. *Nature communications* **6**.

[104] Nakatsuka, M. A, Mattrey, R. F, Esener, S. C, Cha, J. N, & Goodwin, A. P. (2012) Aptamer-crosslinked microbubbles: Smart contrast agents for thrombin-activated ultrasound imaging. *Advanced Materials* **24**, 6010–6016.

[105] Lee, S, Park, K, Kim, K, Choi, K, & Kwon, I. C. (2008) Activatable imaging probes with amplified fluorescent signals. *Chemical Communications* pp. 4250–4260.

[106] Matsuo, K, Kamada, R, Mizusawa, K, Imai, H, Takayama, Y, Narazaki, M, Matsuda, T, Takaoka, Y, & Hamachi, I. (2013) Specific detection and imaging of enzyme activity by signal-amplifiable self-assembling 19f mri probes. *Chemistry–A European Journal* **19**, 12875–12883.

[107] Sakabe, M, Asanuma, D, Kamiya, M, Iwatate, R. J, Hanaoka, K, Terai, T, Nagano, T, & Urano, Y. (2012) Rational design of highly sensitive fluorescence probes for protease and glycosidase based on precisely controlled spirocyclization. *Journal of the American Chemical Society* **135**, 409–414.

[108] Jiang, T, Olson, E. S, Nguyen, Q. T, Roy, M, Jennings, P. A, & Tsien, R. Y. (2004) Tumor imaging by means of proteolytic activation of cell-penetrating peptides. *Proceedings of the National Academy of Sciences of the United States of America* **101**, 17867–17872.

[109] Truxal, A. E, Slack, C. C, Gomes, M. D, Vassiliou, C. C, Wemmer, D. E, & Pines, A. (2016) Frontispiece: Nondisruptive dissolution of hyperpolarized 129xe into viscous aqueous and organic liquid crystalline environments. *Angewandte Chemie International Edition* **55**.

[110] Springuel-Huet, M.-A, Bonardet, J.-L, Gédéon, A, & Fraissard, J. (1999) 129xe nmr overview of xenon physisorbed in porous solids. *Magnetic Resonance in Chemistry* **37**, S1–S13.

[111] Wang, Y, Roose, B. W, Philbin, J. P, Doman, J. L, & Dmochowski, I. J. (2015) Programming a molecular relay for ultrasensitive biodetection through 129xe nmr. *Angewandte Chemie*.

[112] Vartak, D. G & Gemeinhart, R. A. (2007) Matrix metalloproteases: underutilized targets for drug delivery. *Journal of drug targeting* **15**, 1–20.

[113] Ku, T.-H, Chien, M.-P, Thompson, M. P, Sinkovits, R. S, Olson, N. H, Baker, T. S, & Gianneschi, N. C. (2011) Controlling and switching the morphology of micellar nanoparticles with enzymes. *Journal of the American Chemical Society* **133**, 8392–8395.

[114] Nguyen, M. M, Carlini, A. S, Chien, M.-P, Sonnenberg, S, Luo, C, Braden, R. L, Osborn, K. G, Li, Y, Gianneschi, N. C, & Christman, K. L. (2015) Enzyme-responsive nanoparticles for targeted accumulation and prolonged retention in heart tissue after myocardial infarction. *Advanced Materials* **27**, 5547–5552.

[115] Schnurr, M, Sydow, K, Rose, H. M, Dathe, M, & Schröder, L. (2015) Brain endothelial cell targeting via a peptide-functionalized liposomal carrier for xenon hyper-cest mri. *Advanced healthcare materials* **4**, 40–45.

[116] Driehuys, B, Martinez-Jimenez, S, Cleveland, Z. I, Metz, G. M, Beaver, D. M, Nouls, J. C, Kaushik, S. S, Firszt, R, Willis, C, Kelly, K. T, et al. (2012) Chronic obstructive pulmonary disease: safety and tolerability of hyperpolarized 129xe mr imaging in healthy volunteers and patients. *Radiology* **262**, 279–289.

[117] Patz, S, Muradian, I, Hrovat, M. I, Ruset, I. C, Topulos, G, Covrig, S. D, Frederick, E, Hatabu, H, Hersman, F, & Butler, J. P. (2008) Human pulmonary imaging and spectroscopy with hyperpolarized 129 xe at 0.2 t. *Academic radiology* **15**, 713–727.

[118] Jokisaari, J. (2013) Xenon in liquid-crystalline samples. *eMagRes*.

[119] Sozzani, P, Comotti, A, Simonutti, R, Meersmann, T, Logan, J. W, & Pines, A. (2000) A porous crystalline molecular solid explored by hyperpolarized xenon. *Angewandte Chemie International Edition* **39**, 2695–2699.

[120] Baias, M, Demco, D. E, Istrate, D, Popescu, C, Blumich, B, & Moller, M. (2009) Morphology and molecular mobility of fibrous hard α-keratins by 1h, 13c, and 129xe nmr. *The Journal of Physical Chemistry B* **113**, 12136–12147.

[121] Duewel, M, Vogel, N, Weiss, C. K, Landfester, K, Spiess, H.-W, & Munnemann, K. (2012) Online monitoring of styrene polymerization in miniemulsion by hyperpolarized 129xenon nmr spectroscopy. *Macromolecules* **45**, 1839–1846.

[122] Moudrakovski, I. L, Sanchez, A. A, Ratcliffe, C. I, & Ripmeester, J. A. (2001) Nucleation and growth of hydrates on ice surfaces: new insights from 129xe nmr experiments with hyperpolarized xenon. *The Journal of Physical Chemistry B* **105**, 12338–12347.

[123] Muenster, O, Jokisaari, J, & Diehl, P. (1991) Nmr determination of the 129xe shielding anisotropy for xenon gas dissolved in liquid crystals. *Molecular Crystals and Liquid Crystals* **206**, 179–186.

[124] Rubin, S. M, Lee, S.-Y, Ruiz, E. J, Pines, A, & Wemmer, D. E. (2002) Detection and characterization of xenon-binding sites in proteins by 129 xe nmr spectroscopy. *Journal of molecular biology* **322**, 425–440.

[125] Boutin, C, Stopin, A, Lenda, F, Brotin, T, Dutasta, J.-P, Jamin, N, Sanson, A, Boulard, Y, Leteurtre, F, Huber, G, et al. (2011) Cell uptake of a biosensor detected by hyperpolarized 129 xe nmr: The transferrin case. *Bioorganic & medicinal chemistry* **19**, 4135–4143.

[126] Bai, Y, Wang, Y, Goulian, M, Driks, A, & Dmochowski, I. J. (2014) Bacterial spore detection and analysis using hyperpolarized 129 xe chemical exchange saturation transfer (hyper-cest) nmr. *Chemical Science* **5**, 3197–3203.

[127] Klippel, S, Döpfert, J, Jayapaul, J, Kunth, M, Rossella, F, Schnurr, M, Witte, C, Freund, C, & Schröder, L. (2014) Cell tracking with caged xenon: using cryptophanes as mri reporters upon cellular internalization. *Angewandte Chemie International Edition* **53**, 493–496.

[128] Norquay, G, Leung, G, Stewart, N. J, Wolber, J, & Wild, J. M. (2016) 129xe chemical shift in human blood and pulmonary blood oxygenation measurement in humans using hyperpolarized 129xe nmr. *Magnetic resonance in medicine*.

[129] Causier, A, Carret, G, Boutin, C, Berthelot, T, & Berthault, P. (2015) 3d-printed system optimizing dissolution of hyperpolarized gaseous species for micro-sized nmr. *Lab on a Chip* **15**, 2049–2054.

[130] Amor, N, Zänker, P, Blümler, P, Meise, F, Schreiber, L, Scholz, A, Schmiedeskamp, J, Spiess, H. W, & Münnemann, K. (2009) Magnetic resonance imaging of dissolved hyperpolarized 129 xe using a membrane-based continuous flow system. *Journal of Magnetic Resonance* **201**, 93–99.

[131] Cleveland, Z. I, Moller, H. E, Hedlund, L. W, & Driehuys, B. (2009) Continuously infusing hyperpolarized 129xe into flowing aqueous solutions using hydrophobic gas exchange membranes. *The Journal of Physical Chemistry B* **113**, 12489–12499.

[132] Jokisaari, J. P, Luckhurst, G. R, Timimi, B. A, Zhu, J, & Zimmermann, H. (2015) Twist-bend nematic phase of the liquid crystal dimer cb7cb: orientational order and conical angle determined by 129xe and 2h nmr spectroscopy. *Liquid Crystals* **42**, 708–721.

[133] Li, X, Newberry, C, Saha, I, Nikolaou, P, Whiting, N, & Goodson, B. M. (2006) Interactions between xenon and phospholipid bicelles studied by 2 h/129 xe/131 xe nmr and optical pumping of nuclear spins. *Chemical physics letters* **419**, 233–239.

[134] Baumer, D, Brunner, E, Blümler, P, Zänker, P. P, & Spiess, H. W. (2006) Nmr spectroscopy of laser-polarized 129xe under continuous flow: A method to study aqueous solutions of biomolecules. *Angewandte Chemie International Edition* **45**, 7282–7284.

[135] Thiriot, D. S, Nevzorov, A. A, & Opella, S. J. (2005) Structural basis of the temperature transition of pf1 bacteriophage. *Protein science* **14**, 1064–1070.

[136] Miller, J, Walton, J, & Roland, C. (1993) Nmr chemical shift of xenon-129 dissolved in polymers. *Macromolecules* **26**, 5602–5610.

[137] Cherubini, A & Bifone, A. (2003) Hyperpolarised xenon in biology. *Progress in Nuclear Magnetic Resonance Spectroscopy* **42**, 1–30.

[138] Karjalainen, J, Vaara, J, Straka, M, & Lantto, P. (2015) Xenon nmr of liquid crystals confined to cylindrical nanocavities: A simulation study. *Physical Chemistry Chemical Physics* **17**, 7158–7171.

[139] Croucher, M. D & Patterson, D. (1980) Temperature and composition dependences of the heat of mixing of mbba with hydrocarbon. *Journal of Solution Chemistry* **9**, 771–784.

[140] Rosta, L, Kroo, N, Dolganov, V, Pacher, P, Simkin, V, Török, G, & Pepy, G. (1987) Ten phases of mbba (a new phase diagram). *Molecular Crystals and Liquid Crystals* **144**, 297–307.

[141] Keyes, P, Weston, H, Lin, W, & Daniels, W. (1975) Liquid crystal phase diagrams: A study of seven thermotropic materials. *The Journal of Chemical Physics* **63**, 5006–5010.

[142] Molga, E & Stecki, J. (1977) Thermodynamics of solutions of liquid crystals iii. vapour pressure of benzene+ mbba (n-p-methoxybenzylidene-pn-butylaniline). *The Journal of Chemical Thermodynamics* **9**, 79–90.

[143] Tsuchiya, H & Nakamura, K. (1974) Effects of magnetic field on domain formation, in nematic liquid crystal mbba. *Molecular Crystals and Liquid Crystals* **29**, 89–101.

[144] Moghaddam, S, Yang, C, Rekharsky, M, Ko, Y. H, Kim, K, Inoue, Y, & Gilson, M. K. (2011) New ultrahigh affinity host- guest complexes of cucurbit [7] uril with bicyclo [2.2. 2] octane and adamantane guests: Thermodynamic analysis and evaluation of m2 affinity calculations. *Journal of the American Chemical Society* **133**, 3570–3581.

[145] Biedermann, F, Uzunova, V. D, Scherman, O. A, Nau, W. M, & De Simone, A. (2012) Release of high-energy water as an essential driving force for the high-affinity binding of cucurbit [n] urils. *Journal of the American Chemical Society* **134**, 15318–15323.